Immersed Boundary-Finite Difference Lattice Boltzmann Method for Predicting Particulate Flows

ROJAS MOLINA ROBERTO CARLOS

(Degree)
博士（工学）
(Date of Degree)
2013-09-25
(Date of Publication)
2014-09-01
(Resource Type)
doctoral thesis
(Report Number)
甲第5941号
(URL)
https://hdl.handle.net/20.500.14094/D1005941

Doctor Thesis

Immersed Boundary-Finite Difference Lattice Boltzmann Method for Predicting Particulate Flows

埋め込み境界法を用いた差分格子ボルツマン法に基づく粒子流数値予測手法に関する研究

July 2013

Department of Mechanical Engineering, Graduate School of Engineering, Kobe University

Rojas Molina Roberto Carlos

Doctor Thesis

Immersed Boundary-Finite Difference Lattice Boltzmann Method for Predicting Particulate Flows

埋め込み境界法を用いた差分格子ボルツマン法に基づく粒子流数値予測手法に関する研究

July 2013

Department of Mechanical Engineering, Graduate School of Engineering, Kobe University

Rojas Molina Roberto Carlos

Table of Contents

List of Tables

List of Figures

Nomenclature

A	negative viscosity term
c	lattice speed, $c = 1$
$\boldsymbol{c}$	discrete particle velocity, $\boldsymbol{c} = (c_x, c_y, c_z)$
C_D	drag coefficient
C_L	lift coefficient
$c_{PP'}$	force scale
c_{PW}	force scale
c_S	sound speed
D	particle diameter
f	particle velocity distribution function
f^{eq}	equilibrium distribution function
f^{+}	symmetric part of distribution function
f^{-}	anti-symmetric part of distribution function
$f^{eq,+}$	symmetric part of equilibrium distribution function
$f^{eq,-}$	anti-symmetric part of equilibrium distribution function
f_q	frequency of vortex shedding
g	particle velocity distribution function including an additional collision term
$\boldsymbol{G}$	external force, $\boldsymbol{G} = (G_x, G_y, G_z)$
$\boldsymbol{G}_P$	force acting on P
F_D	drag force
F_L	lift force
$\boldsymbol{F}_{PP'}$	repulsive force between the particles P and P'
$\boldsymbol{F}_{PW}$	repulsive force between the particle P and the wall W
G_i	direct forcing term for f_i
h	distance between two plates
I_P	moment of inertia
l	relative error
L	length of the recirculation region in steady flows
M_P	mass o the particle
N_m	number of Lagrangian points at immersed boundary
p	pressure

Q	number of discrete particle velocities
Re	Reynolds number
R_{in}	radius of inner cylinder
R_{out}	radius of outer cylinder
R_P	radius of the particle P
$R_{P'}$	radius of the particle P'
St	Strouhal number
t	time
T_P	torque
$\boldsymbol{u}$	fluid velocity, $\boldsymbol{u} = (u, v, w)$
u_θ	azimuthal velocity component
$\boldsymbol{u}_P$	velocity of solid body
u_b	boundary velocity
u^S	slip velocity
u_T	analytical azimuthal velocity component
U_0	free stream velocity
U_d	horizontal velocity of moving plates
U_θ	rotation velocity of circular cylinder
$\boldsymbol{U}_P$	translational particle velocity
W	weighting function
$\boldsymbol{x}$	Eulerian coordinates, $\boldsymbol{x} = (x, y, z)$
$\boldsymbol{X}_L$	coordinates of Lagrangian point, $\boldsymbol{X}_L = (X_L, Y_L, Z_L)$
$\boldsymbol{X}_P$	coordinates of the center of gravity of the particle P, $\boldsymbol{X}_P = (X_P, Y_P, Z_P)$
Δ	domain of the smoothed delta function
δ	smoothed-delta function
δ_h	one-dimensional smoothed-delta function
$\Delta\boldsymbol{u}$	corrector of velocity in the implicit direct-forcing method
ΔS	area segment of solid body
Δt	time step size
ΔV	computational cell volume
Δx	lattice width in the x direction
Δy	lattice width in the y direction
Δz	lattice width in the z direction

γ	Euler constant
ε	Knudsen number
ε_P	stiffness parameter for collision
ε_W	stiffness parameter for collision
ζ_P	threshold or safe zone
ζ_W	threshold or safe zone
θ	angle of incidence
Λ	magic parameter
μ	viscosity
ν	kinematic viscosity
ρ	density
ρ_P	particle density
τ	single relaxation time
τ_+	relaxation time for f^+ in two-time relaxation model
τ_-	relaxation time for f^- in two-time relaxation model
Ω	collision operator
ω_P	angular velocity

Subscript

i	direction of discrete particle velocity
$\bar{i}$	direction opposite to i
I,J,K	indexes of lattice points
L	index of Lagrangian node

Superscript

n	discrete time
j	position of the lattice point along the y-axis

1

Introduction

1.1 Background

Particulate flows are encountered in a wide variety of engineering applications such as fluid flow in chemical reactors, waste streams with suspended solids, aerosols, and so on. Owing to their diversity, the particle size and the particle shape in these systems vary in an extensive range. The particle Reynolds numbers in particulate flows which are based on the particle size and its velocity vary broadly. Due to these features, the solution of particulate systems is one of the most challenging problems in engineering.

In a few simple cases, analytical solutions of the governing equations of the flow are available. However, the analytical method is not appropriate when the complexity of the problem increases. Experiments can provide valuable information of the flow, and they have been a fundamental approach to particulate flow analyses. However, some disadvantages arise due to the limitation in hardware and the difficulty in setting up an experimental apparatus. Due to the rapid progress of computer technology, the use of computational fluid dynamics (CFD) for investigating particulate flows has been increasing in recent years.

CFD has made the study of particulate flows more efficient and has been used as a complement and/or an option to analytical and experimental approaches. Several numerical methods are available to predict particulate flows. The available numerical methods consider mainly two characteristics of the system: the particles are stationary or moving, and the shape of the particles is regular or not. The selection of one particular method depends on the problem since some methods could be more suitable than others to a specific case. In addition, the quality of predictions is subjected to some important aspects such as accuracy, stability, speed of the computation, and/or difficulty in setting up the problem.

1.2 Numerical methods for predicting particulate flows

Several numerical techniques are available to predict particulate flows. Conventional CFD methods for particulate flows are based on the solution of the conservation equations, i.e. the continuity and Navier-Stokes equations, to solve the fluid flow and the motion of particles are predicting using the equation of motion for a rigid body. Finite difference, finite elements and finite volume methods are the most popular approaches for the discretization of the conservation equations.

Due to its simplicity and effectiveness in solving problems with body-fitted grids; the finite difference method (FDM) has been used to predict flows with high-order schemes [Shukla et al., 2007; Liu & Wang, 2004]. However this method is limited to solve problems with relatively simple computational domains and stationary boundaries. On the other hand, one of the most attractive advantages of the finite volume method (FVM) and finite element method (FEM) is the suitability for problems with complex boundaries owing to the use of unstructured grids. Several studies have proved the capability of these methods for predicting particulate flows with moving boundaries [Hu & Joseph, 1992; Hu & Patankar 2001; Wang & Turek, 2007; Glowinsky et al., 1999]. A drawback of these methods is however the need for remeshing or grid adaptation at each time step. The algorithm for the grid generation or adaptation is likely to be complicated and the computation could become slow, especially when flows with a large number of particles are calculated.

A relatively new approach called the lattice Boltzmann method (LBM) has been proposed as an alternative to predict fluid flows [McNamara & Zanetti, 1988; Succi, 2000; Chen & Doolen, 1998]. The basis of LBM is the lattice Boltzmann equation (LBE), which describes the time evolution of the discrete velocity distribution function. The macroscopic variables such as the density and momentum are defined as moments of the distribution function. The Navier-Stokes equation can be derived from LBE using the Chapman-Enskog analysis. Some of the features that give LBM advantages in computational efficiency over the conventional methods are: (1) the computation in LBM is much simpler than those in the conventional Navier-Stokes solvers since the time marching procedure in LBM is fully explicit and there is no need to solve Poisson equations; (2) the local nature of the discrete particle collision operator in LBE and the fully explicit time integration of LBE makes this method suitable for parallel computing; (3) easy implementation of the method starting from scratch [Kandhai et al., 1999]; and (4) easy implementation of the no-slip boundary condition for complex geometry by making use of the bounce-back rule [Ladd, 1994]. However the bounce-back rule defines the body surface as a step function. Therefore, high spatial resolution is required to smoothly represent a complex geometry.

In all the aforementioned methods, time-consuming tasks related to the grid adaptation, complicated solution algorithms or highly computational cost grids are needed for accurately imposing the no-slip boundary condition at moving bodies and/or complex channel walls. Conversely, there is an additional approach which can be defined as a non-body-fitted grid method, that is, the immersed boundary method (IBM). IBM has emerged to overcome some drawbacks of body-fitted grid methods.

1.3 Immersed boundary method

1.3.1 Outline of the immersed boundary method

The immersed boundary method was originally proposed by Peskin [Peskin, 1977] to calculate blood flows in heart. This method uses the Cartesian grid for calculating the fluid flow and the boundary condition at moving bodies and/or channel walls is accounted for by using the so-called immersed boundaries. Lagrangian points are used to represent the immersed boundaries in the fluid where the no-slip boundary condition is imposed. IBM has been often implemented into conventional methods [Lai & Peskin, 2000; Fadlun et al., 2000; Kim et al., 2001].

1.3.2 Implementation of IBM into LBM

Due to the aforementioned advantages of LBM, various methods combining LBM and IBM (Immersed Boundary LBM: IB-LBM) have been recently developed for predicting liquid-solid two-phase flows. Numerical calculations of particulate flows such as flows past a circular cylinder, drafting-kissing-tumbling (DKT) motion of two particles or sedimentation of thousands of particles, have demonstrated that IB-LBM reasonably predicts the fluid-particle interaction of stationary or moving particles at moderate particle Reynolds numbers [Feng & Michelaides, 2004; 2005; 2009; Wu & Shu, 2009; Lin et al., 2010; Kang & Hassan, 2010].

Most of IB-LBMs utilize the single-relaxation time (SRT) model for the particle collision term in the lattice Boltzmann equation due to its simple implementation. Since the relaxation time, τ, is a monotonically increasing function of the kinematic viscosity ν, τ increases with ν, i.e. with decreasing the Reynolds number. Le & Zhang [2009] pointed out that the validity of IB-LBMs strongly depends on τ. They carried out simulations of planar and circular Couette flows using a direct-forcing IB-LBM with SRT, and showed that errors in velocity near the immersed boundary remarkably increase with decreasing the Reynolds number, i.e. increasing τ. In addition, IB-LBM is not free from restrictions of LBM, e.g., (1) simulation of high Reynolds number flows with a low relaxation time is apt to be unstable so that the spatial resolution must be high to perform stable calculations at these conditions, and (2) the Lagrangian nature of LBE requires that a discrete particle moves from a lattice point to its neighbor during one time step, and therefore, the lattice spacing and the time step size cannot be altered independently. These drawbacks restrict the use of IB-LBM for predicting flows for a wide range of Reynolds numbers.

1.3.3 Numerical evidence of drawbacks in IB-LBM

In the following, IB-LBM proposed by Kang & Hassan [Kang & Hassan, 2010] will be used to examine the applicability of IB-LBM to predictions of flows at high and low Reynolds numbers, i.e. low and high relaxation times, respectively.

1.3.3.1 Numerical method

The lattice Boltzmann equation (LBE) with the direct-forcing term, G_i, is given by

$$f_i(\boldsymbol{x}+\boldsymbol{c}_i\Delta t, t+\Delta t) = f_i(\boldsymbol{x},t)+\Omega_i(f_i(\boldsymbol{x},t))+G_i \tag{1.1}$$

where f_i is the particle velocity distribution function in the ith direction, $\boldsymbol{x}$ the position vector, $\boldsymbol{c_i}$ the discrete particle velocity, t the time, Δt the time step size, Ω_i the collision operator, and G_i acts on the fluid in the vicinity of immersed boundaries to impose the no-slip boundary condition. The single-relaxation time collision model is given by [Bhatnagar, 1954]

$$\Omega_i(f_i(\boldsymbol{x},t)) = -\frac{1}{\tau}[f_i(\boldsymbol{x},t) - f_i^{eq}(\boldsymbol{x},t)] \tag{1.2}$$

where f_i^{eq} is the equilibrium distribution function. Applying the semi-implicit temporal discretization to G_i yields [Kang & Hassan, 2010; Chen & Li, 2008]

$$\begin{aligned} f_i(\boldsymbol{x}+\boldsymbol{c}_i\Delta t, t+\Delta t) = f_i(\boldsymbol{x},t) &- \frac{1}{\tau}[f_i(\boldsymbol{x},t) - f_i^{eq}(\boldsymbol{x},t)] \\ &+ \frac{\Delta t}{2}[G_i(\boldsymbol{x}+\boldsymbol{c}_i\Delta t, t+\Delta t) + G_i(\boldsymbol{x},t)] \end{aligned} \tag{1.3}$$

The macroscopic fluid density, ρ, and velocity, $\boldsymbol{u}$, are given by

$$\rho = \sum_{i=0}^{Q-1} f_i \tag{1.4}$$

$$\rho\boldsymbol{u} = \sum_{i=0}^{Q-1} \boldsymbol{c}_i f_i \tag{1.5}$$

where Q is the number of discrete velocities. The two-dimensional nine-velocity (D2Q9) model is used in the calculations for the discrete velocity. The equilibrium distribution function of this model is given by

Table 1.1 Discrete particle velocity and weighting coefficients in the D2Q9 model

i	0	1	2	3	4	5	6	7	8
c_x	0	c	0	c	0	c	c	c	c
c_y	0	0	c	0	c	c	c	c	c
W_i	4/9	1/9	1/9	1/9	1/9	1/36	1/36	1/36	1/36

$$f_i^{eq} = W_i \rho \left[1 + \frac{3(\boldsymbol{c}_i \cdot \boldsymbol{u})}{c^2} + \frac{9(\boldsymbol{c}_i \cdot \boldsymbol{u})^2}{2c^4} - \frac{3\boldsymbol{u} \cdot \boldsymbol{u}}{2c^2} \right] \tag{1.6}$$

where W_i is the weighting function and c the lattice velocity (c = 1). The values of $\boldsymbol{c}_i$ and W_i are summarized in Table 1.1, where c_x and c_y are the components of $\boldsymbol{c}_i$ in the Cartesian coordinates (x, y). Applying the Chapman-Enskog expansion to Eq. (1.3) recovers the macroscopic conservation equations for an incompressible Newtonian fluid with second-order accuracy:

$$\nabla \cdot \boldsymbol{u} = 0 \tag{1.7}$$

$$\frac{\partial \boldsymbol{u}}{\partial t} + \boldsymbol{u} \cdot \nabla \boldsymbol{u} = -\frac{\nabla p}{\rho} + \nu \nabla \cdot [\nabla \boldsymbol{u} + (\nabla \boldsymbol{u})^T] + \frac{\boldsymbol{G}}{\rho} \tag{1.8}$$

where the superscript T denotes the transpose, $\boldsymbol{G}$ the external force acting on the fluid at the immersed boundaries to satisfy the boundary condition and p the pressure given by $p = \rho c^2/3$, which gives the speed of sound, $c_S = c/\sqrt{3}$. The kinematic viscosity is given by

$$\nu = \frac{c^2 \Delta t}{3} \left(\tau - \frac{1}{2} \right) \tag{1.9}$$

Since Δt and $c = \Delta x/\Delta t$ are set at unity, Eq. (1.9) reduces to $\nu = (\tau - 1/2)/3$.

The solution algorithm of Eq. (1.3) is split into the following four steps [Kang & Hassan, 2010]:

(I) First-forcing step

$$f_i'(\boldsymbol{x},t) = f_i(\boldsymbol{x},t) + \frac{\Delta t}{2} G_i(\boldsymbol{x},t) \tag{1.10}$$

(II) Collision step

$$f_i''(\boldsymbol{x},t) = f_i'(\boldsymbol{x},t) - \frac{1}{\tau}[f_i'(\boldsymbol{x},t) - f_i^{eq}{}'(\boldsymbol{x},t)] \tag{1.11}$$

(III) Second-forcing step

$$f_i'''(\boldsymbol{x},t) = f_i''(\boldsymbol{x},t) + \frac{\Delta t}{2} G_i(\boldsymbol{x},t) \tag{1.12}$$

(IV) Streaming step

$$f_i(\boldsymbol{x} + \boldsymbol{c}_i \Delta t, t + \Delta t) = f_i'''(\boldsymbol{x},t) \tag{1.13}$$

where f', f'' and f''' are temporal distribution functions.

Fluid motion is computed at Eulerian grid points using Eqs. (1.10)-(1.13), whereas solid boundaries immersed in the flow field are represented using Lagrangian points as shown in Fig. 1.1. The Eulerian coordinates at the grid point IJ and the coordinates of the Lth Lagrangian point are denoted by $\boldsymbol{x}_{IJ} = (x_I, y_J)$ and $\boldsymbol{X}_L = (X_L, Y_L)$, respectively. The external force, $\boldsymbol{G}(\boldsymbol{X}_L, t)$, acting on the fluid to impose the no-slip boundary condition is given by [Kang & Hassan, 2010]

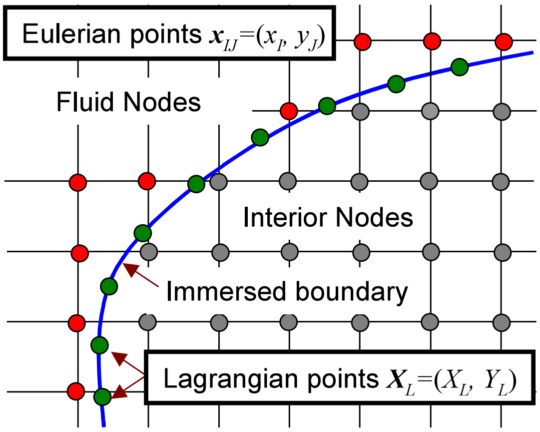

Fig. 1.1 Immersed boundary method. The intersection of mesh lines define Eulerian points ($\boldsymbol{x}_{IJ}$) while the points on the body surface represent Lagrangian points ($\boldsymbol{X}_L$)

$$\boldsymbol{G}(\boldsymbol{X}_L,t) = 2\frac{\boldsymbol{u}_P(\boldsymbol{X}_L,t) - \boldsymbol{u}(\boldsymbol{X}_L,t)}{\Delta t} \tag{1.14}$$

where $\boldsymbol{u}_P(\boldsymbol{X}_L, t)$ is the velocity at the Lth Lagrangian point, and $\boldsymbol{u}(\boldsymbol{X}_L, t)$ the fluid velocity interpolated by using

$$\boldsymbol{u}(\boldsymbol{X}_L,t) = \sum_{\boldsymbol{x}_{IJ}\in\Delta} \boldsymbol{u}(\boldsymbol{x}_{IJ},t)\delta(\boldsymbol{x}_{IJ} - \boldsymbol{X}_L)\Delta V \tag{1.15}$$

where δ is the smoothed-delta function, ΔV the volume of a computational cell and Δ the domain in which $\delta \neq 0$. The delta function is given by

$$\delta(\boldsymbol{x}_{IJ} - \boldsymbol{X}_L) = \delta_h\left(\frac{x_I - X_L}{\Delta x}\right)\delta_h\left(\frac{y_J - Y_L}{\Delta y}\right) \tag{1.16}$$

where Δx and Δy are the lattice spacings in the x and y directions, respectively, and δ_h is the one-dimensional smoothed-delta function. The following two-point stencil delta function is utilized [Kang & Hassan, 2010]:

$$\delta_h(r) = \begin{cases} 1-|r| & \text{for } |r| \le 1 \\ 0 & \text{otherwise} \end{cases} \tag{1.17}$$

The force calculated using Eq. (1.14) is distributed onto the Eulerian grid points by using the delta function:

$$\boldsymbol{G}(\boldsymbol{x}_{IJ},t) = \sum_{L=1}^{N_m} \boldsymbol{G}(\boldsymbol{X}_L,t)\delta(\boldsymbol{x}_{IJ} - \boldsymbol{X}_L)\Delta S \Delta x \tag{1.18}$$

where N_m is the number of Lagrangian points and ΔS the area segment of a solid body. The discrete forcing term with first-order accuracy is given by

$$G_i(\boldsymbol{x}_{IJ},t) = \frac{3\rho W_i}{c^2}\boldsymbol{c}_i \cdot \boldsymbol{G}(\boldsymbol{x}_{IJ},t) \tag{1.19}$$

The necessary and sufficient condition for numerical stability is [Chen & Doolen, 1998]

$$\tau > \frac{1}{2} \tag{1.20}$$

In addition, the characteristic velocity, U, is also bounded by $U/c_S < 0.3$ [Chen & Doolen, 1998] for satisfying the condition of incompressibility.

1.3.3.2 Flows past a circular cylinder

Flows past a stationary circular cylinder are calculated to examine the applicability of IB-LBM at high Reynolds number flows. The Reynolds number of the flow is defined by

$$Re = \frac{U_0 D}{\nu} \tag{1.21}$$

where U_0 is the free stream velocity and D the diameter of the cylinder. This problem has been extensively studied and many experimental and numerical results are available. Table 2 summarizes the drag coefficients, C_D, and the Strouhal numbers, St, at Re = 100, 1000 and 10000 predicted by using two-dimensional simulations with finite-difference and finite element methods [Park et al, 1998; Lei et al., 2000; Matsumiya et al., 1993; Mittal & Kumar, 2001; Kondo, 1993]. The predictions at Re = 100 agree well with the measured data [Wieselsberger, 1922; Roshko, 1954; Schewe, 1983]. Mansy et al. [Mansy, 1994] showed that small-scale three-dimensional disturbances appear in the near wake region when Re is larger than about 200. The two-dimensional simulation, of course, cannot reproduce the three-dimensional flow structure. Therefore the predictions at Re = 1000 and 10000 [Lei et al. 2000; Matsumiya, 1993; Mittal & Kumar, 2001; Kondo, 1993] differ from the measured data. However these two-dimensional simulations give almost the same C_D and St, and little depend on Re. This is because the separation point of flow at the cylinder surface is not altered at Re = 1000 and 10000. Thus, the drag at high Reynolds numbers mainly consists of form drag and the contribution of three-dimensional structure to the drag coefficient may become weaker and weaker as Re increases.

Two-dimensional simulations are carried out using IB-LBM for a wide range of Reynolds number, i.e. $1 \leq Re \leq 1\times10^5$. The computational domain is shown in Fig. 1.2. The dimensions of the domain are $W = 50D$ and $H = 40D$ in the x and y directions, respectively. The cylinder is located at $(X_P, Y_P) = (20D, 20D)$ and $D/\Delta x = 40$. The computational grid is uniform and $\Delta x = \Delta y = 1$. The number of Lagrangian points, N_m, is 126 and these points are evenly distributed along the cylinder surface. Hence ΔS in Eq. (1.18) is $\pi D/N_m$. The left boundary is uniform inflow at $U_0 = 0.05$. The right, top and bottom boundaries are continuous outflow.

Table 1.2 Comparison of C_D and St of flow past a stationary circular cylinder for $10^2 \le Re \le 10^4$

Re		C_D	*St*
100	FDM, 2D* [Park et al., 1998]	1.330	0.165
	FDM, 2D [Lei et al., 2000]	1.490	0.180
	FDM, 2D [Matsumiya et al., 1993]	1.423	0.163
	Measured [Wieselsberger, 1922; Roshko, 1954; Schewe, 1983]	≈1.39	≈0.16
1000	FDM, 2D [Lei et al., 2000]	1.510	0.240
	FDM, 2D [Matsumiya et al., 1993]	1.500	0.220
	FEM, 2D** [Mittal & Kumar, 2001]	1.480	0.250
	FEM, 2D [Kondo, 1993]	1.400	-
	Measured [Wieselsberger, 1922; Roshko, 1954; Schewe, 1983]	≈0.95	≈0.21
10000	FDM, 2D [Matsumiya et al., 1993]	1.661	0.222
	FEM, 2D [Kondo, 1993]	1.712	-
	Measured [Wieselsberger, 1922; Roshko, 1954; Schewe, 1983]	≈1.10	≈0.20

*FDM: finite difference method; **FEM: finite element method

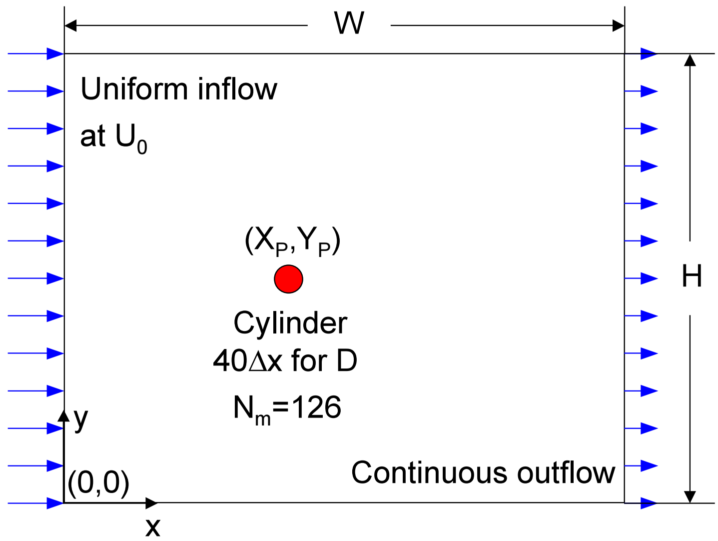

Fig. 1.2 Computational domain for flows past a circular cylinder

The drag coefficients predicted by IB-LBM are plotted against the Reynolds number in Fig. 1.3. Good agreement between measured [Wieselsberger, 1920] and predicted C_D is obtained up to Re = 100. For 500 < Re < 2000, the predicted drag coefficients differ from the measured data. However the drag coefficient of flows at Re = 1000 agrees well with the other predictions obtained using the two-dimensional FDM and FEM [Lei et al, 2000; Matsumiya, 1993; Mittal & Kumar, 2001; Kondo, 1993]. Figure 1.4 shows the predicted Strouhal number. At Re = 100, the prediction agrees well with the experimental data [Roshko, 1954]. The predicted Strouhal numbers for $Re \geq 500$ differ from the experimental data [Roshko, 1954; Schewe, 1983], though the Strouhal number at Re = 1000 is similar to those predicted with the other methods. When $Re \geq 2000$, numerical instability arises and converged solutions are not obtained with the spatial resolution of $D/\Delta x = 40$. From Eq. (1.21), at given U_0 and D, the viscosity must be decreased to increase Re. As can be understood from Eq. (1.9), this reduction makes τ approaching to 1/2 and the computation becomes unstable as ν decreases. Hence a large $D/\Delta x$, i.e., high spatial resolution, is required to satisfy Eq. (1.20) at high Reynolds numbers [Sterling & Chen, 1996; Cao et al., 1997]. In the stable computation at Re = 2000, the relaxation time is 0.503 which, satisfies Eq. (1.20). To keep $\tau = 0.503$ also at Re = 2500, the spatial resolution must be increased to $D/\Delta x = 50$. Likewise, the resolution must be $D/\Delta x = 2000$ at $Re = 1\times10^5$. Thus the computational costs drastically increases with Re.

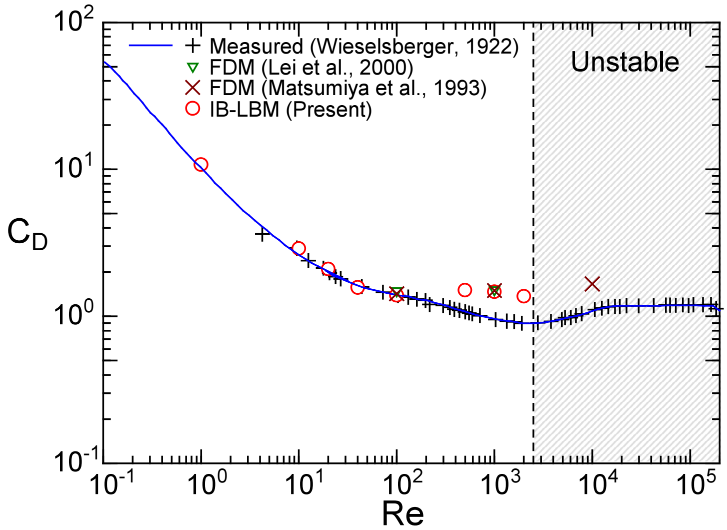

Fig. 1.3 Drag coefficient of a stationary cylinder predicted by using IB-LBM

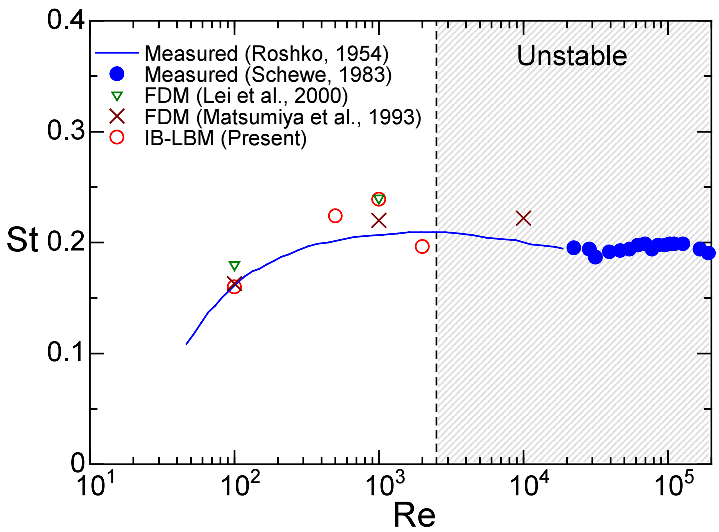

Fig. 1.4 Strouhal number of a stationary cylinder predicted by using IB-LBM

1.3.3.3 Circular Couette flows

Calculations of circular Couette flows are carried out using the IB-LBM to make clear issues appearing in simulations of low *Re* flows, i.e. at high τ.

The numerical conditions are similar to those used in Le & Zhang [2009]. Figure 1.5(a) shows the numerical setup of steady circular Couette flows between a stationary and a rotating cylinder. The computational domain is a square, and the number of lattice points is 201 in the x and y directions. The inner circular cylinder is rotating at velocity $U_\theta = 0.01$, while the outer circular cylinder is at rest. They are located at the center of the domain, and their radii are 45 and 70, respectively. The number of Lagrangian points is 800 for both rings. Periodic boundary conditions are adopted for all the domain boundaries. The Reynolds number of the flow is defined by

$$Re = \frac{(R_{out} - R_{in})U_\theta}{\nu} \tag{1.22}$$

where R_{in} and R_{out} are the radii of the inner and outer cylinders, respectively. The range of Reynolds number tested is from 0.038 to 1.5. The analytical solution of the flow is given by

$$\frac{u_\theta}{U_\theta} = \frac{R_{in}R^2 - R_{out}^2 R_{in}}{R_{in}^2 R - R_{out}^2 R} \tag{1.23}$$

where u_θ is the velocity component in the azimuthal direction. The velocity distribution of the analytical solution is also shown in Fig. 1.5(b).

Figure 1.6 shows the predicted velocity component in the azimuthal direction, u_θ/U_θ, in the steady state. The black circles represent the immersed boundaries. With the direct-forcing method, both particle velocity distributions in the fluid and in the solid are solved. This causes pseudo-fluid velocities inside the inner and outer cylinders. As can be seen, the non-physical distortion of the velocity field or velocity slip pointed out by Le & Zhang [2009] appears when the Reynolds number is low, i.e. when the relaxation time is high.

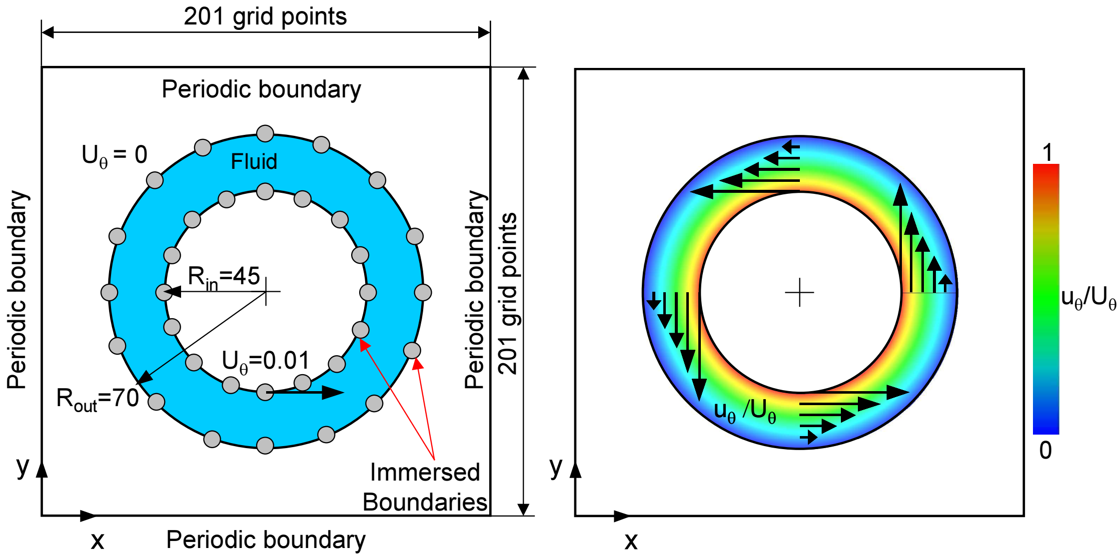

(a) (b)

Fig. 1.5 Computational domain for simulation of circular Couette flow (a) and analytical solution (b)

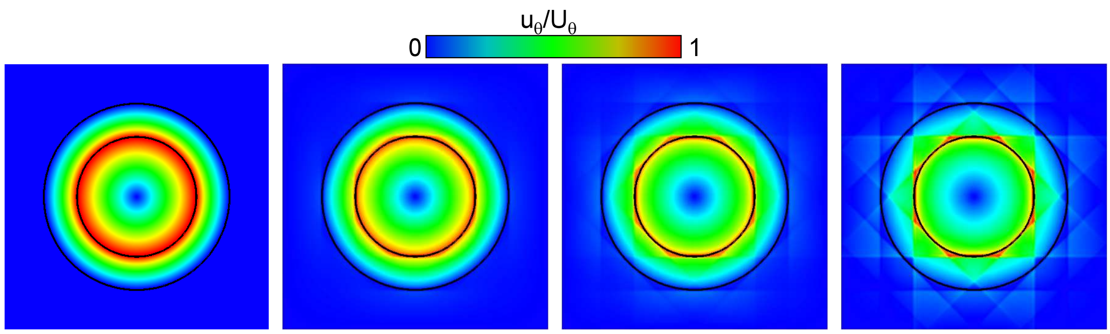

(a) $(Re, \tau) = (1.5, 1)$ (b) (0.17, 5) (c) (0.079, 10) (d) (0.038, 20)

Fig. 1.6 Velocity distributions predicted by using IB-LBM with SRT

1.4 Objectives

According to the above discussion, IB-LBM can be regarded as a promising method for predicting particulate flows. However IB-LBM has not yet matured and the following requirements lie on the way toward a versatile numerical method for predicting particulate flows involving various Reynolds number particles:

(1) Programming the numerical method should be easy.

(2) Problems with moving boundaries and/or complicated channel geometries can be effectively handled.

(3) The numerical method has some advantages over other existing numerical methods, especially with respect to stability, accuracy, speed of the calculation and/or easiness in setting up the problem.

In order to accomplish the above-mentioned objectives, a new IB-LBM is proposed in this study. Specifically, the scope of the developed method is

(1) to reduce or eliminate the error in velocity fields at high relaxation times (low Reynolds numbers),

(2) to extend the range of applicability of the proposed method to the solution of flows with moving or stationary boundaries at high and low particle Reynolds numbers, and

(3) to show that the present method can efficiently solve problems for a wide range of particle Reynolds numbers.

1.5 Preview

In Chapter 2, a numerical method to solve problems with moving boundaries is proposed. The method is a combination of an immersed boundary method and a finite difference lattice Boltzmann method. The proposed method is validated through calculations of particulate flows in two and three dimensions. First, the sedimentation of two- and three-dimensional single particles is calculated. The predicted velocity and particle position are compared with available experimental data. Then, two- and three-dimensional calculations of the draft-kissing-tumbling motion of two particles are carried out.

In Chapter 3, the applicability of the present method to flows at high Reynolds numbers is examined. Flows past stationary circular and square cylinders and a sphere are calculated for a wide range of Reynolds numbers. The results are compared with other numerical predictions and available measured data. Finally, calculations of free-falling cylinders at different Reynolds numbers are carried out to examine the applicability of the present method to problems with moving boundaries at high Reynolds numbers.

In Chapter 4, a remedy to the distortion of velocity field at low Reynolds numbers, i.e. at high relaxation times, in IB-LBM is proposed. The single-relaxation time collision term is replaced with a two-relaxation time (TRT) collision term. The proposed remedy is validated through simulations of circular Couette flows. Then, a theoretical study of the effect of the two-relaxation time collision term on the velocity slip is carried out.

In Chapter 5, the two-relaxation time collision term is also implemented into IB-FDLBM. Initially, the Chapman-Enskog expansion is applied to the discrete lattice Boltzmann equation to check the recovery of the Navier-Stokes equations. Then, the proposed method is validated through simple flows, i.e. circular Couette flows. The velocity profiles obtained by using SRT and TRT are compared in order to make clear the advantages of the proposed method. The influence of the numerical parameters used to improve the stability and accuracy of the calculations on the error in velocity is also investigated and the optimum values of the parameters are discussed. This method is also evaluated in the simulation of flows past a circular cylinder and a sphere at low Reynolds numbers. At this condition, some non-physical penetration of the streamlines into the immersed boundaries becomes stronger. An implicit velocity correction method is therefore implemented to accurately impose the no-slip boundary condition and overcome the penetration of streamlines. A simulation of particulate flows at different Reynolds numbers is also carried out to demonstrate that the developed method can predict particulate flows for a wide range of particle Reynolds numbers.

In Chapter 6, the concluding remarks of this study are summarized. Besides, some suggestions for future research are given to finalize this dissertation.

References

Bhatnagar, P., L., Gross, E., P., Krook, M., A model for collision processes in gases. I. Small amplitude processes in charged and neutral one-component systems, Physical Review, 1954, 94, pp. 511-525.

Cao, N., Chen, S., Jin, S., Martinez, D., Physical symmetry and lattice symmetry in the lattice Boltzmann method, Physical Review E, 1997, 55(1), pp. 21-24.

Chen, S., Doolen, G. D., Lattice Boltzmann method for fluid flows, Annual Review of Fluid Mechanics, 1998, 30, pp. 329-364.

Chen, Y., Li, J., Introducing unsteady non-uniform source terms into the lattice Boltzmann model, International journal of Numerical Methods in Fluids, 2008, 56, pp. 629-641.

Fadlun, E. A., Verzicco, R., Orlandi, P., Mohd-Yusof, J., Combined immersed-boundary finite-difference methods for three-dimensional complex flow simulations, Journal of Computational Physics, 2000, 161, pp. 35-60.

Feng, Z.-G., Michaelides, E. E., The immersed boundary-lattice Boltzmann method for solving fluid-particles interaction problems, Journal of Computational Physics, 2004, 195, pp. 602-628.

Feng, Z.-G., Michaelides, E. E., Proteus: a direct forcing method in the simulations of particulate flows, Journal of Computational Physics, 2005, 202, pp. 20-51.

Feng, Z.-G., Michaelides, E. E., Robust treatment of no-slip boundary condition and velocity updating for the lattice-Boltzmann simulation of particulate flows, Computers and Fluids, 2009, 38, pp. 370-381.

Glowinski, R., Pan, T., Hesla, T., Joseph, D., Periaux, J., A fictitious domain approach to the direct numerical simulation of incompressible viscous flow past moving rigid bodies: application to particulate flow, Journal of Computational Physics, 2001, 169, pp. 363-426.

Hu, H., Joseph, D., Crochet, M., Direct simulation of fluid particle motions, Theoretical and Computational Fluid Dynamics, 1992, 3, pp. 285-306.

Hu, H., Patankar, N., Zhu, M., Direct numerical simulations of fluid-solid systems using the arbitrary Lagrangian-Eulerian techniques, Journal of Computational Physics, 2001, 169, pp. 427-462.

Kandhai, D., Vidal, D., Hoekstra, A., Hoefsloot, H., Iedema, P., Sloot, P., Lattice-Boltzmann and finite element simulations of fluid flow in a SMRX static mixer reactor, International Journal for Numerical Methods in Fluids, 1999, 31, pp. 1019-1033.

Kang, S. K., Hassan, Y. A., A comparative study of direct-forcing immersed boundary-lattice Boltzmann methods for stationary complex boundaries, International Journal for Numerical Methods in Fluids, 2010, DOI: 10.1002/fld.2304.

Kim, J., Kim, D., Choi, H., An immersed-boundary finite-volume method for simulations of flow in complex geometries, Journal of Computational Physics, 2001, 171, pp. 132-150.

Kondo, N., Direct third-order upwind finite element simulation of high Reynolds number flows around a circular cylinder, Journal of Wind Engineering and Industrial Aerodynamics, 1993, 46&47, pp. 349-356.

Ladd, A. J. C., Numerical simulations of particulate suspensions via a discretized Boltzmann equation. Part II: Numerical results, Journal of Fluid Mechanics, 1994, 271, pp. 311-339.

Lai, M.C., Peskin, C. S., An immersed boundary method with formal second-order accuracy and reduced numerical viscosity, Journal of Computational Physics, 2000, 160, pp. 705-719.

Le, G., Zhang, J., Boundary slip from the immersed boundary lattice Boltzmann models, Physical Review E, 2009, 79, 026701.

Lei, C., Cheng, L., Kavanagh K., A finite difference solution of the shear flow over a circular cylinder, Ocean Engineering, 2000, 27, pp. 271-290.

Lin, S.-Y., Lin, C.-T., Chin, Y.-H., Tai, Y.-H., A direct-forcing pressure-based lattice Boltzmann method for solving fluid-particle interaction problems, International Journal for Numerical Methods in Fluids, 2010, DOI: 10.1002/fld.2442.

Liu, J. G., Wang, C., High order finite difference methods for unsteady incompressible flows in multi-connected domains, Computers & Fluids, 2004, 33, pp. 223-255.

Mansy, H., Yang, P.M., Williams, D.R., Quantitative measurements of three-dimensional structures in the wake of a circular cylinder, Journal of Fluid Mechanics, 1994, 270, pp. 277-296.

Matsumiya, H., Kieda, K., Taniguchi, N., Kobayashi, T., Numerical simulation of 2D flow around a circular cylinder by the third-order upwind finite difference method, Transaction of Japanese Society of Mechanical Engineers, Series B, 1993, 59(566), pp. 2937-2943. (in Japanese)

McNamara, G. R, Zanetti, G., Use of the Boltzmann equation to simulate lattice-gas automata, Physical Review Letters, 1988, 61(20), pp. 2332-2335.

Mittal, S., Kumar, V., Flow-induced vibrations of a light circular cylinder at Reynolds number 10^3 to 10^4, Journal of Sound and Vibration, 2001, 245(5), pp. 923-946.

Park, J., Kwon, K., Choi, H., Numerical solutions of flow past a circular cylinder at Reynolds numbers up to 160, KSME International Journal, 1998, 12(6), pp. 1200-1205.

Peskin, C. S., Numerical analysis of blood flow in the heart, Journal of Computational Physics, 1977, 25, pp. 220-252.

Roshko, A., On the development of turbulent wakes from vortex streets, NACA, 1954, Rep. 1191.

Schewe, G., On the force fluctuations acting on a circular cylinder in cross flow from subcritical up to transcritical Reynolds numbers, Journal of Fluid Mechanics, 1983, 133, pp. 265-285.

Shukla, R., Tatineni, M., Zhong, X., Very high-order compact finite difference schemes on non-uniform grids fro incompressible Navier-Stokes equations, Journal of Computational Physics, 2007, 224, pp. 1064-1094.

Sterling, J.D., Chen, S., Stability analysis of lattice Boltzmann methods, Journal of Computational Physics, 1996, 123, pp. 196-206.

Succi, S., The lattice Boltzmann equation for fluid dynamics and beyond, Oxford University Press, 2001.

Wang, D., Turek, S., Fictitious boundary and moving mesh methods for the numerical simulation of rigid particulate flows, Journal of Computational Physics, 2007, 222, pp. 28-56.

Wieselsberger, C., New data on the laws of fluid resistance, National Advisory Committee for Aeronautics, 1922, 84.

Wu, J., Shu, C., Implicit velocity correction-based immersed boundary-lattice Boltzmann method and its applications, Journal of Computational Physics, 2009, 228, pp. 1963-1979.

2

Extension of the lattice Boltzmann method for predicting moving particles

2.1 Introduction

The lattice Boltzmann method (LBM) [Chen & Doolen, 1998] has come into use for predicting and modeling fluid flows. Owing to its easy programming and suitability for parallel computing, LBM has been widely used for predicting various flows such as flows in porous medium [Guo & Zhao, 2002], turbulent flows [Martinez et al., 1994], and two-phase flows [Shan & Chen, 1993; Matsukuma et al., 2010; Yu & Fan, 2011]. LBM however has some restrictions, e.g., (1) when the relaxation time is decreased while keeping the relevant dimensionless numbers constant, the spatial resolution needs to be increased to stably calculate flows at high Reynolds numbers [Sterling & Chen, 1996; Cao et al., 1997], and (2) the Lagrangian nature of LBE requires that a discrete particle moves from a lattice point to its neighbor during one time step, and therefore, the lattice spacing and the time step size cannot be altered independently.

An alternative approach to mitigate the latter restriction was proposed by Cao [1997]. The discrete Boltzmann equation is utilized instead of LBE and is solved using ordinary finite difference methods to assign the lattice spacing and the time step size independently. This class of LBM is referred to as a finite difference lattice Boltzmann method (FDLBM). Tsutahara et al. [Tsutahara et al, 2002] made a further improvement of FDLBM by introducing an additional collision term into the discrete Boltzmann equation. It works as a negative viscosity in the macroscopic level, with which the viscosity can be altered without changing the relaxation time and the spatial resolution.

Various methods combining LBM and an immersed boundary method (Immersed Boundary LBM: IB-LBM) have been recently developed for predicting liquid-solid two-phase flows [Feng & Michelaides, 2004; 2005; 2009; Wu & Shu, 2009; Lin et al., 2010; Kang & Hassan, 2010], and several particulate flows have been successfully simulated such as a drafting-kissing-tumbling (DKT) motion of two particles or sedimentation of thousands of particles. IB-LBM is however subject to the above-mentioned restrictions of LBM.

In this study, a combination of FDLBM and an immersed boundary method is proposed to mitigate these restrictions of IB-LBM. Simulations of moving particles at moderate Reynolds numbers are carried out for the validation of the proposed method: (1) two- and three-dimensional single particles falling in a liquid, and (2) a drafting-kissing-tumbling (DKT) motion of two particles in two and three dimensions.

2.2 Numerical method

2.2.1 Finite difference lattice Boltzmann method

The discrete Boltzmann equation based on the single-relaxation time collision model for single phase flows is given by [Cao, 1997]

$$\frac{\partial f_i}{\partial t} + \boldsymbol{c}_i \cdot \nabla f_i = -\frac{1}{\tau}(f_i - f_i^{eq}) \tag{2.1}$$

Tsutahara et al. [2002] replaced the distribution function in the advection term with the following distribution function including an additional collision term for numerical stability:

$$g_i = f_i - \frac{A}{\tau}(f_i - f_i^{eq}) \tag{2.2}$$

where A is a parameter, which works as a negative viscosity in the macroscopic level. This modification enables us to change the viscosity without changing the relaxation time and the spatial resolution. A is a positive number, and its coefficient can be chosen arbitrarily up to 100 [Tsutahara et al., 2008]. However it has been often set at 1/2 as in the standard LBM. The discrete Boltzmann equation including the additional collision term is given by

$$\frac{\partial f_i}{\partial t} + \boldsymbol{c}_i \cdot \nabla g_i = -\frac{1}{\tau}(f_i - f_i^{eq}) \tag{2.3}$$

The macroscopic fluid density, ρ, and velocity, $\boldsymbol{u}$, are given by Eqs. (1.4) and (1.5), respectively, whereas the kinematic viscosity, ν, is defined as

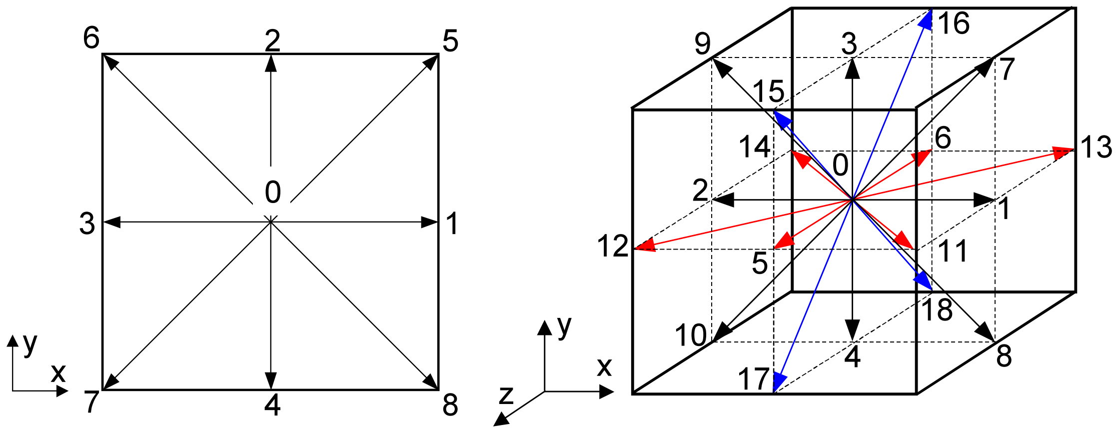

(a) D2Q9 (b) D3Q19

Fig. 2.1 Discrete velocities (the numbers denote the component of the discrete velocity)

$$\nu = c_s^2(\tau - A) \tag{2.4}$$

where the speed of sound, c_S, is $c/\sqrt{3}$, and the lattice velocity, c, is equal to 1. The two-dimensional nine-velocity (D2Q9) model and the three-dimensional nineteen-velocity (D3Q19) model are used for the discrete velocity in two- and three-dimensional calculations, respectively. Figures 2.1 (a) and (b) show the discrete velocities in D2Q9 and D3Q19 models, respectively. The equilibrium velocity distribution function is given by Eq. (1.6). In D2Q9, W_0 = 4/9, W_i = 1/9 for i = 1-4 and W_i = 1/36 for i = 5-8. In D3Q19, W_0 = 1/3, W_i = 1/18 for i = 1-6 and W_i = 1/36 for i = 7-18.

The second-order Runge-Kutta scheme is used for the time integration of Eq. (2.3):

$$f_i^{n+1/2} = f_i^n + \frac{\Delta t}{2}\left[-\boldsymbol{c}_i \cdot \nabla g_i - \frac{1}{\tau}(f_i - f_i^{eq})\right]^n \tag{2.5}$$

$$f_i^{n+1} = f_i^n + \Delta t\left[-\boldsymbol{c}_i \cdot \nabla g_i - \frac{1}{\tau}(f_i - f_i^{eq})\right]^{n+1/2} \tag{2.6}$$

where the superscript n is the discrete time, i.e. $t = n\Delta t$. The advection term is discretized by the following third-order upwind scheme:

$$\frac{\partial g_i}{\partial x} = \frac{g_i(x_{I-2m}, y_J) - 6g_i(x_{I-m}, y_J) + 3g_i(x_I, y_J) + 2g_i(x_{I+m}, y_J)}{6\Delta x} \tag{2.7}$$

where m is the sign function: m = 1 if $c_x > 0$, otherwise $m = -1$. The discretization for the y and z directions is similar. A stability analysis of Eq. (2.3) is carried out in appendix A, and the condition of numerical stability is given by

$$\tau > \frac{\Delta t}{2} \tag{2.8}$$

The condition for incompressibility, $U/c_S < 0.3$ [Chen & Doolen, 1998] must be satisfied in FDLBM as well as in LBM.

An extrapolation method proposed by Watari & Tsutahara [Watari & Tsutahara, 2002] is used for the boundary condition of a computational domain. This method gives distribution functions at the domain boundary by extrapolating the distribution functions at adjacent lattice points.

2.2.1.1 Driven cavity flows

Numerical simulations of two-dimensional incompressible cavity flows are carried out using FDLBM to examine its applicability to high Reynolds numbers. Flows at *Re* = 100, 1000, 5000 and 10000 are simulated. The computational domain is shown in Fig. 2.2. The computational domain size depends on *Re*. Small computational domain sizes are used at *Re*=100 and 1000 and large domains are used at *Re* = 5000 and 10000. The predicted velocity profiles along the *x*- and *y*-axis obtained by using FDLBM are plotted in Figs. 2.3

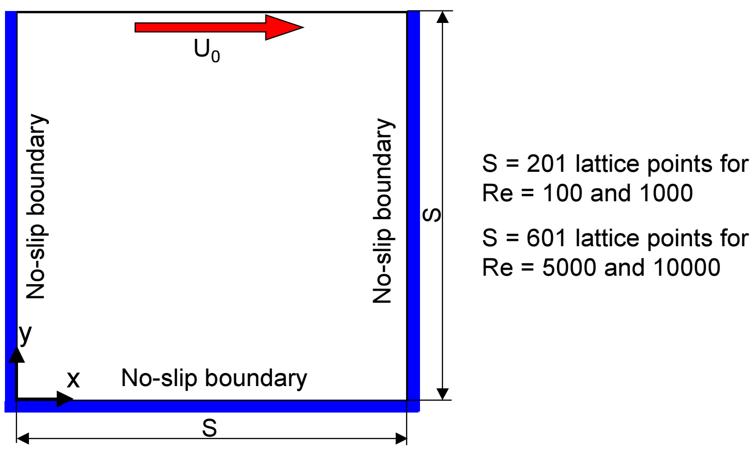

Fig. 2.2 Computational domain for cavity flow

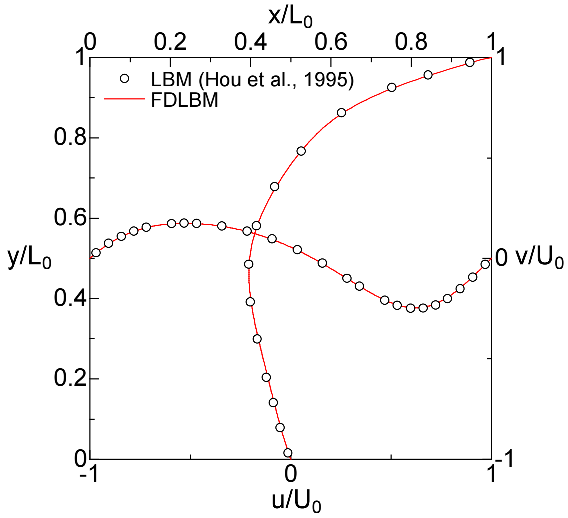

(a) *Re* = 100

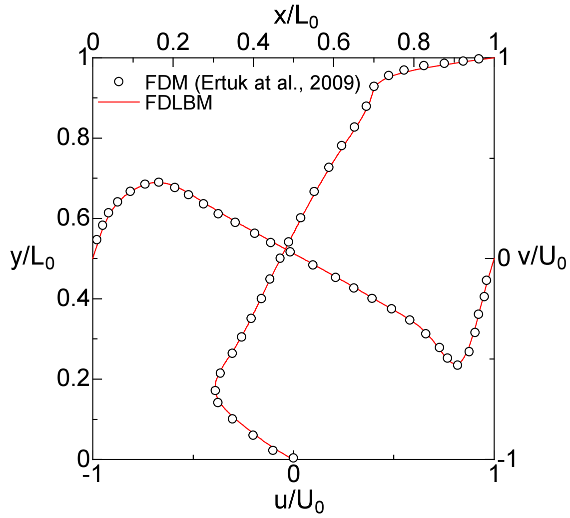

(b) *Re* = 1000

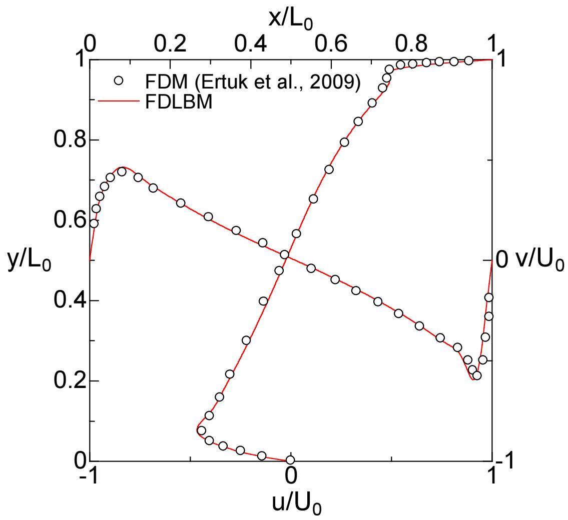

(c) *Re* = 5000

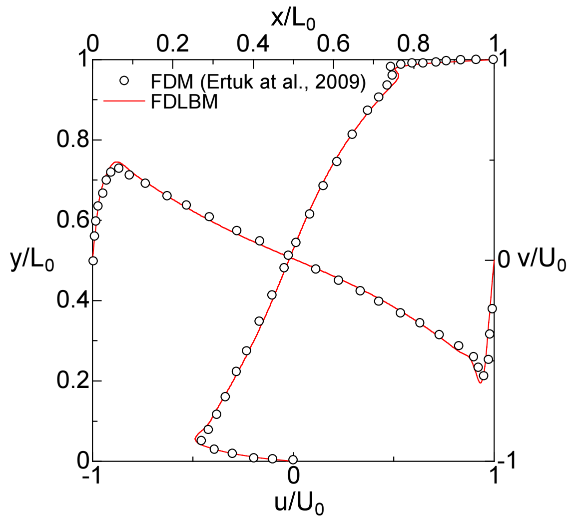

(d) *Re* = 10000

Fig. 2.3 Velocity profiles along the *x*- and *y*-axis of cavity flows at several Reynolds numbers

(a)-(d). These profiles are in good agreement with those of Hou et al. [Hou et al., 1995] and Ertuk [Ertuk, 2009]. The streamlines of the flows show the evolution of the secondary vortices which grow as *Re* increases (Figs. 2.4 (a)-(d)). The formation of these vortices was also predicted by Ertuk [2009]. These results have proved that FDLBM can deal with high Reynolds numbers flows.

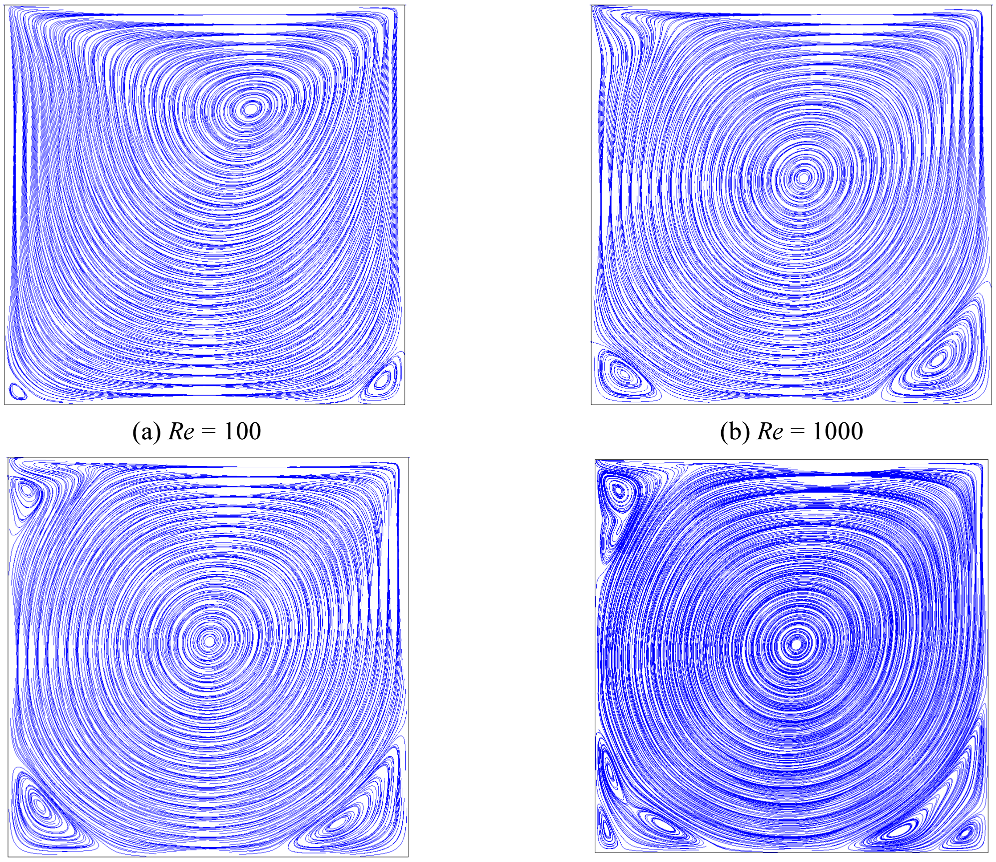

(a) *Re* = 100 (b) *Re* = 1000

(c) *Re* = 5000 (d) *Re* = 10000

Fig. 2.4 Streamlines of cavity flows at several Reynolds numbers

2.2.2 Implementation of the immersed boundary method into FDLBM

The discrete Boltzmann equation including a negative viscosity term, Eq. (2.3), is modified by adding a forcing term, G_i, to impose the boundary condition at immersed boundaries:

$$\frac{\partial f_i}{\partial t} + \boldsymbol{c}_i \cdot \nabla g_i = -\frac{1}{\tau}(f_i - f_i^{eq}) + G_i \tag{2.9}$$

The macroscopic fluid density, ρ, and velocity, $\boldsymbol{u}$, are given by Eqs. (1.4) and (1.5). Applying the Chapman-Enskog expansion to Eq. (2.9) recovers the macroscopic conservation equations for incompressible Newtonian fluids. A detailed explanation of this procedure is given in the next section.

The fluid motion is computed by solving Eq. (2.9) on Eulerian grids, whereas moving bodies immersed in a flow field are represented using Lagrangian points and are tracked by solving an equation of motion. The Eulerian coordinates at the grid point IJK and the coordinates of the Lth Lagrangian point are $\boldsymbol{x}_{IJK} = (x_I, y_I, z_K)$ and $\boldsymbol{X}_L = (X_L, Y_L, Z_L)$, respectively. The external force, $\boldsymbol{G}(\boldsymbol{X}_L, t)$, acting on the fluid to impose the no-slip boundary condition is given by [Dupuis et al., 2008]

$$\boldsymbol{G}(\boldsymbol{X}_L, t) = \rho \frac{\boldsymbol{u}_P(\boldsymbol{X}_L, t) - \boldsymbol{u}(\boldsymbol{X}_L, t)}{\Delta t} \tag{2.10}$$

where Δt is the time step, $\boldsymbol{u}_P(\boldsymbol{X}_L, t)$ the velocity at the Lth Lagrangian point of the solid particle P, and $\boldsymbol{u}(\boldsymbol{X}_L, t)$ the fluid velocity interpolated onto $\boldsymbol{X}_L$. The fluid velocity is interpolated using

$$\boldsymbol{u}(\boldsymbol{X}_L, t) = \sum_{\boldsymbol{x}_{IJK} \in \Delta} \boldsymbol{u}(\boldsymbol{x}_{IJK}, t) \delta(\boldsymbol{x}_{IJK} - \boldsymbol{X}_L) \Delta V \tag{2.11}$$

Here the smoothed delta function δ is given by

$$\delta(\boldsymbol{x}_{IJK} - \boldsymbol{X}_L) = \delta_h\left(\frac{x_I - X_L}{\Delta x}\right) \delta_h\left(\frac{y_J - Y_L}{\Delta y}\right) \delta_h\left(\frac{z_K - Z_L}{\Delta z}\right) \tag{2.12}$$

where the following 4-points cosine delta function [Peskin, 1977; Yang et al., 2009] is used for δ_h:

$$\delta_h(r) = \begin{cases} \dfrac{1}{4}\left[1+\cos\left(\dfrac{\pi|r|}{2}\right)\right] & \text{for } |r| \le 2 \\ 0 & \text{for } |r| > 2 \end{cases} \tag{2.13}$$

The force calculated by using Eq. (2.10) is then distributed onto Eulerian grid points:

$$\boldsymbol{G}(\boldsymbol{x}_{IJK},t) = \sum_{L=1}^{N_m} \boldsymbol{G}(\boldsymbol{X}_L,t)\delta(\boldsymbol{x}_{IJK} - \boldsymbol{X}_L)\Delta S \Delta x \tag{2.14}$$

The external forcing term $G_i(\boldsymbol{x}_{IJK}, t)$ is given by

$$G_i(\boldsymbol{x}_{IJK},t) = 3W_i \boldsymbol{c}_i \cdot \boldsymbol{G}(\boldsymbol{x}_{IJK},t) \tag{2.15}$$

whose moments satisfy $\Sigma_i G_i = 0$ and $\Sigma_i \boldsymbol{c}_i G_i = \boldsymbol{G}$.

Solid particles immersed in a flow field are tracked by solving the following equations:

$$M_P \frac{d\boldsymbol{U}_P}{dt} = \boldsymbol{G}_P \tag{2.16}$$

$$I_P \cdot \frac{d\omega_P}{dt} = \boldsymbol{T}_P \tag{2.17}$$

where M_P is the mass of the particle P, $\boldsymbol{U}_P$ the translational particle velocity, I_P the tensor for moment of inertia, ω_P the angular velocity, $\boldsymbol{T}_P$ the torque, and $\boldsymbol{G}_P$ the force acting on P, which consists of **-*G***, i.e. the reaction force from the fluid, gravity, particle-particle and particle-wall interaction forces and so on, this is, $\boldsymbol{G}_P = -\sum_{L=1}^{N_m} \boldsymbol{G}(\boldsymbol{X}_L,t)\Delta S \Delta x + \left(1 - \frac{\rho}{\rho_P}\right) M_P \boldsymbol{g} + \boldsymbol{F}_P^{col}$ where ρ_P is the particle density, $\boldsymbol{g}$ is the gravity and $\boldsymbol{F}_P^{col}$ is the particle collision forces. The velocity $\boldsymbol{u}_P$ is given by $\boldsymbol{u}_P = \boldsymbol{U}_P + \omega \times (\boldsymbol{X}_L - \boldsymbol{X}_P)$, where $\boldsymbol{X}_P$ is the position vector of the center of gravity of the particle P.

As in FDLBM, the second-order Runge-Kutta scheme is used for the time integration of Eq. (2.9):

$$f_i^{n+1/2} = f_i^n + \frac{\Delta t}{2}\left[-\boldsymbol{c}_i \cdot \nabla g_i - \frac{1}{\tau}(f_i - f_i^{eq}) + G_i \right]^n \tag{2.18}$$

$$f_i^{n+1} = f_i^n + \Delta t\left[-\boldsymbol{c}_i \cdot \nabla g_i - \frac{1}{\tau}(f_i - f_i^{eq}) + G_i \right]^{n+1/2} \tag{2.19}$$

Effects of difference schemes for the advection term, i.e. the second-order central difference scheme, first- and second-order upwind schemes, on planar Couette flows have been examined. Consequently, the third-order upwind scheme is used in this study because it gives the most accurate prediction.

The equation of motion is discretized as

$$\boldsymbol{U}_P^{n+1} = \boldsymbol{U}_P^n + (\boldsymbol{U}_P^n - \boldsymbol{U}_P^{n-1})\frac{\rho}{\rho_P} + \frac{\boldsymbol{G}_P \Delta t}{M_P} \tag{2.20}$$

The second term in the R.H.S. is introduced by Feng & Michaelides [Feng & Michaelides, 2009] to stably simulate particles of $\rho_P \approx \rho$. The particle position is updated using

$$\boldsymbol{X}_P^{n+1} = \boldsymbol{X}_P^n + \frac{\Delta t}{2}(\boldsymbol{U}_P^{n+1} + \boldsymbol{U}_P^n) \tag{2.21}$$

Equation (2.17) is discretized similarly:

$$I_P \cdot \omega_P^{n+1} = I_P\left[\omega_P^n + (\omega_P^n - \omega_P^{n-1})\frac{\rho}{\rho_P} \right] + \boldsymbol{T}_P \Delta t \tag{2.22}$$

2.2.3 Parallel computation of IB-FDLBM

In order to enhance the efficiency of the calculations with IB-FDLBM, OpenMP has been adopted for parallel computation of Eqs. (2.18) and (2.19). The implementation of OpenMP is straightforward, and no modifications of the code are needed. An example of the implementation of OpenMP code is given in the following:

```
!$ use omp_lib
!$ call omp_set_num_threads(l)
!$ omp parallel private (m)
!$ omp do
   do m = 1, m_max
      f(m) = f_old(m) + Δt[A(m) + C(m) + F(m)]_old
   end do
!$ omp end do
!$ omp end parallel
```

where l is the number of threads and it can be as high as the number of threads in the CPU, and m is an integer variable representing the number of lattice points in each direction of the coordinate axes or the number of discrete velocities, A stands for the advection term, C for the collision term and F for the direct-forcing term.

2.2.4 Derivation of the macroscopic conservation equations

Derivation of the macroscopic equations, i.e. the continuity and the Navier-Stokes equations, from the discrete Boltzmann equation is carried out by using the Chapman Enskog expansion:

$$f_i = f_i^{(0)} + \varepsilon f_i^{(1)} + \varepsilon^2 f_i^{(2)} + ... \qquad (2.23)$$

$$\frac{\partial}{\partial t} = \varepsilon \frac{\partial}{\partial t_1} + \varepsilon^2 \frac{\partial}{\partial t_2} \tag{2.24}$$

$$\frac{\partial}{\partial x_\alpha} = \varepsilon \frac{\partial}{\partial x_\alpha} \tag{2.25}$$

where ε is the Knudsen number. The first four moments of the equilibrium distribution function of the D2Q9 or D3Q19 models are

$$\sum f_i^{eq} = \rho \tag{2.26}$$

$$\sum f_i^{eq} c_{i\alpha} = \rho u_\alpha \tag{2.27}$$

$$\sum f_i^{eq} c_{i\alpha} c_{i\beta} = \frac{1}{3}\rho\delta_{\alpha\beta} + \rho u_\alpha u_\beta \tag{2.28}$$

$$\sum f_i^{eq} c_{i\alpha} c_{i\beta} c_{i\gamma} = \rho u_\alpha u_\beta u_\gamma + \frac{1}{3}\rho\left(u_\alpha \delta_{\beta\gamma} + u_\beta \delta_{\alpha\gamma} + u_\gamma \delta_{\alpha\beta}\right) \tag{2.29}$$

Substituting Eqs. (2.23)-(2.25) into Eq. (2.9) yields the following equations for the orders of ε^0, ε^1 and ε^2:

$$\varepsilon^0 : f_i^{(0)} = f_i^{eq} \tag{2.30}$$

$$\varepsilon^1 : \frac{\partial}{\partial t_1} f_i^{(0)} + c_{i\alpha} \frac{\partial}{\partial x_\alpha} f_i^{(0)} = -\frac{1}{\tau} f_i^{(1)+} + G_i \tag{2.31}$$

$$\varepsilon^2 : \frac{\partial}{\partial t_1} f_i^{(1)} + \frac{\partial}{\partial t_2} f_i^{(0)} + c_{i\alpha} \frac{\partial}{\partial x_\alpha} f_i^{(1)} - \frac{Ac_{i\alpha}}{\tau} \frac{\partial}{\partial x_\alpha} f_i^{(1)} = -\frac{1}{\tau} f_i^{(2)} \tag{2.32}$$

Summing Eqs. (2.30) - (2.32) over *i* yields

$$\sum f_i^{(l)} = 0 \quad \text{for } l \geq 1 \tag{2.33}$$

$$\frac{\partial \rho}{\partial t_1} + \frac{\partial \rho u_\alpha}{\partial x_\alpha} = 0 \tag{2.34}$$

$$\frac{\partial \rho}{\partial t_2} = 0 \tag{2.35}$$

Combining Eqs. (2.34) and (2.35) gives the continuity equation:

$$\frac{\partial \rho}{\partial t} + \frac{\partial \rho u_\alpha}{\partial x_\alpha} = 0 \tag{2.36}$$

Multiplying Eqs. (2.30) - (2.32) by $c_{i\alpha}$ and summing the resultant equations over i yields

$$\sum c_{i\alpha} f_i^{(l)} = 0 \quad \text{for } l \geq 1 \tag{2.37}$$

$$\frac{\partial \rho u_\alpha}{\partial t_1} + \frac{\partial}{\partial x_\beta}\left(\frac{1}{3}\rho\delta_{\alpha\beta} + \rho u_\alpha u_\beta\right) = G_\alpha \tag{2.38}$$

$$\frac{\partial \rho u_\alpha}{\partial t_2} - (\tau - A)\frac{\partial}{\partial x_\beta}\left(\frac{1}{3}\rho\frac{\partial u_\alpha}{\partial x_\beta} + \frac{1}{3}\rho\frac{\partial u_\beta}{\partial x_\alpha}\right) + (\tau - A)\frac{\partial}{\partial x_\alpha}\left(\frac{\partial u_\alpha u_\beta u_\gamma \rho}{\partial x_\beta}\right) = 0 \tag{2.39}$$

Combining Eqs. (2.38) and (2.39) yields the Navier-Stokes equation:

$$\frac{\partial \rho u_\alpha}{\partial t} + \frac{\partial \rho u_\alpha u_\beta}{\partial x_\beta} = -\frac{\partial p}{\partial x_\alpha} + \nu\frac{\partial}{\partial x_\beta}\left[\rho\left(\frac{\partial u_\alpha}{\partial x_\beta} + \frac{\partial u_\beta}{\partial x_\alpha}\right)\right] + G_\alpha \tag{2.40}$$

where the pressure p and the viscosity ν, are given by

$$p = \frac{\rho}{3} \tag{2.41}$$

$$\nu = \frac{1}{3}(\tau - A) \tag{2.42}$$

2.3 Applicability of IB-FDLBM to moving particles at moderate Reynolds numbers

2.3.1 Sedimentation of single particles falling through stagnant liquids

A falling particle in a liquid-filled container is one of the typical benchmark tests of moving boundary problems for validating immersed boundary methods [Feng & Michaelides, 2004; Lin et al. 2010]. A two-dimensional simulation is first carried out. Figure 2.5 shows the computational domain. All the domain boundaries are no-slip walls. The initial particle position is (x, y) = (1 cm, 4 cm), and the particle is initially at rest. The fluid and particle densities are 1.0×10^3 kg/m^3 and 1.25×10^3 kg/m^3, respectively. The viscosity is 1.0×10^{-2} Pa·s. The magnitude of acceleration of gravity, g, is 9.81 m/s^2. The particle diameter is 0.25 cm. The numbers of lattice points in the x and y directions are 201 and 601, respectively. The parameters for collision are τ = 0.65 and A = 0.5. The time step size is 5×10^{-6} s. The number of Lagrangian points at the particle surface is 360.

The particle falls rectilinearly as shown in Figs. 2.6 (a)-(d). The vorticity contour shows that the symmetric wake structure is formed behind the particle due to the rectilinear motion. The temporal change in the vertical position, Y_P, of the particle and Re defined using the falling velocity are shown in Fig. 2.7. The particle accelerates and reaches its terminal condition. Then the velocity is suddenly retarded just before reaching the bottom wall. The present method gives the same prediction as that obtained by a finite element method [Wan & Turek, 2006] and that obtained by using an IB-LBM proposed by Dupuis et al. [2008].

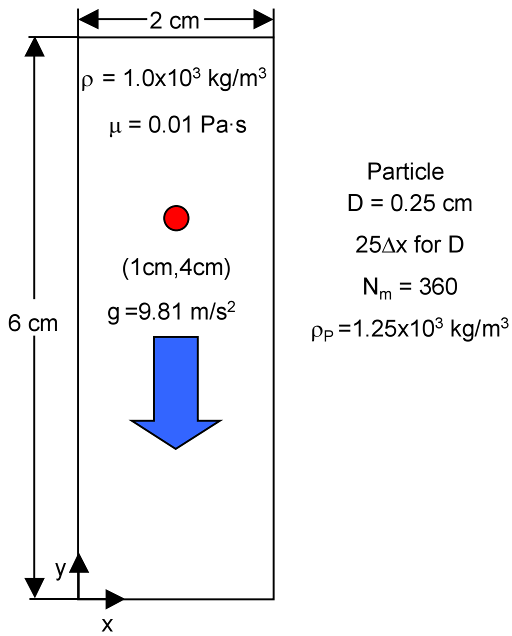

Fig. 2.5 Computational domain of a single two-dimensional falling particle

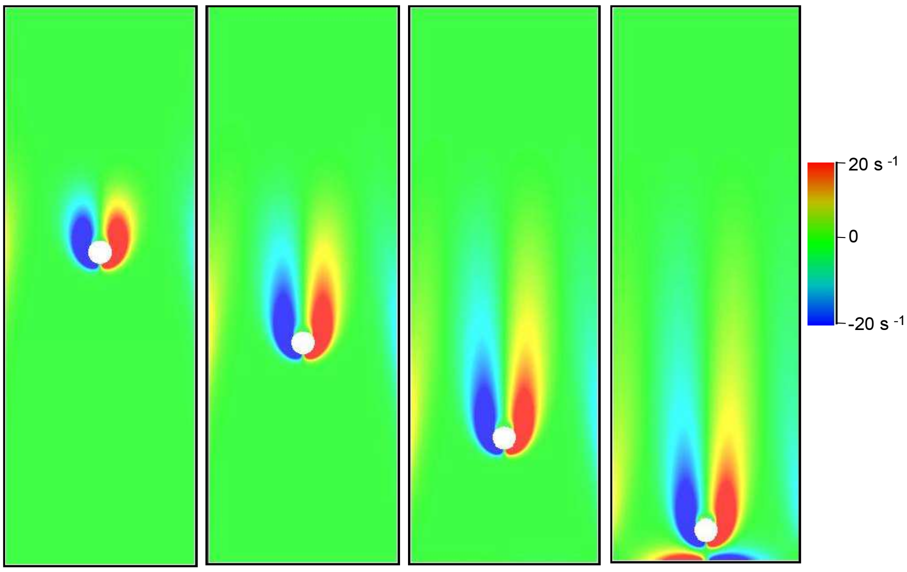

(a) *t* =0.19 s (b) 0.38 s (c) 0.57 s (d) 0.76 s

Fig. 2.6 Vorticity contour of a single two-dimensional falling particle

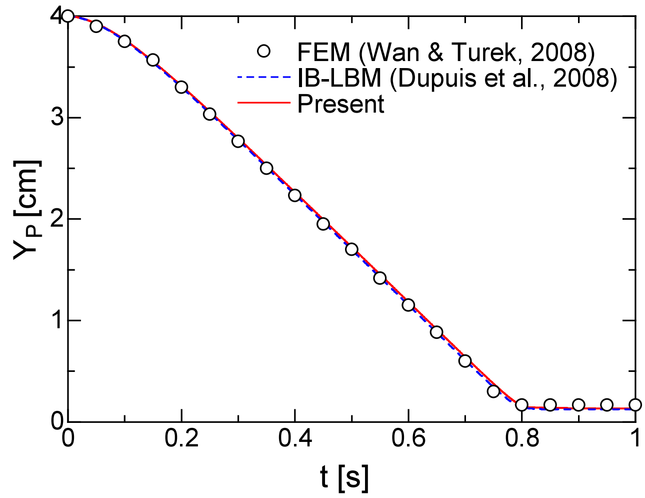

(a)

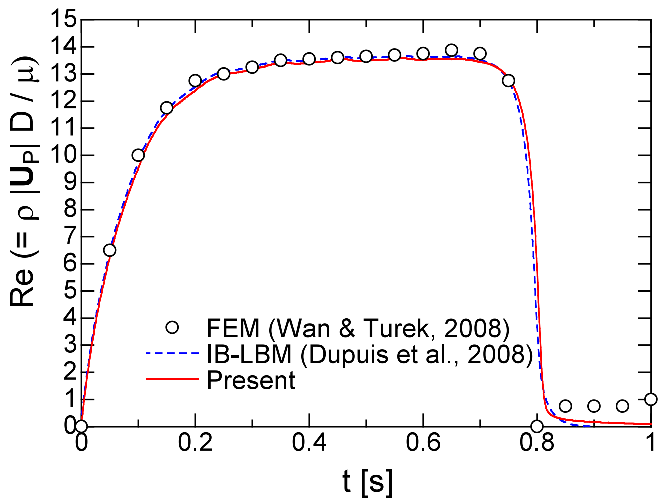

(b)

Fig. 2.7 Particle position and Reynolds number of a single two-dimensional falling particle

Single spherical particles falling through a stagnant liquid in a container are also simulated with IB-FDLBM. The numerical condition is similar to the experiments performed by ten Cate et al. [2002]. The dimensions of the container are 10 cm, 10 cm, and 16 cm in the *x*, *y* and *z* directions, respectively. The lattice spacing is 0.1 cm. Therefore the numbers of lattice points in the *x*, *y* and *z* directions are 101, 101, and 161, respectively. The fluid properties and other computational parameters are summarized in Table 2.1. The acceleration of gravity is (0, 0, -9.8 m/s^2). The initial sphere location is (5 cm, 5 cm, 12.75 cm), and the sphere is initially at rest. The particle density is 1120 kg/m^3 and the diameter is 1.5 cm. Lagrangian points are generated by using the method proposed by Feng & Michaelides [2005]. The number of Lagrangian points is 762, and they are evenly distributed on the sphere surface. The negative viscosity tern, A, is 0.5.

Figures 2.8-2.11 show snapshots of the vorticity contour and the motion of falling spheres for cases 1-4. As can be seen, the motion of particles is similar in all the cases, i.e. the particles fall rectilinearly and a symmetric wake structure is formed behind the particle, and then the particle reaches the bottom wall. The particle velocity increases as the viscosity of the flow decreases. Figure 2.12 shows a comparison of the time evolution of the falling velocity with the measured data [ten Cate et al., 2002]. Good agreements are obtained with IB-FDLBM.

Table 2.1 Computational parameters for a sphere falling through liquid with IB-FDLBM

Case	Density, ρ [kg/m^3]	Viscosity, μ [Pa·s]	Relaxation time τ	Time step [s]
1	970	373×10^{-3}	0.86	1.56×10^{-4}
2	965	212×10^{-3}	0.86	2.73×10^{-4}
3	962	113×10^{-3}	0.74	3.405×10^{-4}
4	960	58×10^{-3}	0.64	4.14×10^{-4}

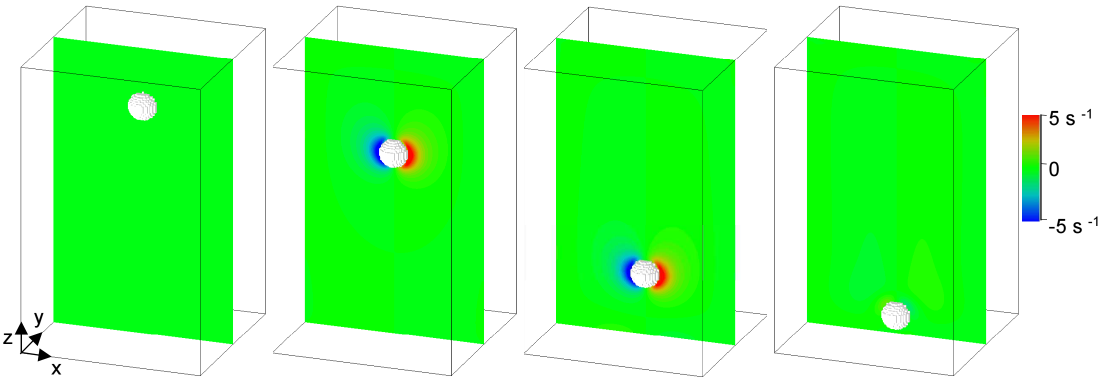

(a) *t* =0 s (b) 1 s (c) 3 s (d) 4 s

Fig. 2.8 Vorticity contour of a single three-dimensional falling particle (Case 1)

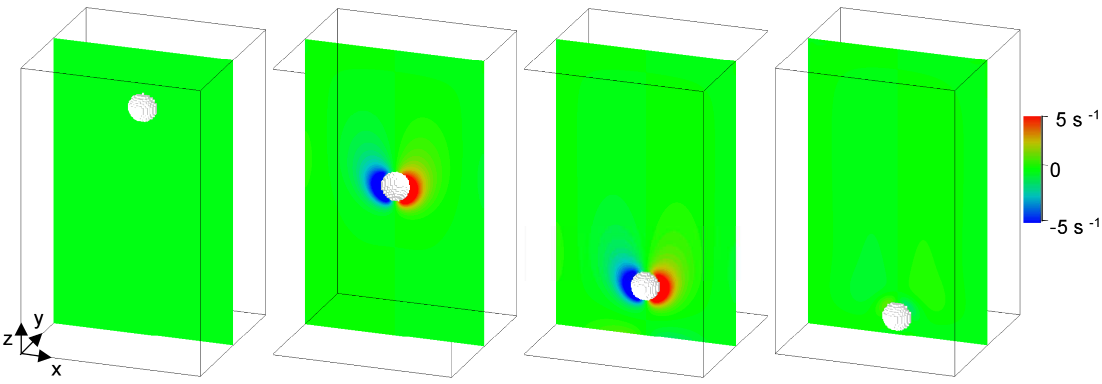

(a) *t* =0 s (b) 1 s (c) 2 s (d) 2.5 s

Fig. 2.9 Vorticity contour of a single three-dimensional falling particle (Case 2)

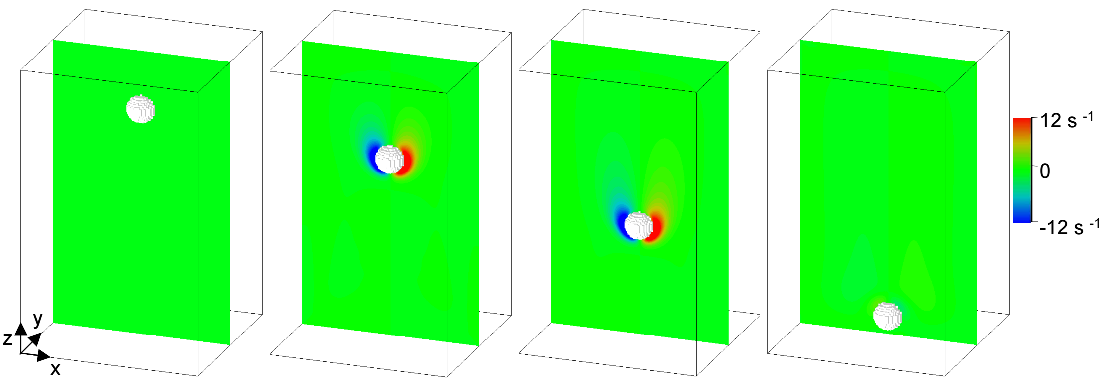

(a) *t* =0 s (b) 0.5 s (c) 1 s (d) 1.5 s

Fig. 2.10 Vorticity contour of a single three-dimensional falling particle (Case 3)

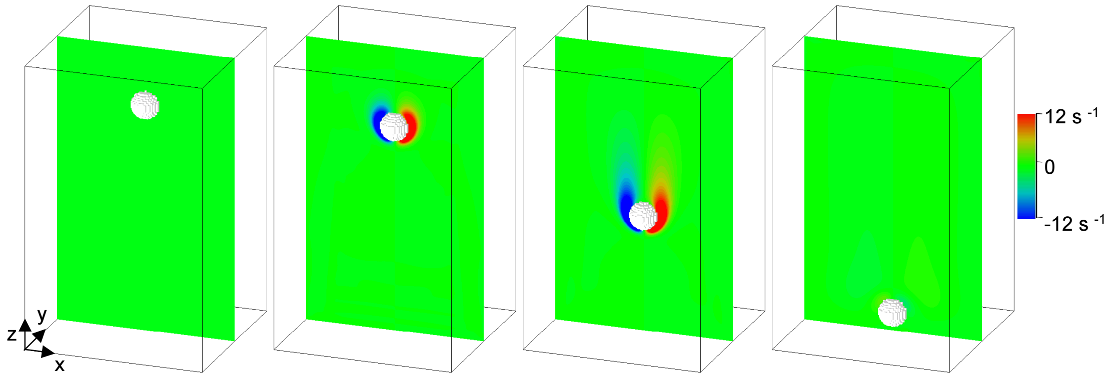

(a) t =0 s (b) 0.25 s (c) 0.75 s (d) 1.5 s

Fig. 2.11 Vorticity contour of a single three-dimensional falling particle (Case 4)

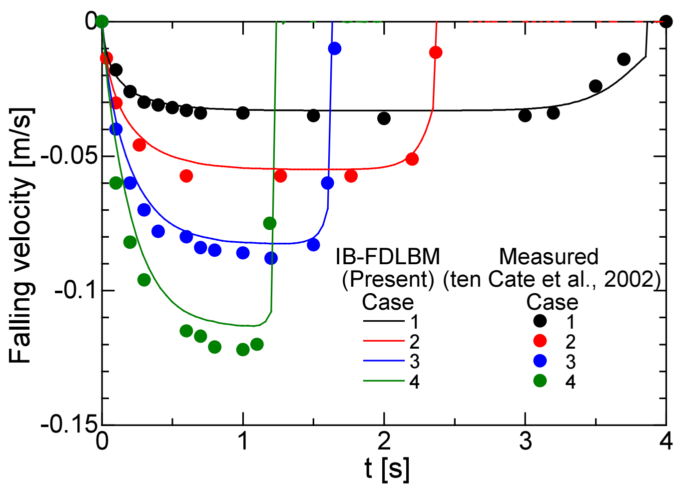

Fig. 2.12 Velocities of single spherical falling particle

Then, single square particles falling through liquid are simulated to prove that the proposed method can deal with non-circular shapes. Figure 2.13 shows the computational domain. All the domain boundaries are no-slip walls. The initial particle position is (x, y) = (1 cm, 4 cm), and the particle is initially at rest. The fluid and particle densities are 1.0×10^3 kg/m^3 and 1.25×10^3 kg/m^3, respectively. The viscosity is 1.0×10^{-2} Pa·s. The magnitude of acceleration of gravity is 9.81 m/s^2. The width of the square is 0.21 cm, and the angle of incidence, θ, is 45°. The numbers of lattice points in the x and y directions are 201 and 601, respectively. τ is 0.65 and A is 0.5. The time step size is 5×10^{-6} s. The number of Lagrangian points at the particle surface is 100.

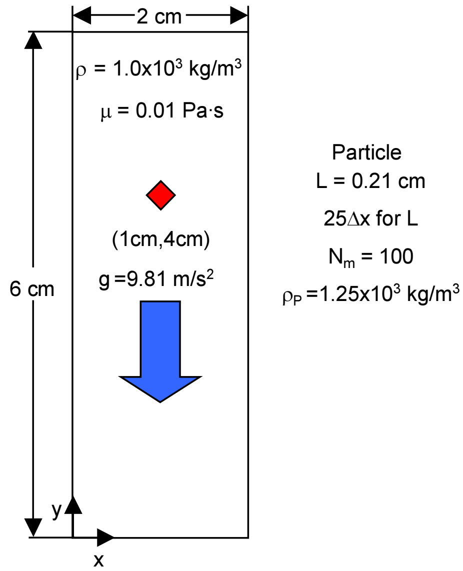

Fig. 2.13 Computational domain of a single square particle falling in a stagnant liquid

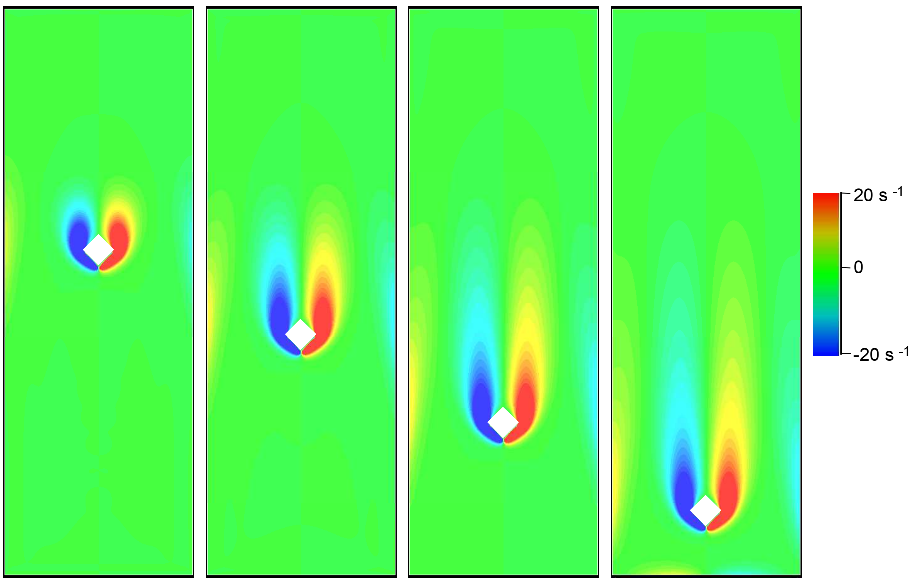

(a) t =0.2 s (b) 0.4 s (c) 0.6 s (d) 0.8 s

Fig. 2.14 Vorticity contour of a single square falling particle at θ = 45°

The particle falls rectilinearly as shown in Figs. 2.14 (a) - (d). The vorticity contour shows that the symmetric wake structure is formed behind the edges of the particle due to the rectilinear motion. The particle path in the vertical position, Y_P, and the time variation of *Re* are shown in Figs. 2.15 (a) and (b). The predictions are similar to those obtained for the single circular particle.

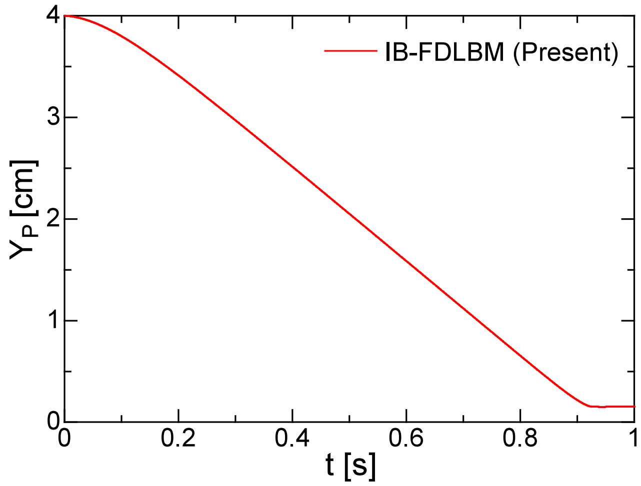

(a)

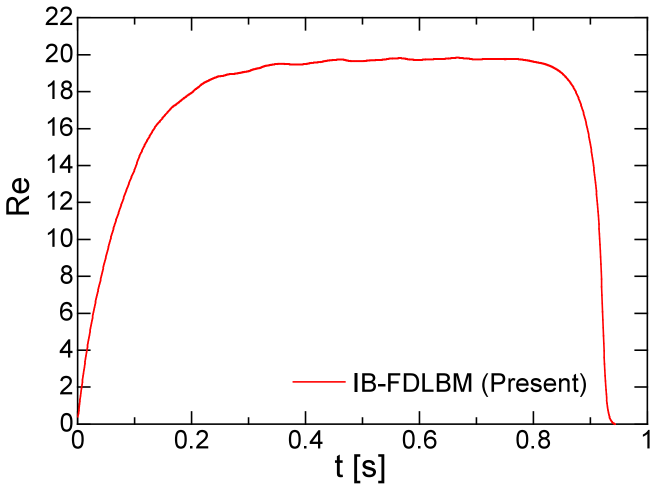

(b)

Fig. 2.15 Particle position and Reynolds number of a single square falling particle θ = 45°

2.3.2 Drafting-kissing-tumbling motion of two particles

A problem of two particles with DKT has been used as a benchmark problem for validating IB-LBMs [Feng & Michaelides, 2004; Lin et al., 2010; Niu et al., 2006]. Figure 2.16 shows the computational domain. All the walls are no-slip walls. The particles, P1 and P2, are initially located at (1 cm, 6.8 cm) and (0.999 cm, 7.2 cm), respectively, and the initial velocities are zero. The other input parameters are as follows: $\rho = 1.0\times10^3$ kg/m^3, $\rho_P = 1.01\times10^3$ kg/m^3, $\mu = 1.0\times10^{-3}$ Pa·s, $g = 9.81$ m/s^2, $D = 0.20$ cm, $\tau = 0.65$, $A = 0.5$ and $\Delta t = 5\times10^{-5}$ s. The numbers of lattice points in the x and y directions are 201 and 801, respectively. For particle-particle and particle-wall collisions, the models proposed by Glowinski et al. [Glowinsky at al., 1999] are adopted. For particle-particle collision, the repulsive force, $\boldsymbol{F}_{PP'}$, between the particles P and P' is given by

$$\boldsymbol{F}_{PP'} = \begin{cases} \dfrac{c_{PP'}}{\varepsilon_P}\left[\dfrac{|\boldsymbol{X}_P - \boldsymbol{X}_{P'}| - R_P - R_{P'} - \zeta_P}{\zeta_P}\right]\dfrac{\boldsymbol{X}_P - \boldsymbol{X}_{P'}}{|\boldsymbol{X}_P - \boldsymbol{X}_{P'}|} & \text{for } |\boldsymbol{X}_P - \boldsymbol{X}_{P'}| > R_P + R_{P'} + \zeta_P \\ 0 & \text{otherwise,} \end{cases} \tag{2.43}$$

where R_P and $R_{P'}$ are the radii of the particles P and P', respectively. For particle-wall collision, the repulsive force, $\boldsymbol{F}_{PW}$, acting on the particle P is given by

$$\boldsymbol{F}_{PW} = \begin{cases} \dfrac{c_{PW}}{\varepsilon_W}\left[\dfrac{|\boldsymbol{X}_P - \boldsymbol{X}_W| - 2R_P - \zeta_W}{\zeta_W}\right]\dfrac{\boldsymbol{X}_P - \boldsymbol{X}_W}{|\boldsymbol{X}_P - \boldsymbol{X}_W|} & \text{for } |\boldsymbol{X}_P - \boldsymbol{X}_W| > 2R_P + \zeta_W \\ 0 & \text{otherwise,} \end{cases} \tag{2.44}$$

where $\varepsilon_P = \varepsilon_W = 2.0$, $\zeta_P = \zeta_W = 3$ and $c_{PP'} = c_{PW} = (\rho_P - \rho)\pi R_P^2 g$.

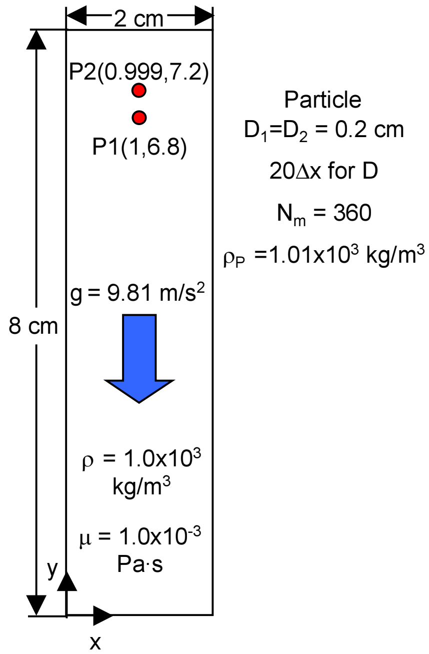

Fig. 2.16 Computational domain of two-dimensional DKT motion of two particles

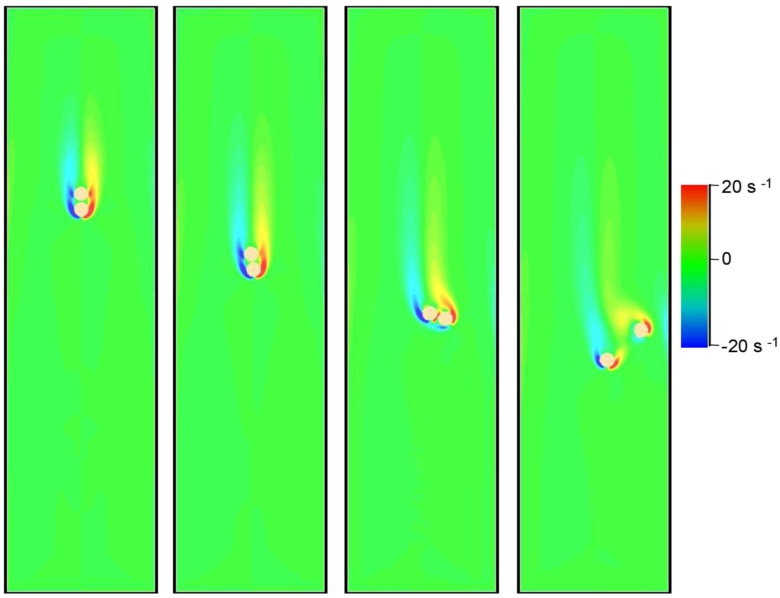

Drafting Kissing Tumbling

(a) t = 1.5 s (b) 2 s (c) 2.5 s (d) 3 s

Fig. 2.17 Two-dimensional DKT motion of two particles

Successive images of the predicted particles and vorticity contour are shown in Figs. 2.17 (a)-(d). The particles show drafting (t = 1.5 s), kissing (t = 2 s) and tumbling motions (t = 3 s). The particle paths in the x and y directions are compared with those predicted using IB-LBMs [Dupuis et al., 2008; Niu et al., 2006]. As shown in Figs. 2.18, good agreement is obtained, and therefore, the proposed method is applicable to problems involving multiple particles interacting with each other.

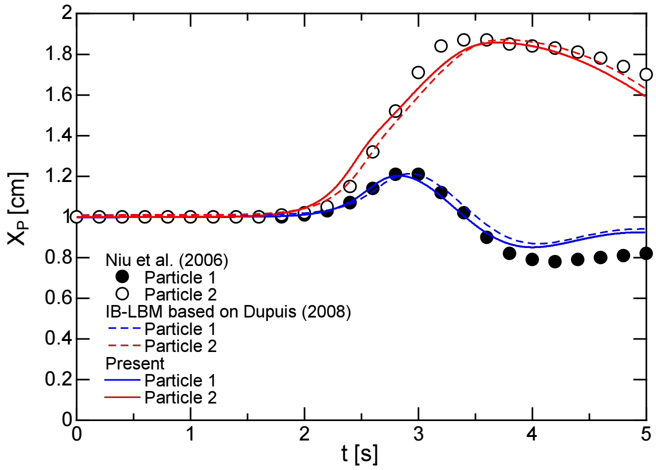

(a) X_P

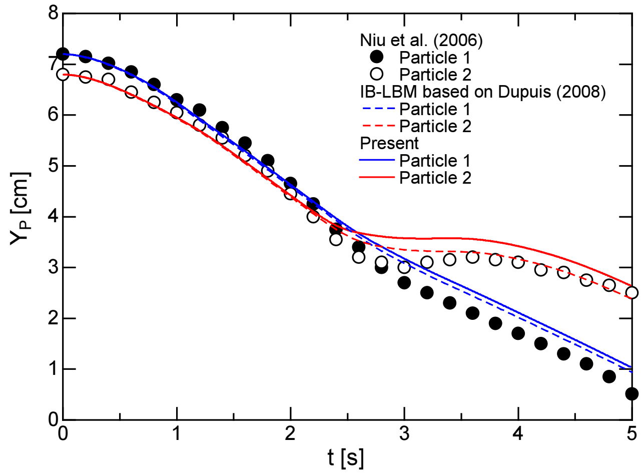

(b) Y_P

Fig. 2.18 Particle position (X_P, Y_P) in two-dimensional DTK motion of two particles

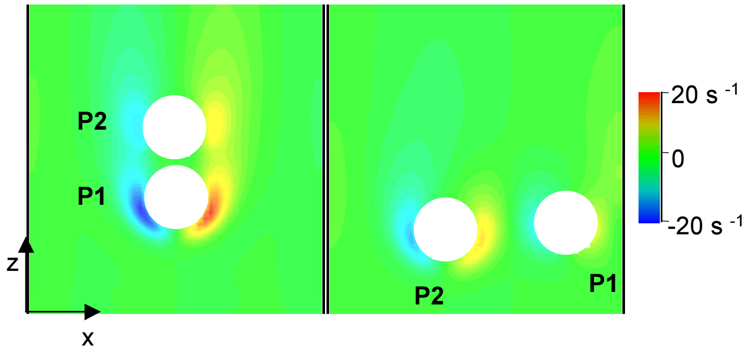

(a) Drafting at $t = 2$ s (b) Tumbling at $t = 6$ s

Fig. 2.19 DTK motion of two spherical particles

A three-dimensional simulation of two spherical particles is also carried out. The computational domain size is 1, 1 and 16 cm in the x, y and z directions. The lattice width is 0.02 cm and the numbers of grid points are 51, 51, and 801. Both particles have the same diameter 0.2 cm, and the density is 1010 kg/m^3. The number of Lagrangian points is 346 for each particle. The initial positions of the particles, P1 and P2, are (0.5 cm, 0.5 cm, 14.8 cm) and (0.498 cm, 0.499 cm, 15.2 cm). The fluid density and viscosity are 1000 kg/m^3 and 1×10^{-3} Pa·s. The single relaxation time is set at 0.575, and the time step is 0.5×10^{-3} s. Figures 2.19 and 2.20 show the predicted particle motion and positions of the center of gravity (X_P,Y_P,Z_P) of P1 and P2. The motion patterns in the x direction are similar to those obtained in the two-dimensional calculations. The DTK motion is reasonably simulated in three dimensions.

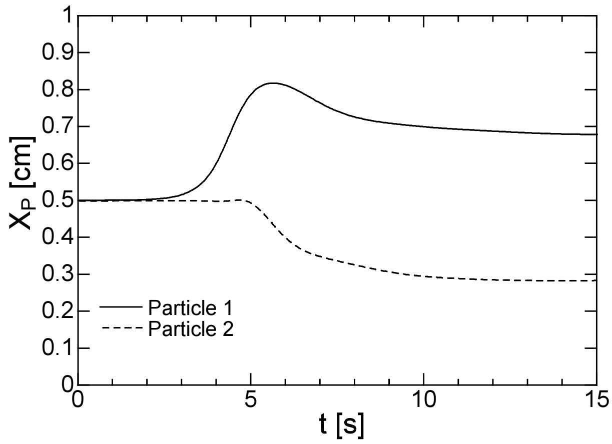

(a) X_P

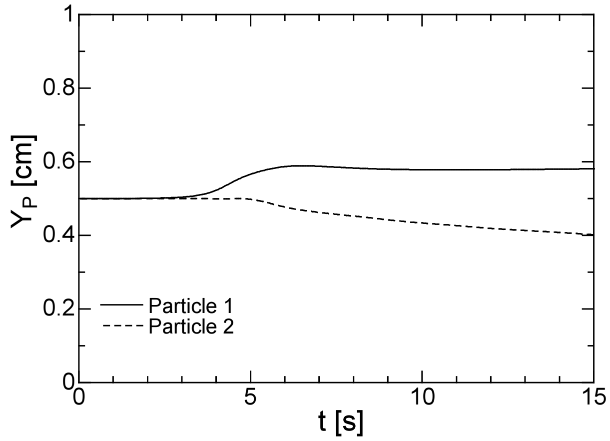

(b) Y_P

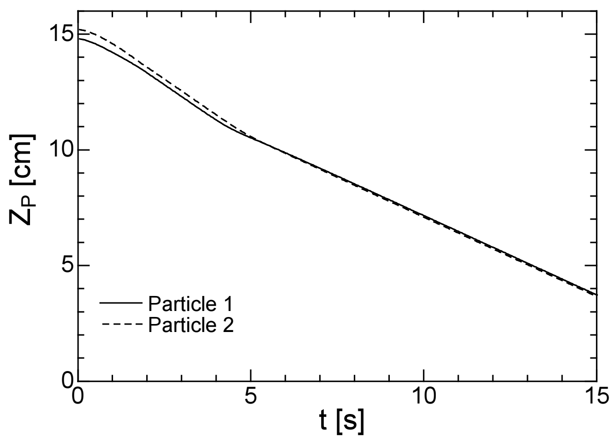

(c) Z_P

Fig. 2.20 Particle path of DTK motion of two spherical particles computed using IB-FDLBM

2.4 Conclusions

A lattice Boltzmann method (LBM) for predicting fluid-solid flows was proposed. The method is a combination of a finite difference lattice Boltzmann method (FDLBM) based on a discrete Boltzmann equation and an immersed boundary method (IBM). The FDLBM allows us to set the lattice spacing and the time step independently. An additional collision term, which works as a negative viscosity in the macroscopic scale, is added for numerical stability. IBM is based on the direct-forcing method, in which an external forcing term to impose the boundary condition at the immersed boundaries is added to the discrete Boltzmann equation. The force is calculated at Lagrangian points at the immersed boundary and is distributed onto Eulerian grids. The proposed method was validated through the following benchmark tests: a single particle falling in a liquid and interaction of two falling particles. As a result, the following conclusions were obtained:

(1) The motions of particles falling through liquids predicted using IB-FDLBM quantitatively agree with those obtained using IB-LBMs.

(2) The proposed method well predicts the interaction between two falling particles, e.g., the drafting-kissing-tumbling motion.

References

Cao, N., Chen, S., Jin, S., Martinez, D., Physical symmetry and lattice symmetry in the lattice Boltzmann method, Physical Review E, 1997, 55(1), pp. 21-24.

Chen, S., Doolen, G. D., Lattice Boltzmann method for fluid flows, Annual Review of

Fluid Mechanics, 1998, 30, pp. 329-364.

Dupuis, A., Chatelain, P., Koumoutsakos, P., An immersed boundary–lattice-Boltzmann method for the simulation of the flow past an impulsively started cylinder, Journal of Computational Physics, 227 (2008) pp. 4486-4498.

Ertuk, E., Corke, T. C., Gokcol, C., Numerical simulations of "2-D steady incompressible driven cavity flow at high Reynolds numbers, International Journal for Numerical Methods in Fluids, 2005, 48, pp. 747-774.

Feng, Z.-G., Michaelides, E. E., The immersed boundary-lattice Boltzmann method for solving fluid-particles interaction problems, Journal of Computational Physics, 2004, 195, pp. 602-628.

Feng, Z.-G., Michaelides, E. E., Proteus: a direct forcing method in the simulations of particulate flows, Journal of Computational Physics, 2005, 202, pp. 20-51.

Feng, Z.-G., Michaelides, E. E., Robust treatment of no-slip boundary condition and velocity updating for the lattice-Boltzmann simulation of particulate flows, Computers and Fluids, 2009, 38, pp. 370-381.

Glowinski, R., Pan, T.-W., Hesla, T. I., Joseph, D. D., A distributed Lagrange multiplier/fictitious domain method for particulate flows, International Journal of Multiphase Flow, 25(5), (1999) pp. 755-794.

Guo, Z., Zhao, T. S., Lattice Boltzmann model for incompressible flows through porous media, Physical Review E, 2002, 66, 036304.

Hou, S., Zou, Q., Chen, S., Doolen, G., Cogley, A. C., Simulation of cavity flow by the lattice Boltzmann method, Journal of Computational Physics, 1995, 118, pp. 329-347.

Kang, S. K., Hassan, Y. A., A comparative study of direct-forcing immersed boundary-lattice Boltzmann methods for stationary complex boundaries, International Journal for Numerical Methods in Fluids, 2010, DOI: 10.1002/fld.2304.

Lin, S.-Y., Lin, C.-T., Chin, Y.-H., Tai, Y.-H., A direct-forcing pressure-based lattice Boltzmann method for solving fluid-particle interaction problems, International Journal for Numerical Methods in Fluids, 2010, DOI: 10.1002/fld.2442.

Martinez, D. O., Matthaeus, W. H., Chen, S., Montgomery, D. C., Comparison of spectral method and lattice Boltzmann simulations of two-dimensional hydrodynamics, Physics of Fluids, 1994, 6, pp. 1285-1298.

Matsukuma, Y., Koga, Y., Minemoto, M., Inoue, G., Numerical simulations of droplet upwelling into gas channel of PEFC by lattice Boltzmann method, Japanese Journal of Multiphase Flow, 2010, 23(5), pp. 515-521. (in Japanese)

Niu, X. D., Shu, C., Chew, Y. T., Peng, Y., A momentum exchange-based immersed boundary-lattice Boltzmann method for simulating incompressible viscous flows, Physical Letter A, 354 (2006) pp. 173-182.

Peskin, C. S., Numerical analysis of blood flow in the heart, Journal of Computational Physics, 1977, 25, pp. 220-252.

Shan, X., Chen, H., Lattice Boltzmann model for simulating flows with multiple phases and components, Physical Review E, 1993, 47(3), pp. 1815-1820.

Sterling, J.D., Chen, S., Stability analysis of lattice Boltzmann methods, Journal of Computational Physics, 1996, 123, pp. 196-206.

ten Cate, A., Nieuwstad, C. H., Derksen, J. J., Van den Akker, H. E. A., Particle imaging velocimetry experiments and lattice-Boltzmann simulations on a single sphere setting under gravity, Physics of Fluids, 2002, 14 (11), pp. 4012-4025.

Tsutahara, M., Kurita, M., Iwagami, T., A study of new finite difference lattice Boltzmann model, Transaction of Japanese Society of Mechanical Engineers, Series B, 2002, 68(665), pp. 17-21. (in Japanese)

Tsutahara, M., Kataoka, T., Shikata, K., Takada, N., New model and scheme for compressible fluids of the finite difference lattice Boltzmann method and direct simulations of aerodynamic sound, Computers & Fluids, 2008, 37, pp. 79-89.

Wan, D., Turek, S., Direct numerical simulation of particulate flow via multigrid FEM techniques and the fictitious boundary method, International Journal for Numerical Methods in Fluids, 2006, 51, pp. 531-566.

Watari, M., Tsutahara, M., Boundary conditions for finite difference lattice Boltzmann method, Transaction of Japanese Society of Mechanical Engineers, Series B, 2002, 68(676), pp. 3229-3236. (in Japanese)

Wu, J., Shu, C., Implicit velocity correction-based immersed boundary-lattice Boltzmann method and its applications, Journal of Computational Physics, 2009, 228, pp. 1963-1979.

Yang, X., Zhang, X., Li, Z., He, G.W., A smoothing technique for discrete delta functions with application to immersed boundary method in moving boundary simulations, Journal of Computational Physics, 2009, 228, pp. 7821-7836.

Yu, Z., Fan, L.-S., Numerical simulation of bubble interactions using an adaptive lattice Boltzmann method, Chemical Engineering Science, 2011, 66, pp. 3441-3451.

3

Simulations of high Reynolds number particles

3.1 Introduction

IB-LBM has been proven to be a promising method to predict liquid-solid two-phases flows [Feng & Michaelides, 2004; 2005; 2009; Dupuis et al., 2008; Wu & Shu, 2009; Kang & Hassan, 2010; Lin et al., 2010]. However, as previously mentioned, IB-LBM has some restrictions: (1) high computational cost, i.e. high spatial resolution is required to stably simulate flows at high Reynolds numbers [Cao et al., 1997; Sterling & Chen, 1996], and (2) the lattice spacing and the time step cannot be independently altered since the lattice Boltzmann equation (LBE) requires a discrete particle to move from a lattice point to its neighbor during one time step. Although several extensions of LBM have been made to overcome the numerical instability [Lallemand & Luo, 2000; Karlin et al., 1998; Shu et al., 2006], these methods still have the former restriction.

In the previous chapter, a combination of the immersed boundary method [Dupuis et al. 2008] and the finite difference lattice Boltzmann method (IB-FDLBM) [Tsutahara et al., 2002] was proposed for predicting liquid-solid two-phase flows including moving particles. Predictions of single particles falling in liquid and interactions of two falling particles at moderate Reynolds numbers agree well with other numerical predictions and experimental data. However the applicability of IB-FDLBM to particulate flows at high Reynolds numbers has not been examined.

In this chapter, numerical simulations of high Reynolds number flows are, therefore, carried out using IB-FDLBM. Flows past a stationary circular cylinder are simulated for a wide range of Reynolds number, Re, i.e. $1 \leq Re \leq 1\times10^5$. Predicted drag coefficients and Strouhal numbers are compared with available experimental and numerical data. Flows past a square cylinder are also simulated. Simulations of flows past a stationary sphere are carried out and the predicted drag coefficients are compared with measured data. Then, free-falling cylinders at intermediate and high Reynolds numbers are simulated to examine the applicability of the method to moving particles at these Reynolds numbers.

3.2 Flows past a stationary circular cylinder

Flows past a stationary circular cylinder are used for examining the applicability of IB-FDLBM to high Reynolds numbers since many experimental and numerical results are available for comparison. Calculations are carried out for a wide range of Re, i.e. $1 \leq Re \leq 1\times10^5$. The computational domain and numerical condition are the same as the ones shown in Fig. 1.2. The dimensions of the domain are W = 50D and H = 40D in the x and y directions. The cylinder is located at (x, y) = (20D, 20D) and $D/\Delta x$ = 40. The number of Lagrangian points is 126. The value of A is 0.5. The time step is 0.5.

The drag and lift forces, F_D, and F_L, respectively, are calculated from the external force by

$$F_D = -\sum_{L=1}^{N_m} F_x(\boldsymbol{X}_L, t)\Delta S\,\Delta x \tag{3.1}$$

$$F_L = -\sum_{L=1}^{N_m} F_y(\boldsymbol{X}_L, t)\Delta S\, \Delta x \tag{3.2}$$

where $\boldsymbol{F}(\boldsymbol{X}_L, t) = (F_x(\boldsymbol{X}_L, t), F_y(\boldsymbol{X}_L, t))$. The drag and lift coefficients, C_D and C_L, are defined by

$$C_D = \frac{F_D}{\frac{1}{2}\rho U_0^2 D} \tag{3.3}$$

$$C_L = \frac{F_L}{\frac{1}{2}\rho U_0^2 D} \tag{3.4}$$

The Strouhal number is defined by

$$St = \frac{f_q D}{U_0} \tag{3.5}$$

where f_q is the frequency of vortex shedding, which is calculated from the temporal change in C_L.

Figure 3.1 shows the drag coefficient predicted by using IB-FDLBM. Good agreements with the measured data [Wieselsberger, 1922] are obtained up to approximately Re =160~200 [Mansy et al., 1994]. Table 3.1 shows that C_D obtained with the proposed IB-FDLBM agree well with those obtained using other numerical methods. Similar to the result of IB-LBM detailed in Section 1.3.3.2, the predicted drag coefficients slightly differ from the experimental data at Re = 500 and 1000. However the predicted drag coefficient at Re = 1000 agree well with the numerical predictions [Lei et al., 2000; Matsumiya et al.,

Table 3.1 Comparison of drag coefficient of steady and unsteady flows past a circular cylinder

	Re = 20		Re = 40		Re = 100
	C_D	L	C_D	L	C_D
IB-LBM [Kang&Hassan, 2010]	2.090	1.902	1.572	4.796	1.399
IB-LBM[Wu&Shu, 2009]	2.091	1.860	1.565	4.620	1.364
FDM* [Park et al. 1998]	2.010	1.900	1.510	4.760	1.330
IB-FDLBM (Present)	2.135	1.950	1.580	4.850	1.405

*FDM: finite difference method

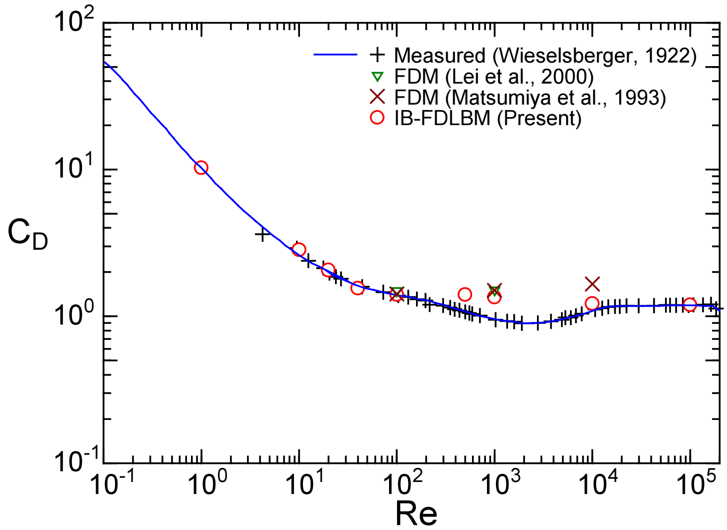

Fig. 3.1 Drag coefficient of a stationary cylinder obtained by using IB-FDLBM

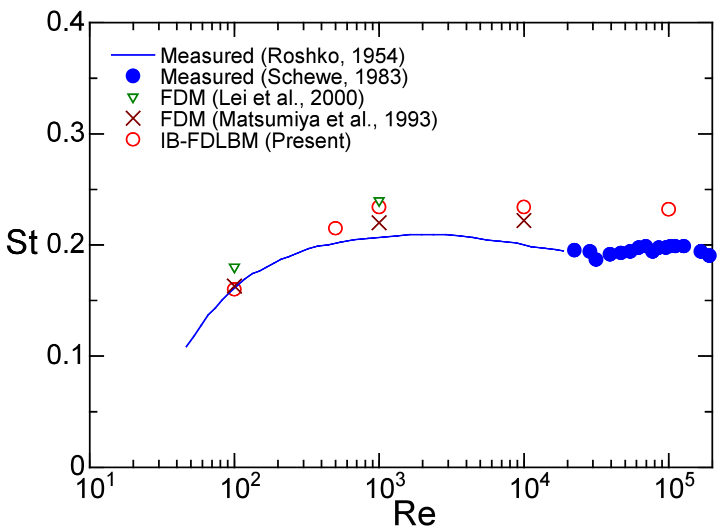

Fig. 3.2 Strouhal number of a stationary cylinder obtained by using IB-FDLBM

1993; Mittal & Kumar, 2001; Kondo, 1993]. The flows at the higher Reynolds numbers, $Re = 1\times10^4$ and 1×10^5, are successfully simulated without any numerical instability and the predicted drag coefficients agree well with the measured data. The predicted Strouhal number is larger than the measured data as shown in Fig. 3.2. Three-dimensional simulations should be done for obtaining better prediction of *St,* and for predicting the three-dimensional disturbances appearing in the near wake region in a turbulent flow.

The streamlines of steady flows about the cylinder at $Re = 20$ and 40 are shown in Figs 3.3 (a) and (b). A pair of stationary symmetric vortices is formed behind the cylinder in each case. These flow patterns are in good agreement with experimental observations [Bachelor, 2000]. The length L of the vortex increases with Re. The L in steady flows (scaled by $D/2$) shown in Table 3.1 reasonably agrees with the other numerical results. In Figs. 3.3 (a) and (b), some streamlines penetrate into the cylinder surface. As pointed out by Wu & Shu [2009], it is difficult for the direct-forcing method implemented in Chapter 2 to perfectly satisfy the no-slip boundary condition, and the non-physical penetration is apt to take place. However, as shown in Figs. 3.3 (c) and (d), the error in velocity at the cylinder surface is very small and good predictions of the vortex shape and drag coefficient are obtained. Figures 3.4 (a)-(d) shows the streamlines and the vortex shedding of the flow at $Re = 100$ at two instants. The flow is unsteady and periodic vortex shedding (Kármán vortex street) takes place behind the cylinder (Figs. 3.4(c) and (d)). The streamlines of flows at $Re = 1\times10^5$ show irregular vortex shedding. In reality, flows at this Reynolds number possess more vortical structures with three-dimensional fluctuations [Van Dyke, 1982], which are, of course, not obtained with the present two-dimensional simulation.

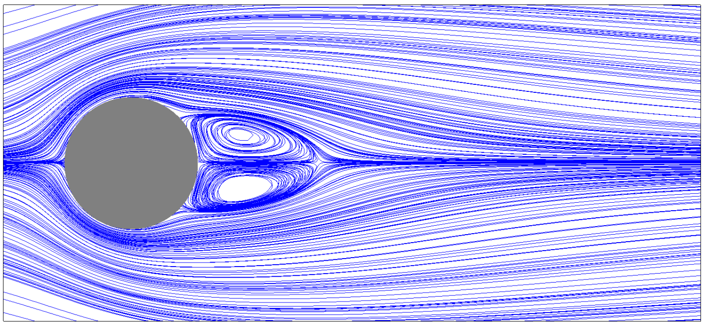

(a) Re = 20

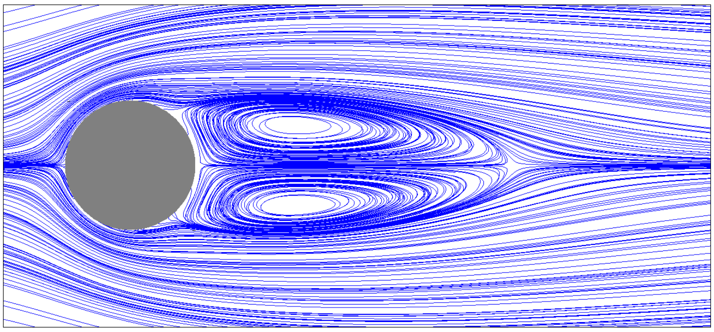

(b) Re = 40

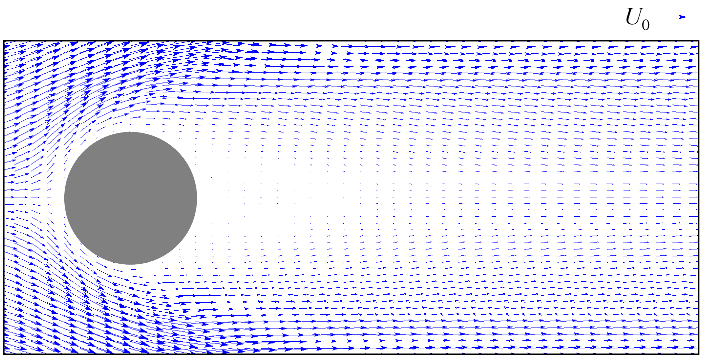

(c) Re = 20

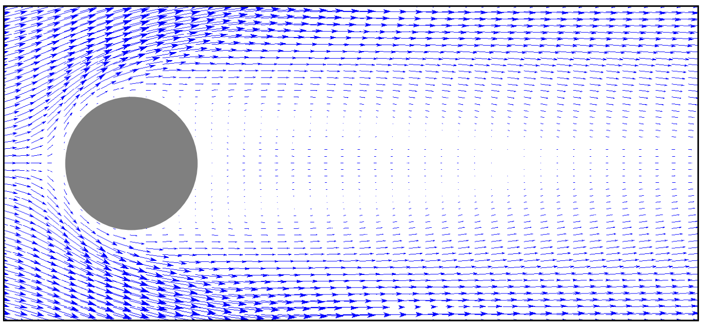

(d) Re = 40

Fig. 3.3 Streamlines and velocity field of steady flows about a circular cylinder

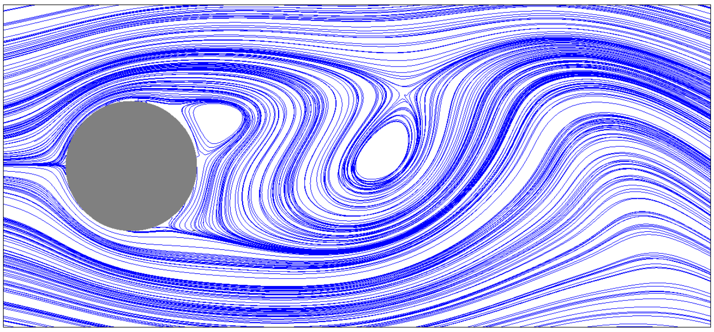

(a) Dimensionless time $U_0 t/D$ = 218.75

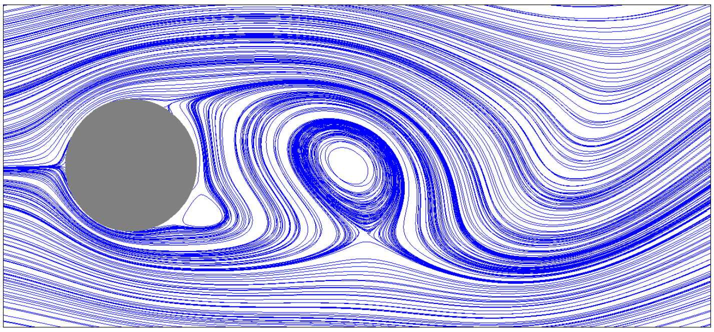

(b) $U_0 t/D$ = 221.25

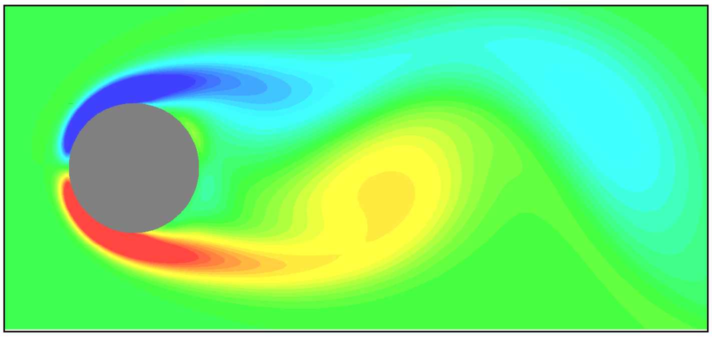

(c) $U_0 t/D$ = 218.75

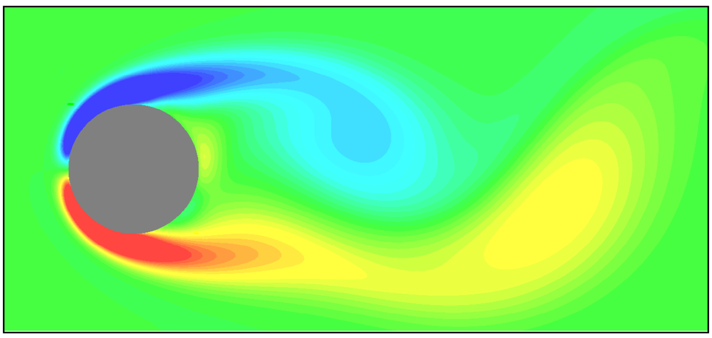

(d) $U_0 t/D$ = 221.25

Fig. 3.4 Streamlines and vortex shedding about a circular cylinder at Re = 100

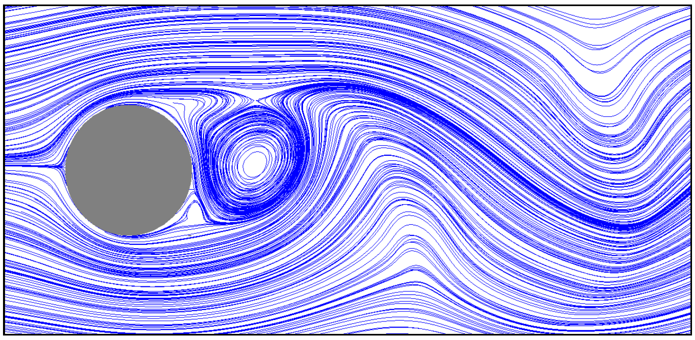

(a) Dimensionless time $U_0 t/D$ = 218.75

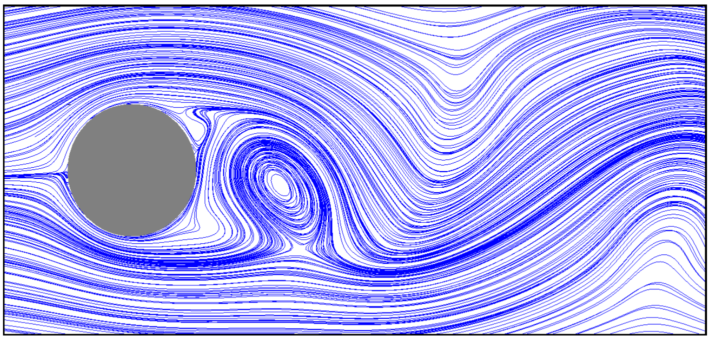

(b) $U_0 t/D$ = 221.25

Fig. 3.5 Streamlines about a circular cylinder at Re = 1×10^5

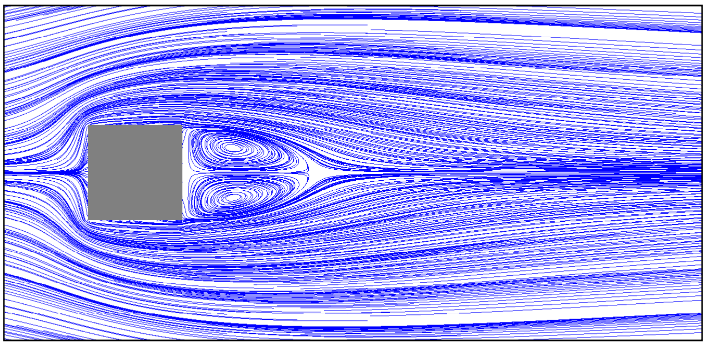

Fig. 3.6 Streamlines about a square cylinder at Re = 20 and θ = 0°

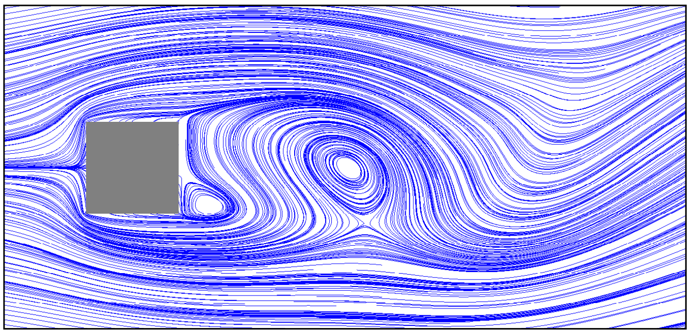

(a) Dimensionless time $U_0 t/D$ = 181.25

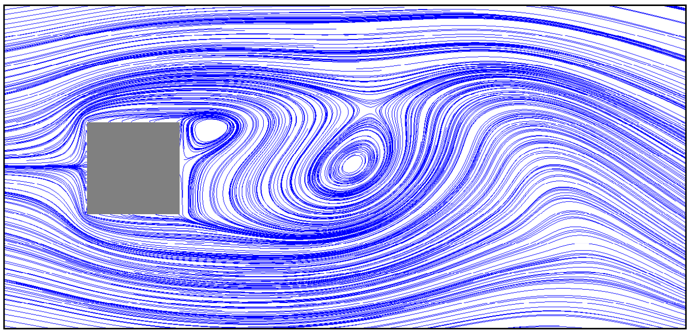

(b) $U_0 t/D$ = 185

Fig. 3.7 Streamlines about a square cylinder at *Re* = 100 and θ = 0°

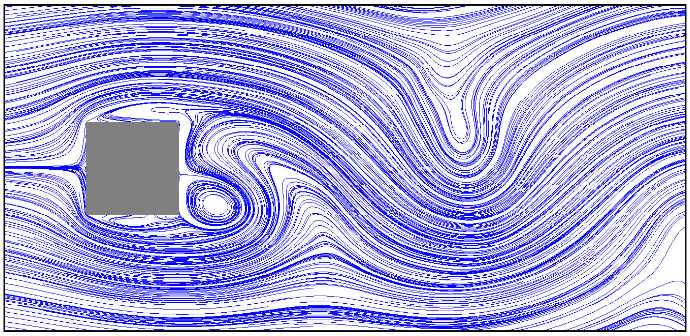

(a) Dimensionless time $U_0 t/D$ = 185

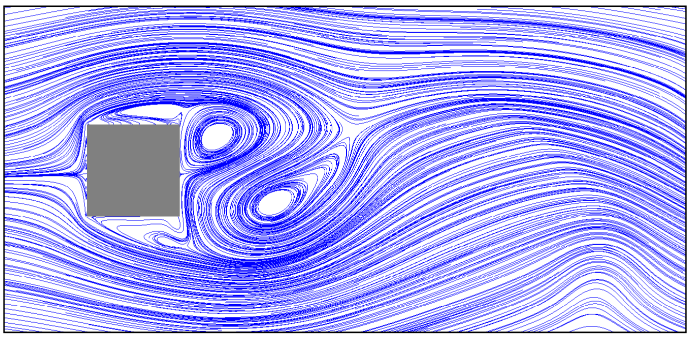

(b) $U_0 t/D$ = 188.75

Fig. 3.8 Streamlines about a square cylinder at *Re* = 100000 and θ = 0°

3.3 Flows past a stationary square cylinder

Flows past a square cylinder are simulated to prove that the proposed method can predict flows about an obstacle with sharp-edged boundaries. The computational setup is the same as that used in the simulations of flows past a circular cylinder. The dimension of the square is $40\Delta x$. The number of Lagrangian points is 160. The Reynolds number tested are $Re = 20$, 100 and 100000.

The streamlines of the flows at $Re = 20$, 100 and 100000 and $\theta = 0°$ are shown in Figs. 3.6-3.8, where θ is the angle of incidence. A pair of stationary vortices is formed behind the square cylinder at $Re = 20$. The periodic vortex shedding is observed at $Re = 100$. The frequency of the vortex shedding becomes irregular as Re increases. At $\theta = 45°$, a pair of stationary vortices appears behind the inclined square cylinder (Fig. 3.9). Irregular vortex shedding at $Re = 100$ and 100000 and $\theta = 45°$ is shown in Figs. 3.10 and 3.11. These flow patterns are in good agreement with those obtained by Yoon et al. [2010].

The predicted drag coefficients are compared with other numerical results [Yoon, D.H. et al., 2010] in Table 3.2. Reasonable agreements are obtained for steady and unsteady flows at $Re = 20$ and 100 at $\theta = 0°$ and 45°. For steady flows, the reduction of the drag coefficient with increasing θ is reasonably predicted. The drag coefficient of unsteady flows increases with increasing θ for $Re \geq 100$. The drag coefficients of flows at $Re = 100000$ are similar to those obtained by Lyn et al. [Lyn, D. A. et al., 1995] for flows in the subcritical region, i.e. $C_D = 2.16$. Furthermore instability is not present in the calculations in spite of the high Reynolds numbers.

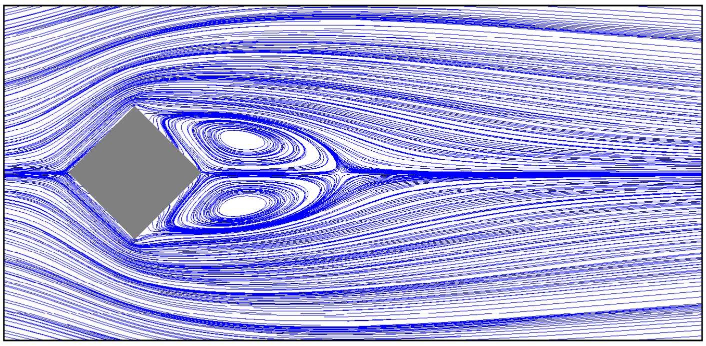

Fig. 3.9 Streamlines about a square cylinder at $Re = 20$ and $\theta = 45°$

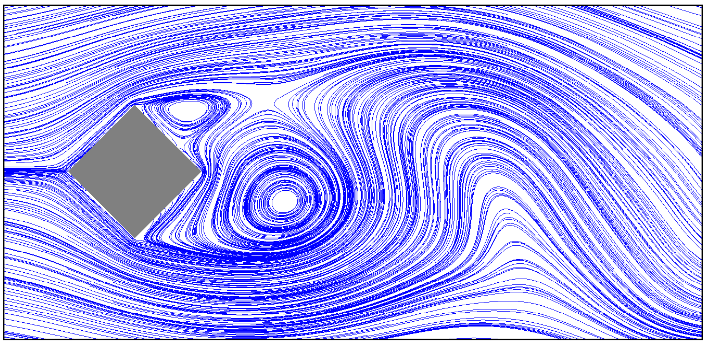

(a) Dimensionless time $U_0 t/D = 182.5$

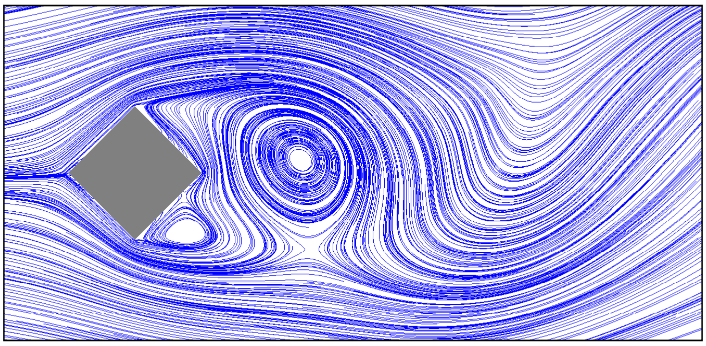

(b) $U_0 t/D = 186.25$

Fig. 3.10 Streamlines about a square cylinder at $Re = 100$ and $\theta = 45°$

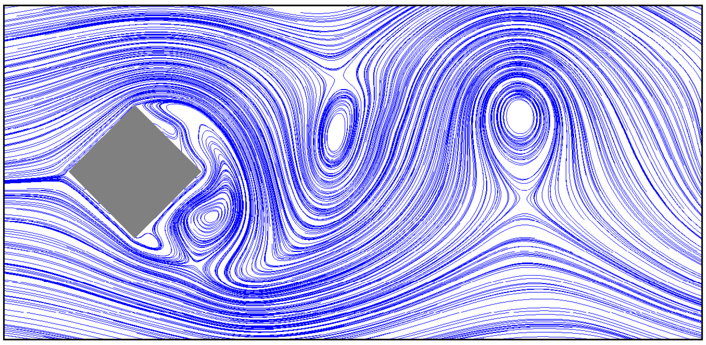

(a) Dimensionless time $U_0 t/D$ = 182.5

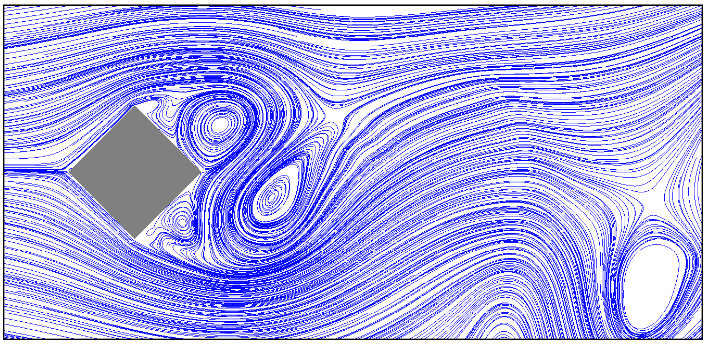

(b) $U_0 t/D$ = 186.25

Fig. 3.11 Streamlines about a square cylinder at Re = 100000 and θ = 45°

Table 3.2 Comparison of drag coefficient of flows past a square cylinder

θ	0°			45°		
Re	20	100	100000	20	100	100000
FVM [Yoon, D.H. et al., 2010]	2.21	1.46	-	1.98	1.8	-
IB-FDLBM (Present)	2.25	1.543	2.26	2.03	1.82	2.35

*FVM: finite volume method

3.4 Flows past a stationary sphere

Simulations of flows past a sphere at intermediate and high Reynolds numbers are carried out. The domain sizes are 50D, 40D and 40D in the x, y and z directions, respectively. The sphere is located at (x, y, z) = (20D, 20D, 20D). The left boundary condition is uniform inflow at free stream velocity, U_0, 0.05. The other boundaries are continuous outflow. A wide range of Reynolds numbers, i.e. from Re = 1 to 10000, is tested. Lagrangian points are generated using a method proposed by Feng & Michaelides [2005]. Effects of the grid resolution are also evaluated. The number of Lagrangian points at the sphere surface is 346, 1338 and 4958 for flows at $D/\Delta x$ = 10, 20 and 40, respectively. The negative viscosity term, A, is set at 0.5.

The drag coefficients are plotted against the Reynolds number in Fig. 3.12. At low Reynolds numbers, good agreements between the measured data [Wieselsberger, 1922] and the predictions are obtained using IB-FDLBM with fine and coarse grid resolutions. However, when the Reynolds number increases, the predictions with $D/\Delta x$ = 10 and 20 differ from the measured data. In contrast, the predictions obtained using IB-FDLBM at $D/\Delta x$ = 40 reasonably agree with the measurements. Irregular vortex shedding of flow at Re = 10000 is shown in Figs. 3.13 (a) and (b).

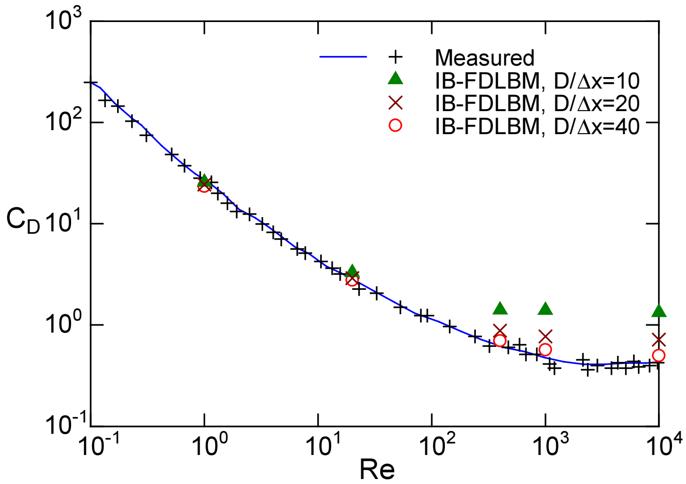

Fig. 3.12 Drag coefficients of flows past a sphere

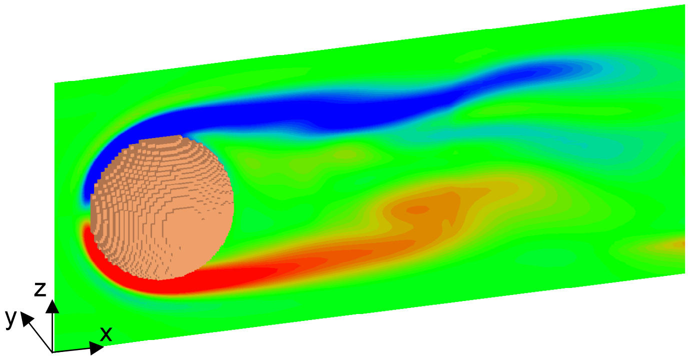

(a) $U_0 t/D = 287.50$

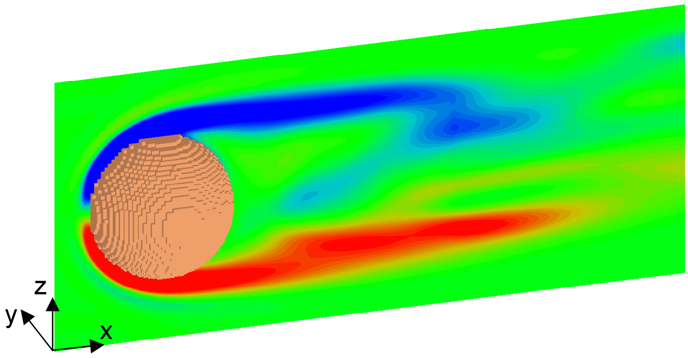

(b) $U_0 t/D = 306.25$

Fig. 3.13 Vorticity field of flows past a sphere

3.5 Free-falling cylinders for *Re* ≤ 20000

The motion of a free-falling circular cylinder is simulated to examine the applicability of IB-FDLBM to moving boundary problems at high Reynolds numbers. It is known that the Strouhal number of a free-falling cylinder is lower than that of a stationary cylinder at the same Reynolds number [Namkoong et al., 2008], that is, the vortex shedding is retarded due to the cylinder motion. Namkoong et al. [2008] carried out simulations of free-falling cylinders at intermediate Reynolds numbers (Re < 188) using a finite element method and the mechanism of the St reduction has been described as follows: the cylinder tends to move toward the low-pressure side, where a vortex is generated and then separates, so that the pressure on this side recovers with the retardation of vortex separation. Simulations of free-falling cylinders at intermediate Re are first carried out using IB-FDLBM to examine whether or not IB-FDLBM can reproduce the St reduction. The numerical setup is similar to that shown in Fig. 1.2 whereas the domain size is the same as that used in Namkoong et al., i.e., $W = 70D$ and $H = 100D$ in the x and y directions. The initial cylinder position is $(x,y) = (20D, 50D)$. The computational grid is uniform near the cylinder, whereas it is non-uniform in the other region. The dimensions of the uniform grid region are $5D$ and $2D$ in the x and y directions, and the spatial resolution of this region is $D = 40\Delta x$ ($\Delta x = \Delta y = 1$). The number of Lagrangian points is 126. Uniform flow in the x direction enters from the left boundary and crosses the cylinder. First the cylinder is fixed at the initial position until the flow reaches a quasi-steady state. Then, the constraint on cylinder motion is removed and the translation and rotation of the cylinder are calculated by solving the equations of motion, Eqs. (2.16) and (2.17). The acceleration of gravity directing toward $-x$ is added and its value is set so as to balance the gravitational force with the drag force. Hence the motion of the free-falling cylinder is observed in the frame of reference moving with the cylinder velocity. The Reynolds numbers simulated are 96, 119, 138 and 156.

Figure 3.14 shows a comparison of the Strouhal numbers of stationary and free-falling cylinders. The predicted Strouhal numbers of the stationary cylinder agree very well with those measured by Roshko [1954]. The Strouhal number of the free-falling cylinder takes lower values than that of the stationary cylinder and agrees well with the predictions by Namkoong et al.

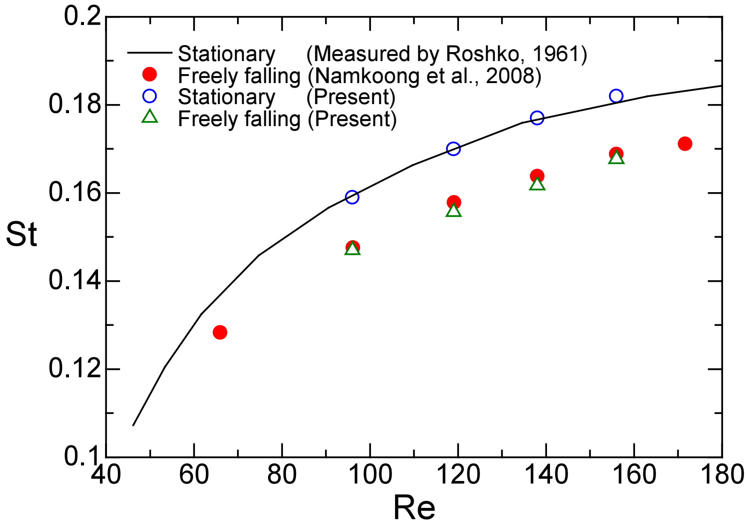

Fig. 3.14 Strouhal numbers of stationary and free-falling cylinders

Then, a circular cylinder falling at a high Reynolds number is simulated. The numerical conditions are similar to those in section 3.2: the domain size is $W = 50D$ and $H = 40D$ in the x and y directions, the initial cylinder position is $(x, y) = (20D, 20D)$, $D/\Delta x = 40$ and the number of Lagrangian points is 126. The Reynolds number is 2×10^4. The cylinder oscillates due to the vortex shedding. The amplitude of the oscillation is not constant because the flow fluctuation at this Re is irregular. The averaged drag coefficient is approximately 1.2, which is the same as that of the stationary cylinder. The predicted Strouhal number of the stationary cylinder is 0.234 while $St \approx 0.191$ for the free-falling cylinder.

The processes of vortex shedding for the stationary cylinder and for the free-falling cylinder are shown in Figs. 3.15 (a) and (b), respectively. The cross symbol represents the initial position of cylinder center. The time interval, ΔT, scaled with U_0 and D is 1.25. In the

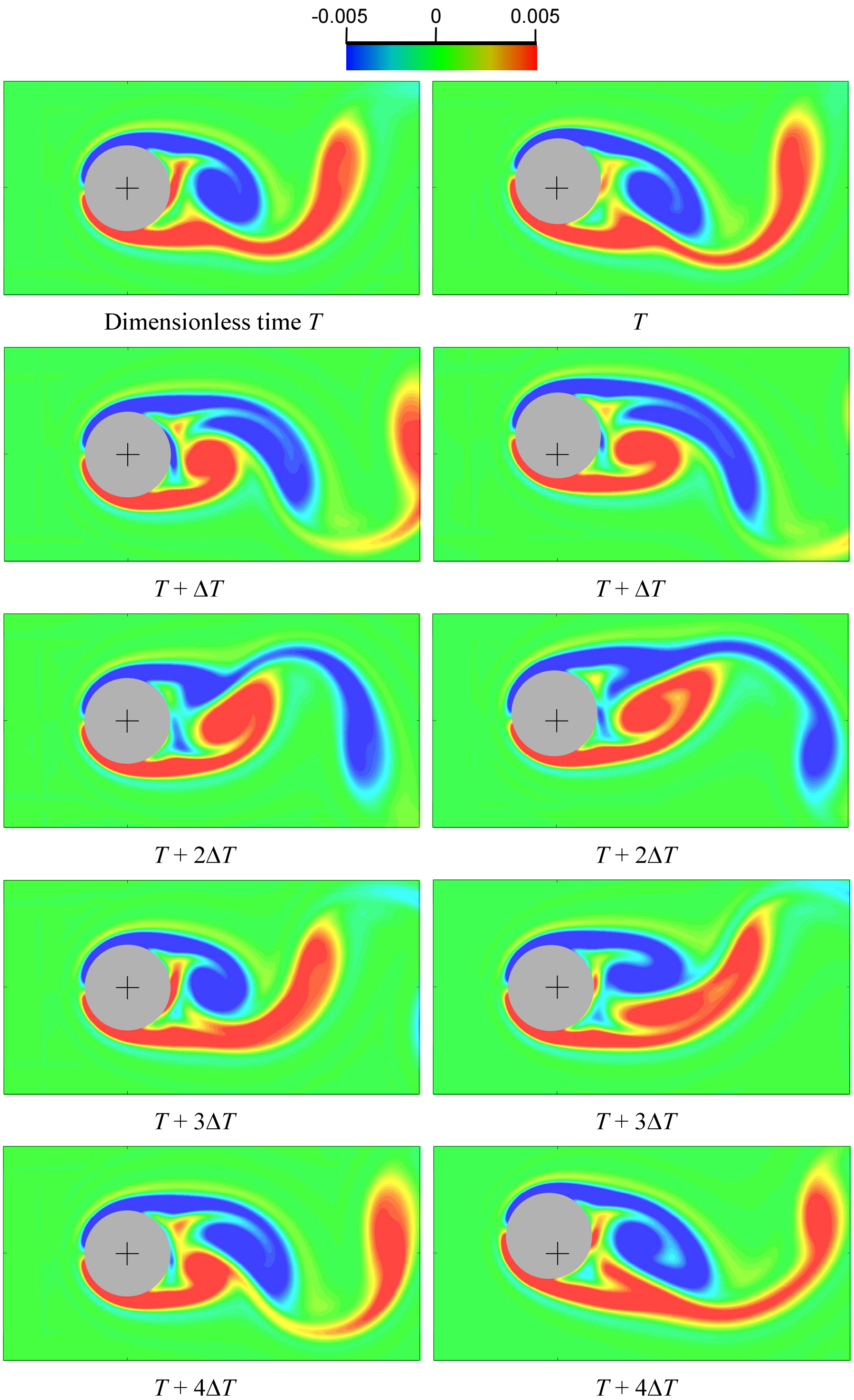

(a) Stationary cylinder (b) Free-falling cylinder

Fig. 3.15 Dimensionless vorticity fields about a stationary and free-falling cylinders at Re=2×10^4

case of the stationary cylinder, the negative vortex (clockwise vortex represented with blue color) behind the cylinder is elongated in the streamwise direction at the dimensionless time T and is shed downstream when the positive vortex (counter-clockwise vortex represented with red color) is formed ($T + \Delta T$). The positive vortex is elongated ($T + 2\Delta T$) and is shed when the new negative vortex is formed ($T + 3\Delta T$). Then the next shedding cycle starts ($T + 4\Delta T$). Thus the period of vortex shedding is about $3\Delta T$. The vortex-shedding process for the free-falling cylinder is similar to that of the stationary cylinder, whereas the cylinder motion affects the vortex motion, i.e., each vortex is more elongated compared with that of the stationary cylinder. The period of vortex-shedding process is also changed to about $4\Delta T$.

3.6 Conclusions

Simulations of two-dimensional flows about a circular cylinder and flows past a sphere for a wide range of Reynolds numbers were carried out using the immersed boundary-finite difference lattice Boltzmann method (IB-FDLBM) to investigate its applicability to high Reynolds number liquid-solid two-phase flows. The drag coefficients and Strouhal numbers obtained were compared with experimental data and available numerical predictions. Simulations of free-falling cylinders at intermediate and high Reynolds numbers were also performed. As a result, the following conclusions were obtained:

(1) Steady and unsteady flows at $1 \leq Re \leq 1\times10^5$ about circular and square cylinders are well predicted with IB-FDLBM.

(2) IB-FDLBM can stably simulate flows at very high Reynolds numbers without increasing the spatial resolution.

(3) IB-FDLBM gives reasonable predictions of the drag coefficients of a sphere in uniform flows for a wide range of Reynolds number, i.e. $1 \le Re \le 1\times10^4$ provided that the ratio, $D/\Delta x$, is high enough.

(4) IB-FDLBM gives accurate predictions for the motion of free-falling cylinders at intermediate Reynolds numbers.

(5) IB-FDLBM reasonably predicts moving boundary problems at high Reynolds numbers.

References

Bachelor, G. K., An introduction to fluid dynamics, Cambridge University Press, 2000.

Cao, N., Chen, S., Jin, S., Martinez, D., Physical symmetry and lattice symmetry in the lattice Boltzmann method, Physical Review E, 1997, 55(1), pp. 21-24.

Dupuis, A., Chatelain, P., Koumoutsakos, P., An immersed boundary–lattice-Boltzmann method for the simulation of the flow past an impulsively started cylinder, Journal of Computational Physics, 2008, 227, pp. 4486-4498.

Feng, Z.-G., Michaelides, E. E., The immersed boundary-lattice Boltzmann method for solving fluid-particles interaction problems, Journal of Computational Physics, 2004, 195, pp. 602-628.

Feng, Z.-G., Michaelides, E. E., Proteus: a direct forcing method in the simulations of particulate flows, Journal of Computational Physics, 2005, 202, pp. 20-51.

Feng, Z.-G., Michaelides, E. E., Robust treatment of no-slip boundary condition and velocity updating for the lattice-Boltzmann simulation of particulate flows, Computers and Fluids, 2009, 38, pp. 370-381.

Kang, S. K., Hassan, Y. A., A comparative study of direct-forcing immersed boundary-lattice Boltzmann methods for stationary complex boundaries, International Journal for Numerical Methods in Fluids, 2010, DOI: 10.1002/fld.2304.

Karlin, I.V., Gorban, A.N., Succi, S., Boffi, V., Maximum entropy principle for lattice kinetic equations, Physical Review Letters, 1998, 81, pp. 6-9.

Kondo, N., Direct third-order upwind finite element simulation of high Reynolds number flows around a circular cylinder, Journal of Wind Engineering and Industrial Aerodynamics, 1993, 46&47, pp. 349-356.

Lallemand, P., Luo, L.S., Theory of the lattice Boltzmann method: dispersion, dissipation, isotropy, Galilean invariance, and stability, Physical Review E, 2000, 61, pp. 6546-6562.

Lei, C., Cheng, L., Kavanagh K., A finite difference solution of the shear flow over a circular cylinder, Ocean Engineering, 2000, 27, pp. 271-290.

Lin, S.-Y., Lin, C.-T., Chin, Y.-H., Tai, Y.-H., A direct-forcing pressure-based lattice Boltzmann method for solving fluid-particle interaction problems, International Journal for Numerical Methods in Fluids, 2010, DOI: 10.1002/fld.2442.

Lyn, D., A., Einav, S., Rodi, W., Park, J. H. “A laser-Doppler velocimetry study of ensemble-averaged characteristics of the turbulent near wake of a square cylinder”, Journal of Fluid Mechanics, 1995, 304, pp. 285-319.

Mansy, H., Yang, P.M., Williams, D.R., Quantitative measurements of three-dimensional structures in the wake of a circular cylinder, Journal of Fluid Mechanics, 1994, 270, pp. 277-296.

Matsumiya, H., Kieda, K., Taniguchi, N., Kobayashi, T., Numerical simulation of 2D flow around a circular cylinder by the third-order upwind finite difference method, Transaction of Japanese Society of Mechanical Engineers, Series B, 1993, 59(566), pp. 2937-2943. (in Japanese)

Mittal, S., Kumar, V., Flow-induced vibrations of a light circular cylinder at Reynolds number 10^3 to 10^4, Journal of Sound and Vibration, 2001, 245(5), pp. 923-946.

Namkoong, K., Yoo, J. Y., Choi, H., Numerical Analysis of Two-Dimensional Motion of a Freely Falling Circular Cylinder in an Infinite Fluid, Journal of Fluid Mechanics, 2008, 604, pp. 33-53.

Park, J., Kwon, K., Choi, H., Numerical solutions of flow past a circular cylinder at Reynolds numbers up to 160, KSME International Journal, 1998, 12(6), pp. 1200-1205.

Roshko, A., On the development of turbulent wakes from vortex streets, NACA, 1954, Rep. 1191.

Schewe, G., On the force fluctuations acting on a circular cylinder in cross flow from subcritical up to transcritical Reynolds numbers, Journal of Fluid Mechanics, 1983, 133, pp. 265-285.

Shu, C., Niu, X.D., Chew, Y.T., Cai, Q.D., A fractional step lattice Boltzmann method for simulating high Reynolds number flows, Mathematics and Computers in Simulation, 2006, 72, pp. 201-205.

Sterling, J.D., Chen, S., Stability analysis of lattice Boltzmann methods, Journal of Computational Physics, 1996, 123, pp. 196-206.

Tsutahara, M., Kurita, M., Iwagami, T., A study of new finite difference lattice Boltzmann model, Transaction of Japanese Society of Mechanical Engineers, Series B, 2002, 68(665), pp. 17-21. (in Japanese)

Van Dyke, M., An album of fluid motion, Parabolic Press, 1982.

Wieselsberger, C., New data on the laws of fluid resistance, National Advisory Committee for Aeronautics, 1922, 84.

Wu, J., Shu, C., Implicit velocity correction-based immersed boundary-lattice Boltzmann method and its applications, Journal of Computational Physics, 2009, 228, pp. 1963-1979.

Yoon, D., P., Yang, K., S., Choi, C., B., "Flow past a square cylinder with an angle of incidence", Physical of Fluids, 2010, 22, 043603.

4

Prevention of the unphysical distortion in velocity field at low Reynolds number flows

4.1 Introduction

Due to its simplicity and numerical efficiency, LBMs often utilize the single-relaxation time (SRT) [Bhatnagar, 1954] model for the particle collision term in the lattice Boltzmann equation. Particulate flows with moving and stationary boundaries at intermediate Reynolds numbers have been reasonably predicted using IB-LBM and SRT [Feng & Michaelides, 2009; Dupuis et al., 2008; Kang & Hassan, 2010]. Since the single relaxation time, τ, is a monotonically increasing function of the kinematic viscosity ν, τ decreases with decreasing ν, i.e. with increasing the Reynolds number, which is defined by $Re = UL/\nu$ where U is the characteristic velocity and L the characteristic length. Simulations become unstable as τ approaches its lower limit, $\tau = 1/2$ [Chen & Doolen, 1998], and a high spatial resolution is required to perform stable calculations of high Reynolds number flows [Sterling & Chen, 1996; Cao et al., 1997]. In addition, Le & Zhang [2009] reported that the validity of IB-LBM strongly depends on τ. They carried out calculations of simple flows, e.g. planar and circular Couette flows, by using IB-LBM proposed by Dupuis et al. [2008], and pointed out that large distortion of the velocity field or velocity slip appears in the vicinity of immersed boundaries when the Reynolds number is low, i.e. when the relaxation time is high.

In Chapters 2 and 3, IB-FDLBM using SRT was proposed to predict liquid-solid two-phases flows at moderate and high Reynolds numbers. However the method has not been validated at low Reynolds numbers, and therefore, calculations of circular Couette flows are carried out using IB-FDLBM. The numerical conditions are similar to those in section 1.3.3.3 [Le & Zhang, 2009], and the negative viscosity term, A, is 0.5. The range of Re tested is from 0.038 to 1.5. In this case the relaxation time, τ, varies from 1 to 20. Figures 4.1 (a)-(d) show the azimuthal velocity distribution, u_θ/U_θ, in the steady state predicted by using IB-FDLBM with SRT. The velocity distortion near the immersed boundary appears as in IB-LBM when Re = 0.038 and 0.079, i.e. when τ = 20 and 10.

Niu et al. [2006] implemented a multi-relaxation time (MRT) model instead of SRT into IB-LBM for better accuracy and stability. However, the numerical algorithm of MRT is more complicated than that of SRT. In addition, the number of relaxation times is large. For example, six relaxation times to define the viscosity and 13 relaxation times to improve numerical stability in D3Q19 [Yu et al., 2011]. In contrast, Ginzburg et al. [2005; 2008; 2008] proposed a simplification of MRT by using one relaxation time for the even order particle velocity moments of the distribution function and the other relaxation time for the odd order moments. This collision model is referred to as the two-relaxation time (TRT) collision model. In TRT, one relaxation time is used for determining the viscosity and the other for improving numerical stability and accuracy, and the latter is determined by the parameter, Λ, which is a function of the two relaxation times [d'Humieres & Ginzburg, 2009].

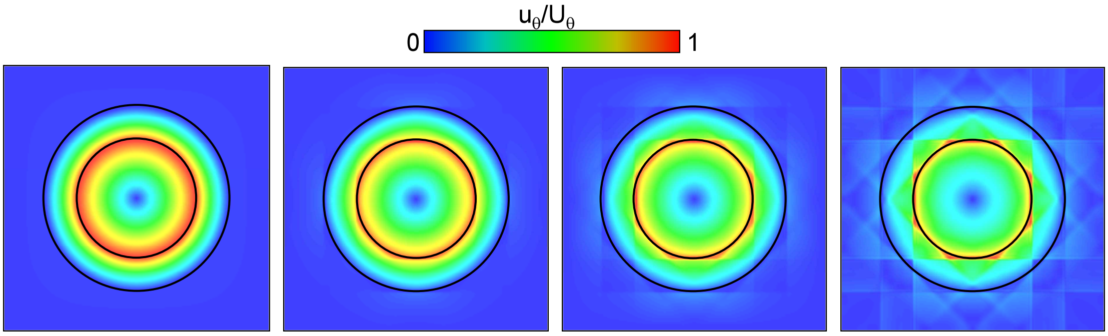

(a) (Re, τ) = (1.5, 1) (b) (0.17, 5) (c) (0.079, 10) (d) (0.038, 20)

Fig. 4.1 Velocity distributions predicted by using IB-FDLBM with SRT

The two-relaxation time collision model is, therefore, implemented into IB-LBM in this chapter for reducing or removing the velocity slip of flows at low Re. The second-order accuracy split-forcing method proposed by Chen & Li [2008] is utilized for dealing with immersed boundaries. Simulations of circular Couette flows at low and high relaxation times are carried out to validate the proposed method. Calculations of a single particle falling through liquid and DTK motion of two particles are also carried out to show that the proposed method can predict problems with moving boundaries. Finally, a theoretical analysis is conducted to derive the numerical errors in terms of the relaxation times and find the optimum values of the relaxation times.

4.2 Implementation of two-relaxation time collision model into IB-LBM

4.2.1 Numerical method

The collision operator of the two-relaxation time model [Ginzburg et al., 2005; 2008; 2008] is given by

$$\Omega_i = -\frac{1}{\tau_+}[f_i^+ - f_i^{eq,+}] - \frac{1}{\tau_-}[f_i^- - f_i^{eq,-}] \tag{4.1}$$

where τ_+ and τ_- are the relaxation times for the even order particle velocity moments of the distribution function (symmetric parts) f^+, and that for the odd order moments (antisymmetric parts) f^-, respectively. The distribution functions, f^+, f^-, $f^{eq,+}$ and $f^{eq,-}$, are defined by

$$f_i = f_i^+ + f_i^- \tag{4.2}$$

$$f_i^+ = \frac{f_i + f_{\bar{i}}}{2} \tag{4.3}$$

$$f_i^- = \frac{f_i - f_{\bar{i}}}{2} \tag{4.4}$$

$$f_i^{eq} = f_i^{eq,+} + f_i^{eq,-} \tag{4.5}$$

$$f_i^{eq,+} = \frac{f_i^{eq} + f_{\bar{i}}^{eq}}{2} \tag{4.6}$$

$$f_i^{eq,-} = \frac{f_i^{eq} - f_{\bar{i}}^{eq}}{2} \tag{4.7}$$

where the subscript $\bar{i}$ denotes the direction opposite to i, i.e. $\boldsymbol{c}_i = -\boldsymbol{c}_{\bar{i}}$. TRT reduces to SRT when $\tau_+ = \tau_-$ ($\Omega_i = -(f_i - f_i^{eq})/\tau$). Substituting Eq. (4.1) into Eq. (1.3) yields

$$f_i(\boldsymbol{x}+\boldsymbol{c}_i\Delta t,t+\Delta t)=f_i(\boldsymbol{x},t)-\frac{1}{\tau_+}[f_i^+-f_i^{eq,+}]-\frac{1}{\tau_-}[f_i^--f_i^{eq,-}] \\ +\frac{\Delta t}{2}[G_i(\boldsymbol{x}+\boldsymbol{c}_i\Delta t,t+\Delta t)+G_i(\boldsymbol{x},t)]. \tag{4.8}$$

The fluid density, ρ, velocity, $\boldsymbol{u}$, and the equilibrium distribution function, f_i^{eq}, of D2Q9 model, are defined by Eqs. (1.4) - (1.6), respectively. The kinematic viscosity, ν, is given as the following monotonically increasing function of τ_+:

$$\nu=\frac{1}{3}\left(\tau_+-\frac{1}{2}\right) \tag{4.9}$$

The relaxation time, τ_-, is determined through the following parameter [Ginzburg, 2008]:

$$\Lambda=(\tau_+-\frac{1}{2})(\tau_--\frac{1}{2}) \tag{4.10}$$

For linear advection-diffusion problems, Λ = 1/4 is the most stable value, Λ = 1/12 and Λ = 1/6 remove the third-order advection error and the fourth-order diffusion error, respectively, and Λ = 3/16 gives the exact wall location for the bounce-back model [Ginzburg at al., 2008; Kuzmin & Derksen, 2011]

The solution algorithm of Eq. (4.8) and the treatment of immersed boundaries are similar to those for SRT in Section 1.3.3.1 (Eqs. (1.10-1.19)). The discrete direct-forcing term with second-order accuracy is

$$G_i=\rho W_i\left[3\frac{\boldsymbol{c}_i-\boldsymbol{u}}{c^2}+9\frac{(\boldsymbol{c}_i\cdot\boldsymbol{u})\boldsymbol{c}_i}{c^4}\right]\cdot\boldsymbol{G} \tag{4.11}$$

The two-point (Eq. (1.17)), δ_2, and the four-point piecewise, δ_4, delta functions are utilized to investigate the effects of these delta functions on the predictions. The latter is given by [Yang et al., 2009]

$$\delta_h(r) = \begin{cases} \frac{1}{8}\left(3 - 2|r| + \sqrt{1 + 4|r| - 4r^2}\right) & \text{for} \quad |r| \le 1 \\ \frac{1}{8}\left(5 - 2|r| - \sqrt{-7 + 12|r| - 4r^2}\right) & \text{for} \quad 1 \le |r| \le 2 \\ 0 & \text{for} \quad 2 \le |r| \end{cases} \tag{4.12}$$

4.2.2 Circular Couette flows

Simulations of two-dimensional circular Couette flows using IB-LBM with TRT are carried out to investigate whether or not the proposed method can reduce or remove the non-physical distortion in velocity field of flows at low Reynolds numbers, i.e. at high relaxation times. The numerical conditions are similar to those used in Le & Zhang [2009] (Fig. 1.5). *Re* varies from 0.038 to 1.5, i.e. τ_+ varies from 1 to 20. The parameter Λ is set at 1/4. The calculations are continued while

$$\max_{IJ \in fluid} \left| \frac{u_\theta(t) - u_\theta(t - 1000\Delta t)}{u_\theta^{exact}} \right| > 1 \times 10^{-6} \tag{4.13}$$

where u_θ and u_θ^{exact} are the predicted and the exact (Eq. (1.23)) azimuthal velocity components, respectively.

Figures 4.2 and 4.3 show the velocity distributions predicted using the proposed method, i.e. IB-LBM with TRT. Even at low Reynolds numbers (high τ_+) axisymmetric flow fields are obtained with the two- and four-point delta functions, and second-order accurate forcing

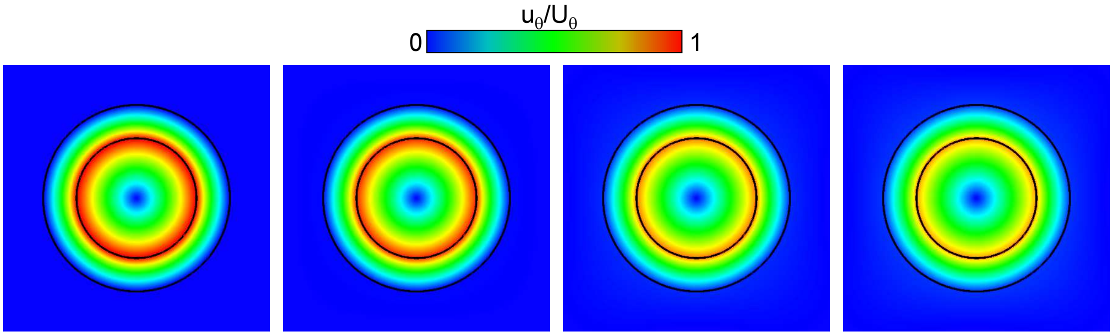

(a) (Re,τ_+,τ_-)=(1.5, 1, 1) (b) (0.17, 5, 0.56) (c) (0.079, 10, 0.53) (d) (0.038, 20, 0.51)

Fig. 4.2 Velocity distributions predicted by using IB-LBM with TRT at Λ = 1/4 and δ_2

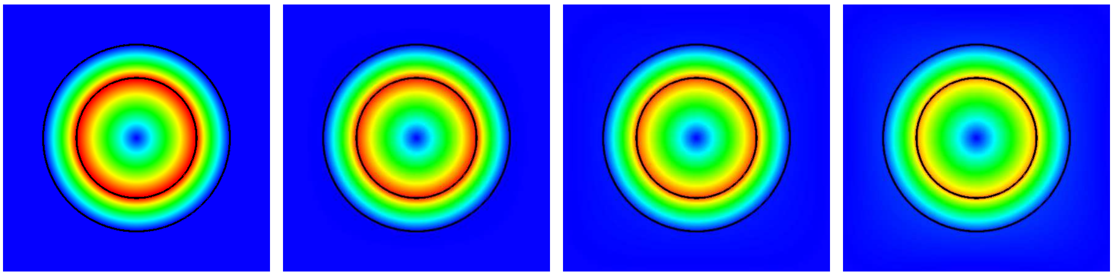
(a) (Re,τ_+,τ_-)=(1.5, 1, 1) (b) (0.17, 5, 0.56) (c) (0.079, 10, 0.53) (d) (0.038, 20, 0.51)

Fig. 4.3 Velocity distributions predicted by using IB-LBM with TRT at Λ = 1/4 and δ_4

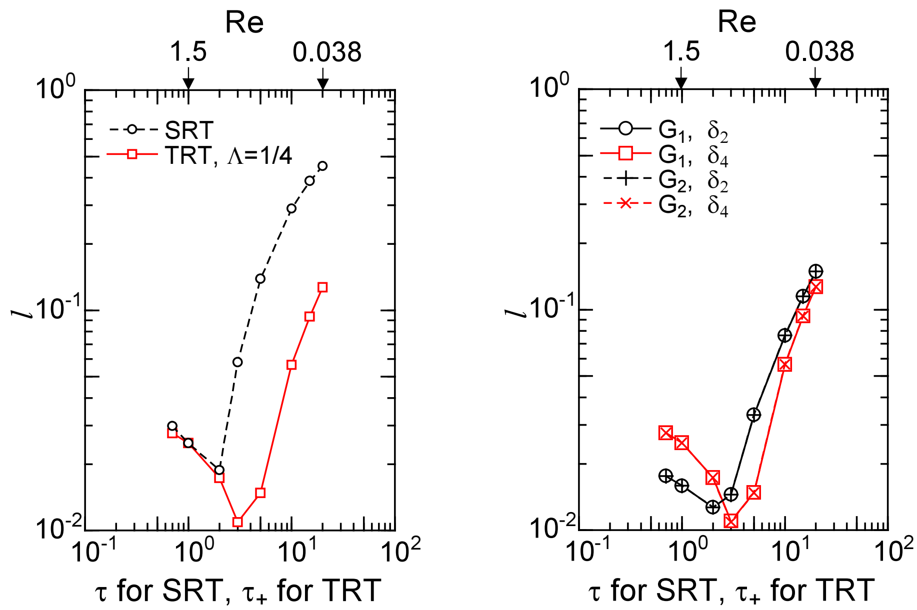

(a) (b)

Fig. 4.4 Numerical errors defined by Eq. (4.14) in circular Couette flow simulations using IB-LBM with TRT term. In order to make clear the advantage of the proposed method over IB-LBM with SRT, Figs. 4.4 (a) and (b) show the errors in the predicted velocity distributions, where l is the relative error defined by

$$l = \max_{IJ \in fluid} \left| \frac{u_\theta^{predicted} - u_\theta^{exact}}{u_\theta^{exact}} \right| \tag{4.14}$$

Figure 4.4 (a) shows a comparison of the error in velocity predicted with SRT and TRT with the second-order accurate forcing term and δ_4. In both cases, the error decreases with increasing τ_+ up to around $\tau_+ = 3$ and then increases at higher τ_+. The reason of this tendency is as follows. The direct forcing method enforces $\boldsymbol{u}_P(\boldsymbol{X}_L) = \boldsymbol{u}(\boldsymbol{X}_L)$ but does not ensure $\boldsymbol{u}_{theory}(\boldsymbol{X}_L) = \boldsymbol{u}(\boldsymbol{X}_L)$ due to the diffusive nature of δ_h. Because of this, the predicted fluid velocity in the vicinity of the rotating cylinder is slightly higher than the theoretical one at low τ_+. Then, the predicted velocity decreases as τ_+ increases and approaches the theoretical value at $\tau_+ = 2$ in SRT and $\tau_+ = 3$ in TRT, where the errors take the minimum value. Then, the errors monotonously increase with τ_+ at high τ_+ since the velocity continues to decrease with increasing τ_+. The errors in TRT are smaller than those in SRT. Figure 4.4 (b) shows the errors calculated with the first- (G_1) and second-order (G_2) accurate forcing terms. Both forcing terms give the same results. A narrow stencil delta function, i.e. δ_2, gives smaller errors at low τ_+ than those obtained with δ_4; however, the errors increase at high τ_+ (low Reynolds numbers).

4.2.3 Single particle falling through a stagnant liquid

A two-dimensional calculation of a single particle falling through a stagnant liquid is carried out to show that the proposed method can deal with moving boundaries. The numerical setup and parameters are similar to those in Section 2.3.1 (Fig. 2.5), whereas the time step size is 5×10^{-5} s and the number of Lagrangian points is 50. The parameter, Λ, in TRT is 1/4. The particle path and velocity are compared with those obtained using a finite element method [Wan & Turek, 2006] in Fig. 4.5. They are in good agreement. Furthermore, the predictions are similar to those obtained with IB-FDLBM. The effects of the accuracy of the forcing term or the type of delta function are negligible.

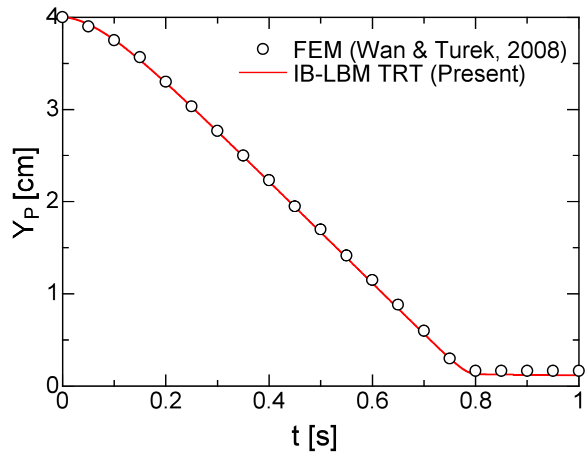

(a)

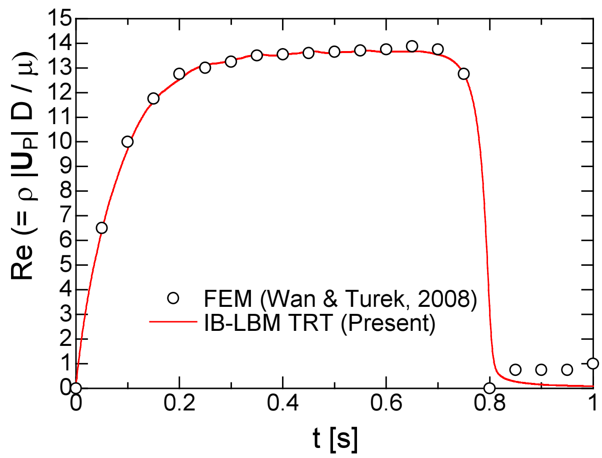

(b)

Fig. 4.5 Particle position and velocity of a single two-dimensional falling particle using IB-LBM with TRT

Single spheres falling through a liquid-filled container are also simulated. The numerical setup is the same as that utilized in Section 2.31. [ten Cate et al., 2002]. The fluid density, ρ, and viscosity, μ, are detailed in Table 2.1, whereas the time step sizes are 3.12×10^{-4}, 5.46×10^{-4}, 6.81×10^{-4} and 8.28×10^{-4} s for cases 1-4. The relaxation times, τ_{+}, are 0.86, 0.86, 0.74 and 0.65. The parameter, Λ, is 1/4. Figure 4.6 shows a comparison of the falling velocity with the experimental data. The predictions are reasonable for all the cases.

4.2.4 Drafting-kissing-tumbling motion of two particles

The particle-particle and particle-wall interactions are also predicted with the proposed method. The computational setup and parameters of two-dimensional DTK motion are given in Fig. 2.13 (Section 2.3.2). The number of Lagrangian points is 50, Δt is 5×10^{-4} s, τ_{+} is 0.65, and Λ is 1/4. The coefficients of the collision models, Eqs. (2.43) and (2.44) [Glowinski et al. 1999], are $\varepsilon_P = \varepsilon_W = 2.0$, $\zeta_P = \Delta x$, $\zeta_W = \Delta x/2$, and $c_{PP'} = c_{PW} = (\rho_P - \rho)\pi R_P^2 g$.

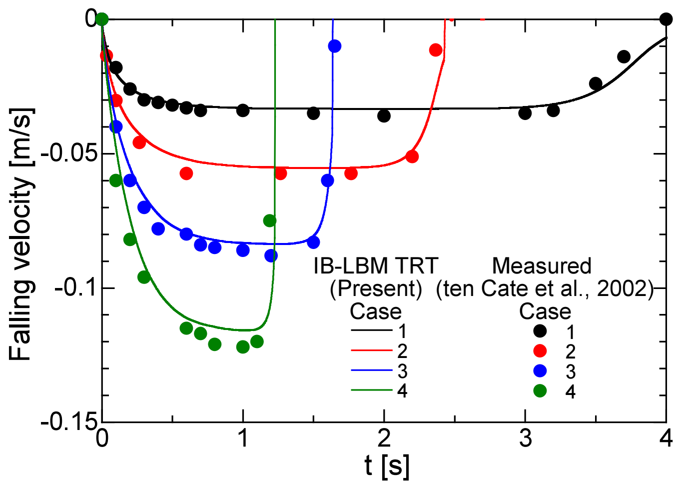

Fig. 4.6 Velocities of single spherical falling particles using IB-LBM with TRT

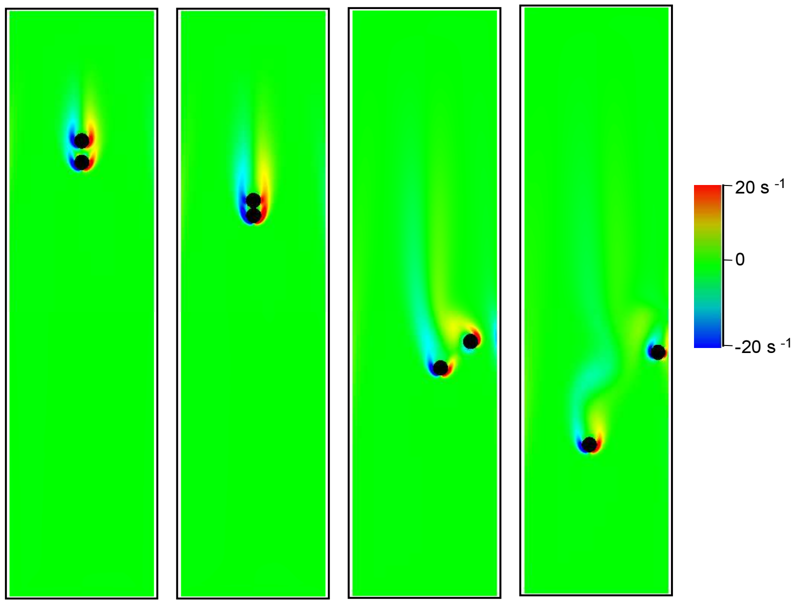

(a) t = 1 s (b) 1.5 s (c) 3 s (d) 4 s

Fig. 4.7 Two-dimensional DKT motion of two particles using IB-LBM with TRT

Figures 4.7 (a)-(d) show the particle motion predicted using IB-LBM with TRT. The trailing particle approaches the leading particle (drafting) at t = 1 s. Then they collide with each other (kissing) at t = 1.5 s. After collision, the leading particle is pushed toward the side wall and the trailing particle falls faster (tumbling). This motion is similar to the prediction using IB-FDLBM. Good agreements for the particle paths between the present method and the numerical result by Niu et al. [2006] are obtained as shown in Fig. 4.8.

A three-dimensional simulation is also performed. The computational setup and the fluid properties are the same as those explained in Section 2.3.2. The relaxation time, τ_+, is 0.575 and the time step is 1×10^{-3} s. Predicted particle motion and paths are shown in Figs. 4.9 and 4.10. The particles paths in the x- and z-axis agree with those obtained by using IB-FDLBM. The difference in the particle paths in the y-direction might be due to difference in the schemes and also in the coefficients of the collision model.

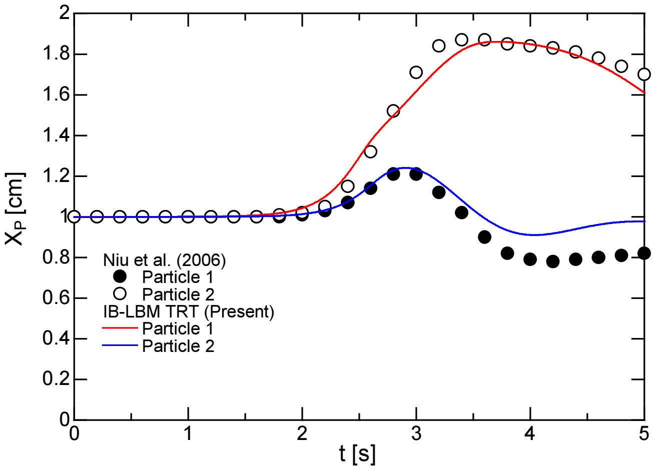

(a) X_P

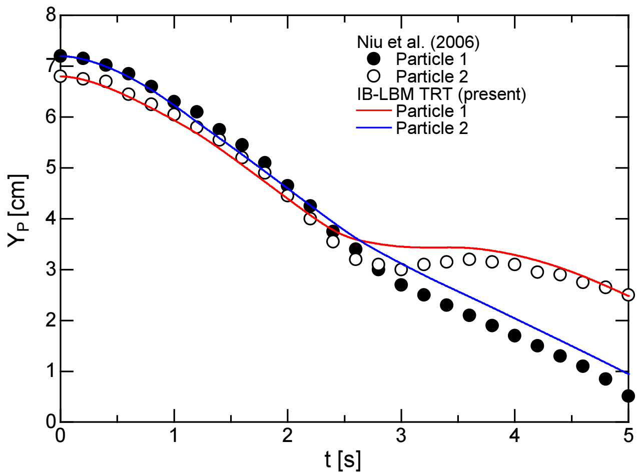

(b) Y_P

Fig. 4.8 Particle position (X_P, Y_P) of two-dimensional DTK motion of two particles with IB-LBM using TRT

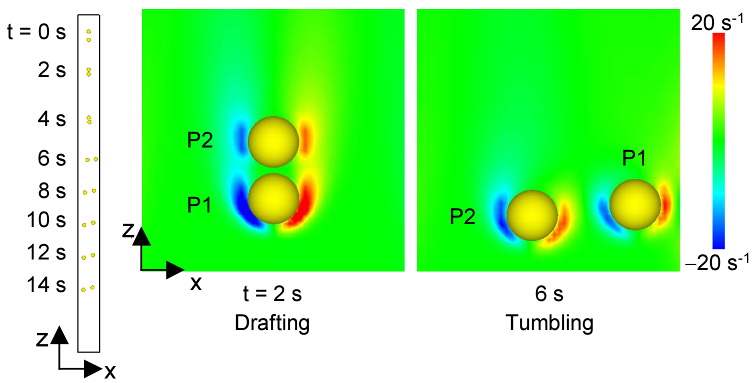

Fig. 4.9 DTK motion of two spherical particles using IB-LBM with TRT

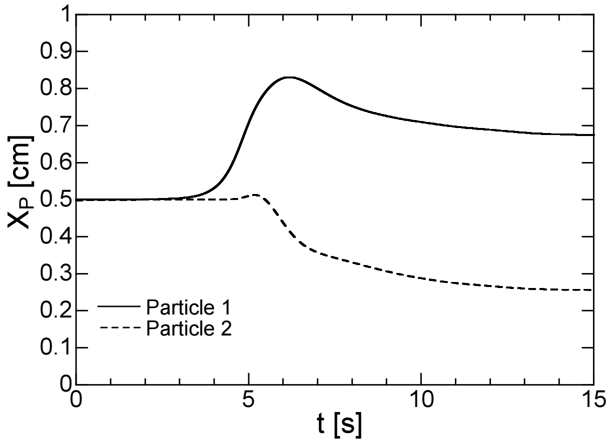

(a) X_P

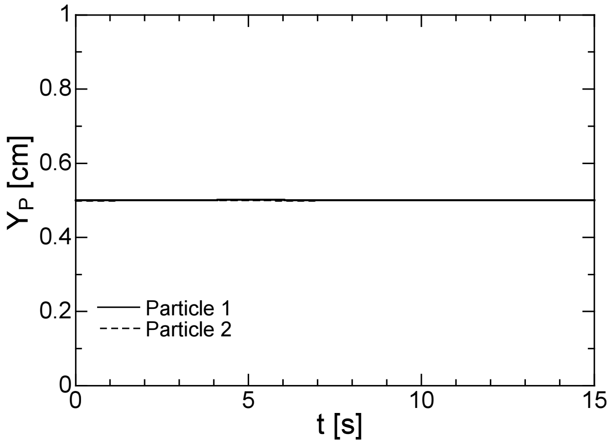

(b) Y_P

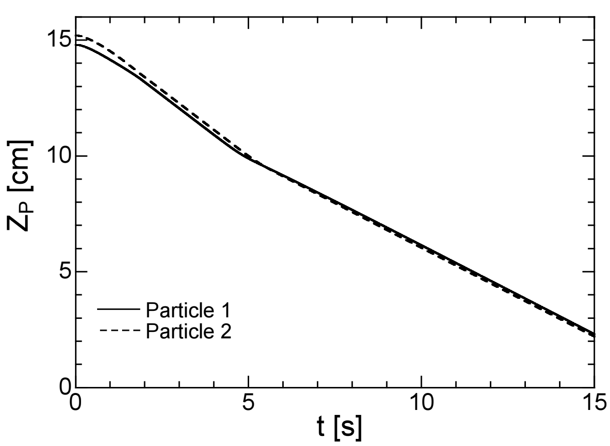

(c) Z_P

Fig. 4.10 Particle path of DTK motion of two spherical particles computed with IB-LBM using TRT

4.3 Error analysis for IB-LBM with TRT

The effect of the two-relaxation time collision model on the numerical error in IB-LBM with TRT is analyzed in this section. For simplicity, a modified version of IB-LBM proposed by Dupuis et al. [2008] is used:

$$f_i(\boldsymbol{x}+\boldsymbol{c}_i\Delta t, t+\Delta t) = f_i(\boldsymbol{x},t) - \frac{1}{\tau_+}[f_i^+ - f_i^{eq,+}] - \frac{1}{\tau_-}[f_i^- - f_i^{eq,-}] + \Delta t G_i(\boldsymbol{x},t) \tag{4.15}$$

The forcing term, G_i, with first-order accuracy is given by Eq. (1.19).

The velocity distribution of two-dimensional steady incompressible shear flows in the x direction is considered:

$$\rho = const,\ v = 0,\ \frac{du}{dx} = 0,\ \text{ and }\ \frac{du}{dt} = 0 \tag{4.16}$$

where $\boldsymbol{u}$ = (u, v) and $\boldsymbol{G}$ = (G, 0) in two dimensions. The process to obtain the analytical solution is similar to those proposed by He et al. [1997] and Le & Zhang [2009]. Since $f_i(\boldsymbol{x}+\boldsymbol{c}_i\Delta t,\ t+\Delta t) = f_i(\boldsymbol{x},\ t)$ for i = 1 and 3 in the steady state, Eq. (4.15) reduces to

$$\frac{1}{\tau_+}\left\{\frac{f_1^j + f_3^j}{2} - \frac{\rho}{9}\left(1+\frac{3u_j^2}{c^2}\right)\right\} + \frac{1}{\tau_-}\left(\frac{f_1^j - f_3^j}{2} - \frac{\rho u_j}{3c}\right) = \frac{\Delta x \rho G_j}{3c^2} \tag{4.17}$$

$$\frac{1}{\tau_+}\left\{\frac{f_3^j + f_1^j}{2} - \frac{\rho}{9}\left(1+\frac{3u_j^2}{c^2}\right)\right\} + \frac{1}{\tau_-}\left(\frac{f_3^j - f_1^j}{2} - \frac{\rho u_j}{3c}\right) = -\frac{\Delta x \rho G_j}{3c^2} \tag{4.18}$$

Here the subscript j denotes the position of the lattice point along the y-axis. Subtracting Eq. (4.17) from Eq. (4.18) yields

$$f_1^j - f_3^j = \frac{2\rho}{3c}\left(u_j + \frac{\Delta x \tau\_ G_j}{c}\right) \tag{4.19}$$

According to the definitions of the equilibrium distribution function (Eq. (1.6)), the discrete forcing term (Eq. (1.19)), f^+ and f^- (Eqs. (4.2)-(4.7)), and Eq. (4.15) in the steady state, the following relations are obtained:

$$\begin{aligned} f_5^j = &\left\{1 - \frac{1}{2}\left(\frac{1}{\tau_+} + \frac{1}{\tau_-}\right)\right\} f_5^{j-1} - \frac{1}{2}\left(\frac{1}{\tau_+} - \frac{1}{\tau_-}\right) f_7^{j-1} \\ &+ \frac{\rho}{36\tau_+}\left(1 + \frac{3u_{j-1}^2}{c^2}\right) + \frac{\rho u_{j-1}}{12c\tau_-} + \frac{\Delta x \rho G_{j-1}}{12c^2} \end{aligned} \tag{4.20}$$

$$\begin{aligned} f_6^j = &\left\{1 - \frac{1}{2}\left(\frac{1}{\tau_+} + \frac{1}{\tau_-}\right)\right\} f_6^{j-1} - \frac{1}{2}\left(\frac{1}{\tau_+} - \frac{1}{\tau_-}\right) f_8^{j-1} \\ &+ \frac{\rho}{36\tau_+}\left(1 + \frac{3u_{j-1}^2}{c^2}\right) - \frac{\rho u_{j-1}}{12c\tau_-} - \frac{\Delta x \rho G_{j-1}}{12c^2} \end{aligned} \tag{4.21}$$

$$\begin{aligned} f_7^j = &\left\{1 - \frac{1}{2}\left(\frac{1}{\tau_+} + \frac{1}{\tau_-}\right)\right\} f_7^{j+1} - \frac{1}{2}\left(\frac{1}{\tau_+} - \frac{1}{\tau_-}\right) f_5^{j+1} \\ &+ \frac{\rho}{36\tau_+}\left(1 + \frac{3u_{j+1}^2}{c^2}\right) - \frac{\rho u_{j+1}}{12c\tau_-} - \frac{\Delta x \rho G_{j+1}}{12c^2} \end{aligned} \tag{4.22}$$

$$\begin{aligned} f_8^j = &\left\{1 - \frac{1}{2}\left(\frac{1}{\tau_+} + \frac{1}{\tau_-}\right)\right\} f_8^{j+1} - \frac{1}{2}\left(\frac{1}{\tau_+} - \frac{1}{\tau_-}\right) f_6^{j+1} \\ &+ \frac{\rho}{36\tau_+}\left(1 + \frac{3u_{j+1}^2}{c^2}\right) + \frac{\rho u_{j+1}}{12c\tau_-} + \frac{\Delta x \rho G_{j+1}}{12c^2} \end{aligned} \tag{4.23}$$

Equation (1.5) ($\rho \boldsymbol{u} = \Sigma \boldsymbol{c}_i f_i$) gives the momentum density in the x direction

$$\rho u = c\left(f_1 - f_3 + f_5 - f_6 - f_7 + f_8\right) \tag{4.24}$$

Substituting Eqs. (4.19)-(4.23) into Eq. (4.24) at two positions $j\pm1$ yields

$$\begin{aligned}&\left(2\tau_+\tau_- - \tau_+ - \tau_- + 1\right)\left(f_5^j - f_6^j - f_7^j + f_8^j\right) = \\ &\frac{\rho}{6c}\Big\{\tau_-(2\tau_+ - 1)(u_{j+1} + u_{j-1}) - 2(\tau_+ - 1)u_j \\ &\qquad - \frac{\Delta x\tau_-(4\tau_+\tau_- - 3\tau_+ - 2\tau_-)}{c}\left(G_{j+1} + G_{j-1}\right) - \frac{2\Delta x\tau_-(\tau_+ - 1)}{c}G_j\Big\}\end{aligned} \tag{4.25}$$

Substituting Eqs. (4.19) and (4.25) into (4.24) at the position j and considering Eq. (1.9) yield

$$0 = \nu\frac{u_{j+1} - 2u_j + u_{j-1}}{\Delta x^2} + G_j + \frac{3\tau_+ + 2\tau_- - 4\tau_+\tau_-}{6}\left(G_{j+1} - 2G_j + G_{j-1}\right) \tag{4.26}$$

When $\tau_+ = \tau_-$, Eq. (4.26) gives the analytical equation for IB-LBM with SRT obtained by Le & Zhang [2009]. In symmetric shear flows, the computational domain with periodic boundaries is covered by 201×201 lattice points (Fig. 4.11), and two plates moving at opposite horizontal velocities U_d and $-U_d$ are located at $y = 50\Delta x$ and $150\Delta x$. U_d is 0.01 at all the Lagrangian points, and the distance between the plates is h. The Reynolds number of the flow is defined by $Re = U_d h/\nu$. In LBM, $\Delta x = \Delta t = c = 1$. Considering G_0 is the total boundary force applied, and according to Eq. (1.16) and the cosine delta function with stencil, d:

$$\delta_h(r) = \begin{cases}\dfrac{1}{2d}\left[1 + \cos\left(\dfrac{\pi|r|}{d}\right)\right] & \text{for } |r| \le d \\ 0 & \text{for } |r| > d\end{cases}, \tag{4.27}$$

yield

$$G_{j_0}=\frac{G_0}{2},\ G_{j_{0\pm1}}=\frac{G_0}{4},\ G_{|j-j_0|\geq 2}=0 \tag{4.28}$$

where j_0 denotes the position of the moving boundaries. Due to the symmetry of the flow

$$u_{j_0+1}=u_{j_0-1} \tag{4.29}$$

Substituting Eqs. (4.28) and (4.29) into (4.26) gives the velocity difference in the immersed boundary layer (IBL):

$$u_{j_0}-u_{j_0+1}=\frac{G_0\Delta x^2}{\nu}\left(\frac{1}{4}-\frac{3\tau_+ +2\tau_- -4\tau_+\tau_-}{24}\right) \tag{4.30}$$

$$u_{j_0+1}-u_{j_0+2}=\frac{G_0\Delta x^2}{\nu}\left(\frac{1}{2}-\frac{3\tau_+ +2\tau_- -4\tau_+\tau_-}{24}\right) \tag{4.31}$$

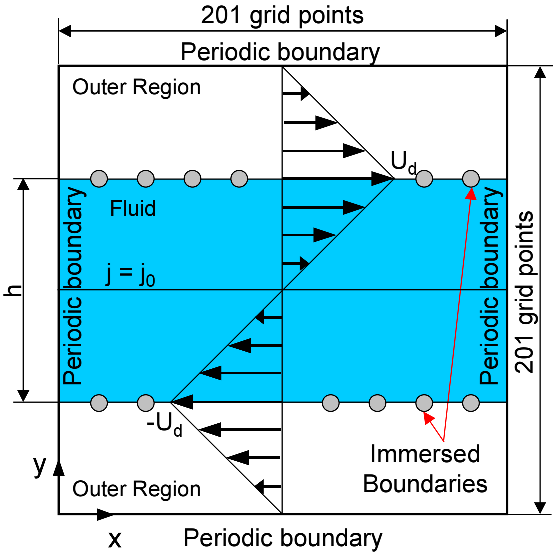

Fig. 4. 11 Computational domain for calculation of symmetric shear flows

Since the body force does not spread beyond IBL, the velocity gradient in the bulk fluid is constant:

$$u_{j-1} - u_j = \frac{G_0 \Delta x^2}{2\nu}, \quad \text{for } j > j_0 + 2 \tag{4.32}$$

Equation (4.32) means that the force applied at the boundaries induces the following bulk velocity gradient:

$$\left(\frac{du}{dy}\right)_{bulk} = \frac{G_0 \Delta x}{2\nu} \tag{4.33}$$

Since the velocity is zero at the center plane between the two plates, Eq. (4.33) gives the exact solution for the velocity at j_0

$$\bar{u}_{j_0} = \frac{G_0 \Delta x^2}{2\nu} \frac{h}{2} \tag{4.34}$$

Equation (4.32) gives the velocity at $j_0 + 2$ beyond IBL as follows:

$$u_{j_0+2} = \frac{G_0 \Delta x^2}{2\nu} \left(\frac{h}{2} - 2\right) \tag{4.35}$$

Combining Eqs. (4.30), (4.31) and (4.35) yields

$$u_{j_0} = \frac{G_0 \Delta x^2}{\nu} \left(\frac{h}{4} - \frac{1}{4} - \frac{3\tau_+ + 2\tau_- - 4\tau_+\tau_-}{12}\right) \tag{4.36}$$

$$u_{j_0 \pm 1} = \frac{G_0 \Delta x^2}{\nu} \left(\frac{h}{4} - \frac{1}{2} - \frac{3\tau_+ + 2\tau_- - 4\tau_+\tau_-}{24}\right) \tag{4.37}$$

Subtraction of Eq. (4.34) from (4.36) gives the artificial slip velocity:

$$u_{j_0}^s = u_{j_0} - \bar{u}_{j_0} = \left(\frac{4\tau_+\tau_- - 3\tau_+ - 2\tau_- - 3}{12}\right)\frac{G_0\Delta x^2}{\nu} \tag{4.38}$$

from which the following relation between τ_- and τ_+ to make $u_{j_0}^s = 0$ is deduced:

$$\tau_- = \frac{3(\tau_+ + 1)}{4\tau_+ - 2} \tag{4.39}$$

IB-LBM with SRT requires $\tau_+ \approx 1.693$ to make the boundary slip, $u_{j_0}^s$, equal to zero [Le & Zhang, 2009]. The boundary slip increases with τ and it cannot be prevented at high τ in SRT. On the other hand, IB-LBM with TRT can remove the boundary slip at any relaxation time τ_+ by setting τ_- so as to satisfy Eq. (4.39).

Substitution of Eqs. (4.36) and (4.37) into the interpolated fluid velocity $\boldsymbol{u}(\boldsymbol{X}_L, t)$ (=$\Sigma\boldsymbol{u}(x_{IJ}, t)\delta(x_{IJ}-X_L)\Delta V$) gives the boundary velocity, u_b:

$$u_b = \frac{u_{j_0}}{2} + \frac{u_{j_0+1}}{4} + \frac{u_{j_0-1}}{4} = \frac{G_0\Delta x^2}{\nu}\left(\frac{h}{4} - \frac{3}{8} - \frac{3\tau_+ + 2\tau_- - 4\tau_+\tau_-}{16}\right) \tag{4.40}$$

Substituting Eq. (4.40) into the force density $\boldsymbol{G}(\boldsymbol{X}_L, t)$ (=($\boldsymbol{u_P}(X_L, t) - \boldsymbol{u}(X_L, t))/\Delta t$) gives

$$U_d = \frac{G_0\Delta x^2}{\nu}\left(\frac{h}{4} - \frac{13}{24} + \frac{7\tau_+}{48} - \frac{\tau_-}{8} + \frac{\tau_+\tau_-}{4}\right) \tag{4.41}$$

For Newtonian fluids, the velocity gradient in the shear flow is given by $du/dy = 2U_d/h\Delta x$. From Eqs. (4.33) and (4.41), the analytical solution is therefore

$$\frac{\left(\frac{du}{dy}\right)_{bulk}}{\frac{2U_d}{h\Delta x}} = \frac{\frac{h}{4}}{\frac{h}{4} - \frac{13}{24} + \frac{7\tau_+}{48} - \frac{\tau_-}{8} + \frac{\tau_+\tau_-}{4}} \tag{4.42}$$

Equations (4.36), (4.38) and (4.41) give the normalized boundary velocity u_{j_0}/U_d, and the boundary slip velocity $u_{j_0}^s/U_d$ as follows:

$$\frac{u_{j_0}}{U_d}=\frac{\dfrac{h}{4}-\dfrac{1}{4}-\dfrac{\tau_+}{4}-\dfrac{\tau_-}{6}+\dfrac{\tau_+\tau_-}{3}}{\dfrac{h}{4}-\dfrac{13}{24}+\dfrac{7\tau_+}{48}-\dfrac{\tau_-}{8}+\dfrac{\tau_+\tau_-}{4}} \tag{4.43}$$

$$\frac{u_{j_0}^s}{U_d}=\frac{-\dfrac{1}{4}-\dfrac{\tau_+}{4}-\dfrac{\tau_-}{6}+\dfrac{\tau_+\tau_-}{3}}{\dfrac{h}{4}-\dfrac{13}{24}+\dfrac{7\tau_+}{48}-\dfrac{\tau_-}{8}+\dfrac{\tau_+\tau_-}{4}} \tag{4.44}$$

The relation between τ_+ and τ_- for making $u_{j_0}=U_d$ can be derived from Eq. (4.43):

$$\tau_-=\frac{19\tau_+-14}{4\tau_+-2} \tag{4.45}$$

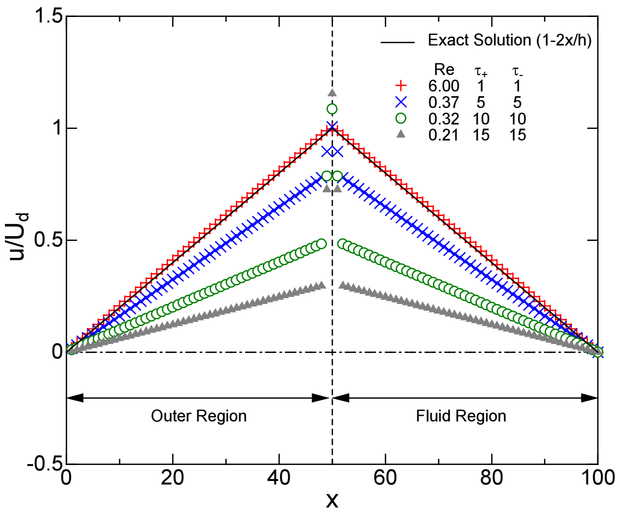

Fig. 4.12 Velocity profiles of symmetric shear flows with IB-LBM with TRT at $\tau_+ = \tau_-$

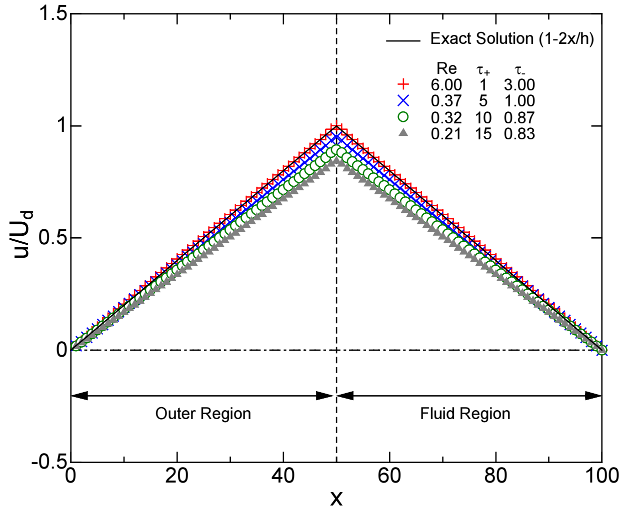

(a) $\tau_{-} = (3\tau_{+} + 3) / (4\tau_{+} - 2)$ (Eq. (4.39))

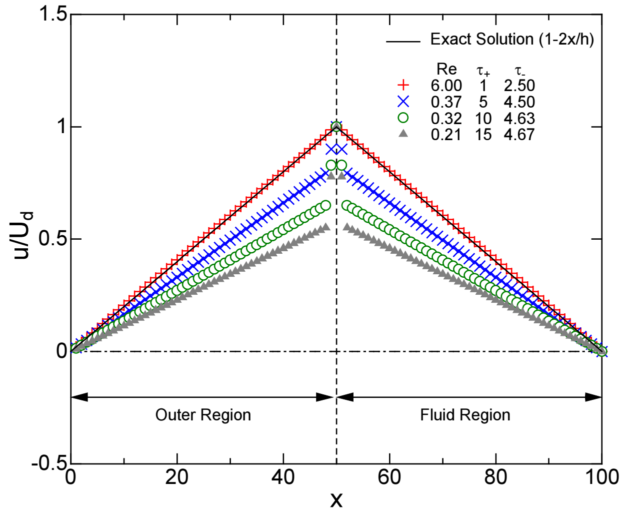

(b) $\tau_{-} = (19\tau_{+} + 14) / (4\tau_{+} - 2)$ (Eq. (4.45))

Fig. 4.13 Velocity profiles of symmetric shear flows with IB-LBM with TRT

Figures 4.12 and 4.13 show the velocity profiles of symmetric shear flows for the half of the domain. The solid line in the fluid region is the exact solution. The range of Reynolds number tested is from 6 to 0.21, i.e. τ_{+} from 1 to 15. Figure 4.12 shows the velocity profiles calculated with $\tau_{+} = \tau_{-}$ (SRT) and $d = 2\Delta x$. As mentioned above, the error in velocity near the moving plate becomes larger with decreasing *Re*, i.e. with increasing τ_{+}. The predictions

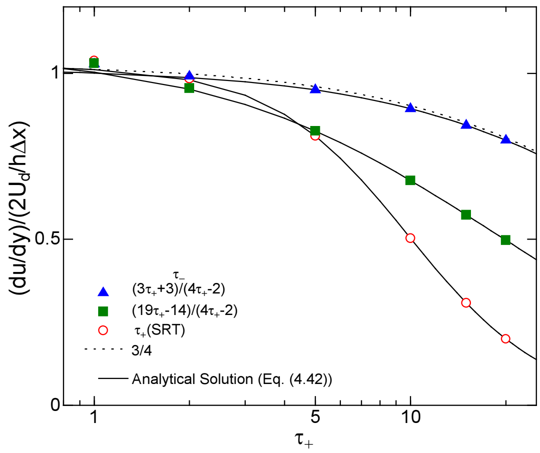

(a) Velocity gradient

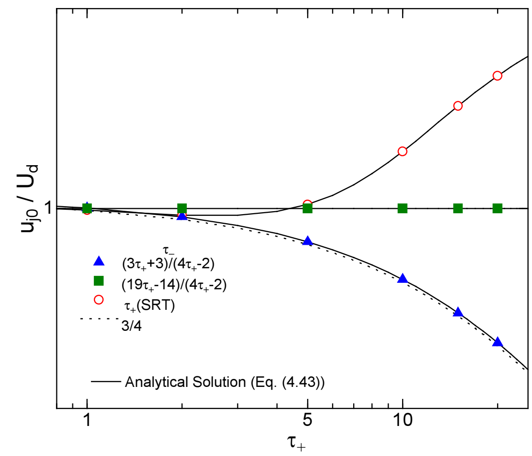

(b) Boundary velocity

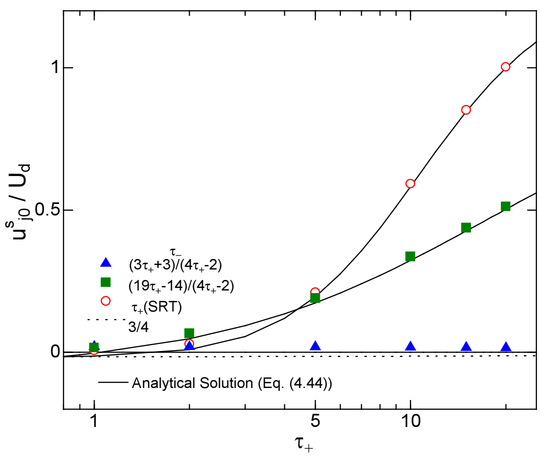

(c) Boundary slip

Fig. 4.14 Comparison of the analytical and numerical solutions obtained by using IB-LBM with TRT have also confirmed that increasing the IBL thickness, e.g. $d = 10\Delta x$, helps to reduce the discrepancy in the velocity profiles. However, this approach is limited due to the high computational cost required to deal with a thick IBL [Le & Zhang, 2009]. Figures 4.13 (a) and (b) show the velocity profiles to satisfy the boundary slip velocity $u_{j0}^{s} = 0$ and the boundary velocity $u_{j_0} = U_d$ at different Re (τ_+), i.e. Eqs. (4.39) and (4.45), respectively. However, TRT cannot deal with both issues at the same time. Evidently, the boundary slip has been removed but the fluid velocity is not accurate at high τ_+ in Fig. 4.13 (a), or the desired boundary velocity is imposed but the boundary slip is present in Fig. 4.13 (b). The velocity gradients, boundary slip velocities and boundary velocities are plotted against Re (τ_+) in Figs. 4.14 (a)-(c). Good agreements between the numerical and the analytical solutions assure the validity of the proposed analytical solutions.

4.4 Conclusions

A two-relaxation time model (TRT) for the collision term in the lattice Boltzmann equation proposed by Ginzburg was implemented into IB-LBM to remove the errors appearing in simulation of low Reynolds number flows. The external forcing term imposing the no-slip boundary condition at immersed boundaries is computed using a method proposed by Chen & Li, which is a second-order accurate temporal discretization. Simulations of circular Couette flows were carried out to validate the proposed strategy. The first- and second-order accurate formulations for the direct-forcing term and two kinds of delta functions were tested. Moving particle simulations, i.e. single circular and spherical particles falling through liquids and interaction between two particles were also performed to validate the proposed method. Then, analytical and numerical studies of the effect of TRT on symmetric shear flows were carried out. For simplicity, IB-LBM proposed by Dupuis et al. was utilized in the analysis. The velocity gradient, the boundary velocity and the boundary slip were theoretically derived. As a result, the following conclusions were obtained:

(1) IB-LBM with TRT does not cause non-physical anti-symmetric velocity distribution in circular Couette flows even at low Reynolds numbers, i.e. at high relaxation times.

(2) The two-point delta function is better than the four-point delta function at relatively high Reynolds number (low relaxation times), but worse at low Reynolds numbers (high relaxation times).

(3) The degree of accuracy in the forcing term does not affect the predictions.

(4) Two- and three-dimensional particulate flows with moving boundaries are reasonably predicted using IB-LBM with TRT.

(5) The analytical solutions obtained for the velocity gradient, the boundary velocity and the boundary slip agree well with the numerical predictions at the same conditions.

(6) The two-relaxation time collision term can remove the boundary slip velocity or accurately impose the boundary velocity at low Reynolds numbers. However, it cannot

solve both problems at the same time.

References

Bhatnagar, P., L., Gross, E., P., Krook, M., A model for collision processes in gases. I. Small amplitude processes in charged and neutral one-component systems, Physical Review, 1954, 94, pp. 511-525.

Chen, Y., Li, J., “Introducing unsteady non-uniform source terms into the lattice Boltzmann model”, International journal of Numerical Methods in Fluids, 2008, 56, pp. 629-641.

d'Humieres, D., Ginzburg, I., “Viscosity independent numerical errors for lattice Boltzmann models: from recurrence equations to magic collision numbers”, Computers and Mathematics with Applications, 2009, 58, pp. 823-840.

Dupuis, A., Chatelain, P., Koumoutsakos, P., An immersed boundary–lattice-Boltzmann method for the simulation of the flow past an impulsively started cylinder, Journal of Computational Physics, 2008, 227, pp. 4486-4498.

Feng, Z.-G., Michaelides, E. E., Robust treatment of no-slip boundary condition and velocity updating for the lattice-Boltzmann simulation of particulate flows, Computers and Fluids, 2009, 38, pp. 370-381.

Ginzburg, I., “Equilibrium type-and link-type lattice Boltzmann models for generic advection and anisotropic-dispersion equation”, Advances in Water Resources, 2005, 28, pp.1171-1195.

Ginzburg, I., Verhaeghe, F., d'Humieres, D., “Two-relaxation-time lattice Boltzmann scheme: about parametrization, velocity, pressure and mixed boundary conditions”, Communication in Computational Physics, 2008, 3(2), pp. 427-478.

Ginzburg, I., Verhaeghe, F., d'Humieres, D., “Study of simple hydrodynamics solutions with the two-relaxation times lattice Boltzmann scheme”, Communication in Computational Physics, 2008, 3(3), pp. 519-581.

He, X., Zou, Q., Luo, L.S., Dembo, M., “Analytic solutions of simple flows and analysis of nonslip boundary conditions for the lattice Boltzmann BGK model", Journal of Statistical Physics, 1997, 87, pp. 115-136.

Kang, S. K., Hassan, Y. A., A comparative study of direct-forcing immersed boundary-lattice Boltzmann methods for stationary complex boundaries, International Journal for Numerical Methods in Fluids, 2010, DOI: 10.1002/fld.2304.

Kuzmin, A., Derksen, J, "Introduction to the lattice Boltzmann method", Proceedings of the LBM workshop 2011, 2011.

Le, G., Zhang, J., Boundary slip from the immersed boundary lattice Boltzmann models, Physical Review E, 2009, 79, 026701.

Niu, X. D., Shu, C., Chew, Y. T., Peng, Y., A momentum exchange-based immersed boundary-lattice Boltzmann method for simulating incompressible viscous flows, Physical Letter A, 2006, 354, pp. 173-182.

Yang, X., Zhang, X., Li, Z., He, G.W., A smoothing technique for discrete delta functions with application to immersed boundary method in moving boundary simulations, Journal of Computational Physics, 2009, 228, pp. 7821-7836.

Yu, Z., Fan, L.-S., "Numerical simulation of bubble interactions using an adaptive lattice Boltzmann method", Chemical Engineering Science, 66 (2011) pp. 3441-3451.

5

Improvement of IB-FDLBM for accurate predictions of low Reynolds number flows

5.1. Introduction

In the previous Chapter, an immersed boundary-lattice Boltzmann method with the two-relaxation time (TRT) collision model proposed by Ginzburg et al. [2008] was proposed. It was proved through numerical calculations and theoretical analysis that the extra relaxation time in TRT can reduce the errors appearing at low Reynolds numbers in IB-LBM [Le & Zhang, 2009].

In Chapters 2 and 3, a combination of the immersed boundary method based on the direct forcing method [Dupuis et al., 2008] and the finite difference lattice Boltzmann method [Tsutahara et al., 2002] with the single-relaxation time collision model (SRT) [Bhatnagar et al., 1954] was proposed to predict particulate flows at intermediate and high Reynolds numbers. However non-physical distortion in fluid velocity appears when the Reynolds number is low, i.e. when the relaxation time is high. To ensure the applicability of IB-FDLBM to liquid-solid two-phase flows in various engineering applications, IB-FDLBM should be able to accurately simulate not only particles at high Reynolds numbers but also those at low Reynolds numbers.

The two-relaxation time collision model is, therefore, implemented into IB-FDLBM in this chapter to reduce the numerical error appearing at low Reynolds numbers. The

Chapman-Enskog expansion is applied to IB-FDLBM with TRT to show the recovery of the macroscopic conservation equations for Newtonian fluids, i.e., the continuity and Navier-Stokes equations. Then, simulations of circular Couette flows [Le & Zhang, 2009] are carried out at low Reynolds numbers to validate the proposed method. Predicted velocity distributions are compared with those obtained using SRT and with an analytical solution. Flows past a circular cylinder and a sphere are also simulated for a wide rage of the Reynolds number. The predicted drag coefficients obtained by using SRT and TRT are compared with an analytical solution and measured data for validation. The sedimentation of multiple particles at different Reynolds numbers is also simulated.

5.2. Implementation of two-relaxation time collision model into IB-FDLBM

In order to implement the two-relaxation time collision model into IB-FDLBM, the discrete Boltzmann equation with direct forcing term, Eq. (2.9), is rewritten as

$$\frac{\partial f_i}{\partial t} + \boldsymbol{c}_i \cdot \nabla[f_i + A\Omega_i] = \Omega_i + G_i \tag{5.1}$$

where Ω_i is the collision operator ($\Omega_i = (f_i - f_i^{eq}) / \tau$ in SRT) . Then, TRT collision operator [Ginzburg et al., 2008] given by Eq. (4.1) is substituted into Eq. (5.1). As a result, the discrete Boltzmann equation with the direct forcing term and the TRT collision model is given by:

$$\frac{\partial f_i}{\partial t} + \boldsymbol{c}_i \cdot \nabla\left[f_i + A\left\{ -\frac{1}{\tau_+}(f_i^+ - f_i^{eq,+}) - \frac{1}{\tau_-}(f_i^- - f_i^{eq,-}) \right\}\right] = -\frac{1}{\tau_+}(f_i^+ - f_i^{eq,+}) - \frac{1}{\tau_-}(f_i^- - f_i^{eq,-}) + G_i. \tag{5.2}$$

The relation for the distribution functions, f^+, f^-, $f^{eq,+}$ and $f^{eq,-}$, are given by Eqs. (4.2)-(4.7). Applying the Chapman-Enskog expansion to Eq. (5.2) recovers the macroscopic conservation equations for incompressible Newtonian fluids. The detailed derivation is given in the next section. The kinematic viscosity, ν, is defined as

$$\nu = \frac{1}{3}\left(\tau_+ - A\right) \tag{5.3}$$

The relaxation time, τ_-, is determined through the following parameter [Ginzburg et al., 2008]

$$\Lambda = (\tau_+ - A)(\tau_- - A) \tag{5.4}$$

The optimum values of Λ have been theoretically obtained in only a few simple cases for IB-LBM such as the one given in the previous chapter and the one in the studies by Ginzburg at al. [2008]. Λ should be tuned to improve the numerical stability and accuracy. Hence sensitivity analysis for Λ in IB-FDLBM will be carried out in this chapter.

The treatment of immersed boundaries and the solution algorithm of Eq. (5.2) are similar to those in Chapter 2, i.e. Eqs. (2.10)-(2.21).

5.3 Derivation of the macroscopic conservation equations

The macroscopic equations, i.e. the continuity and the Navier-Stokes equations, are obtained by the Chapman-Enskog expansion:

$$f_i = f_i^{(0)} + \varepsilon f_i^{(1)} + \varepsilon^2 f_i^{(2)} + \ldots \quad (5.5)$$

$$f_i^{\pm} = f_i^{\pm(0)} + \varepsilon f_i^{\pm(1)} + \varepsilon^2 f_i^{\pm(2)} + \ldots \quad (5.6)$$

$$\frac{\partial}{\partial t} = \varepsilon \frac{\partial}{\partial t_1} + \varepsilon^2 \frac{\partial}{\partial t_2} \quad (5.7)$$

$$\frac{\partial}{\partial x_\alpha} = \varepsilon \frac{\partial}{\partial x_\alpha} \quad (5.8)$$

where ε is the Knudsen number. The first four moments of the equilibrium distribution function of the D2Q9 or D3Q19 models are

$$\sum f_i^{eq} = \sum f_i^{eq,+} = \rho \quad (5.9)$$

$$\sum f_i^{eq} c_{i\alpha} = \sum f_i^{eq,-} c_{i\alpha} = \rho u_\alpha \quad (5.10)$$

$$\sum f_i^{eq} c_{i\alpha} c_{i\beta} = \sum f_i^{eq,+} c_{i\alpha} c_{i\beta} = \frac{1}{3}\rho\delta_{\alpha\beta} + \rho u_\alpha u_\beta \quad (5.11)$$

$$\sum f_i^{eq} c_{i\alpha} c_{i\beta} c_{i\gamma} = \sum f_i^{eq,-} c_{i\alpha} c_{i\beta} c_{i\gamma} = \rho u_\alpha u_\beta u_\gamma + \frac{1}{3}\rho\left(u_\alpha \delta_{\beta\gamma} + u_\beta \delta_{\alpha\gamma} + u_\gamma \delta_{\alpha\beta}\right) \quad (5.12)$$

The distribution functions $f_i^{(l)}$ and $f_i^{\pm(l)}$ satisfy

$$\sum f_i^{(l)} = 0 \quad (5.13)$$

$$\sum f_i^{(l)} c_{i\alpha} = 0 \tag{5.14}$$

$$\sum f_i^{(l)\pm} = 0 \tag{5.15}$$

$$\sum f_i^{(l)\pm} c_{i\alpha} = 0 \tag{5.16}$$

for $l \geq 1$. Substituting Eqs. (5.5)-(5.8) into Eq. (5.2) yields the following equations for the orders of ε^0, ε^1 and ε^2:

$$\varepsilon^0 : f_i^{(0)} = f_i^{eq} \tag{5.17}$$

$$\varepsilon^1 : \frac{\partial}{\partial t_1} f_i^{(0)} + c_{i\alpha} \frac{\partial}{\partial x_\alpha} f_i^{(0)} = -\frac{1}{\tau_+} f_i^{(1)+} - \frac{1}{\tau_-} f_i^{(1)-} \tag{5.18}$$

$$\begin{aligned} \varepsilon^2 : &\frac{\partial}{\partial t_1} f_i^{(1)} + \frac{\partial}{\partial t_2} f_i^{(0)} + c_{i\alpha} \frac{\partial}{\partial x_\alpha} f_i^{(1)} \\ &- A c_{i\alpha} \frac{\partial}{\partial x_\alpha} \left[\frac{1}{\tau_+} f_i^{(1)+} + \frac{1}{\tau_-} f_i^{(1)-} \right] = -\frac{1}{\tau_+} f_i^{(2)+} - \frac{1}{\tau_-} f_i^{(2)-} \end{aligned} \tag{5.19}$$

To obtain $f_i^{(1)}$, the symmetric and anti-symmetric parts are derived from Eq. (5.18)

$$f_i^{(1)} = -\tau_+ \left(\frac{\partial}{\partial t_1} f_i^{(0)+} + c_{i\alpha} \frac{\partial}{\partial x_\alpha} f_i^{(0)-} \right) - \tau_- \left(\frac{\partial}{\partial t_1} f_i^{(0)-} + c_{i\alpha} \frac{\partial}{\partial x_\alpha} f_i^{(0)+} \right) \tag{5.20}$$

Summing Eqs. (5.18) and (5.19) over i yields

$$\frac{\partial \rho}{\partial t_1} + \frac{\partial \rho u_\alpha}{\partial x_\alpha} = 0 \tag{5.21}$$

$$\frac{\partial \rho}{\partial t_2} = 0 \tag{5.22}$$

Combining Eq. (5.21) and (5.22) gives the continuity equation:

$$\frac{\partial \rho}{\partial t} + \frac{\partial \rho u_\alpha}{\partial x_\alpha} = 0 \tag{5.23}$$

Multiplying Eqs. (5.18) and (5.19) by $c_{i\alpha}$ and summing the resultant equations over i yields

$$\frac{\partial \rho u_\alpha}{\partial t_1} + \frac{\partial}{\partial x_\beta}\left(\frac{1}{3}\rho\delta_{\alpha\beta} + \rho u_\alpha u_\beta\right) = 0 \tag{5.24}$$

$$\frac{\partial \rho u_\alpha}{\partial t_2} - (\tau_+ - A)\frac{\partial}{\partial x_\beta}\left(\frac{1}{3}\rho\frac{\partial u_\alpha}{\partial x_\beta} + \frac{1}{3}\rho\frac{\partial u_\beta}{\partial x_\alpha}\right) + (\tau_+ - A)\frac{\partial}{\partial x_\alpha}\left(\frac{\partial u_\alpha u_\beta u_\gamma \rho}{\partial x_\beta}\right) = 0 \tag{5.25}$$

Combining Eqs. (5.24) and (5.25) yields the Navier-Stokes equation:

$$\frac{\partial \rho u_\alpha}{\partial t} + \frac{\partial \rho u_\alpha u_\beta}{\partial x_\beta} = -\frac{\partial p}{\partial x_\alpha} + \nu\frac{\partial}{\partial x_\beta}\left[\rho\left(\frac{\partial u_\alpha}{\partial x_\beta} + \frac{\partial u_\beta}{\partial x_\alpha}\right)\right] \tag{5.26}$$

where the pressure p is given by $p=\rho/3$.

5.4 Validation

5.4.1 Circular Couette flows

Calculations of two-dimensional circular Couette flows are carried out to confirm that the proposed method can reduce non-physical distortion in velocity field at low Reynolds numbers. The numerical condition is similar to that used in Le & Zhang [2009] (Fig. 1.5).

In order to optimize computational resources, the number of Lagrangian points is determined so as to make the spacing between two points on the outer cylinder comparable to the grid spacing. The number of Lagrangian points is therefore 440 for each cylinder surface. Different numbers of Lagrangian points, e.g. 880 and 220, were also tested and no significant differences were found in the predicted velocity fields. The negative viscosity term, A, is set at 0.5, and $\Lambda = 1/4$. The range of Reynolds number tested is $0.038 \leq Re \leq 1.5$, i.e. $1 \leq \tau_+ \leq 20$.

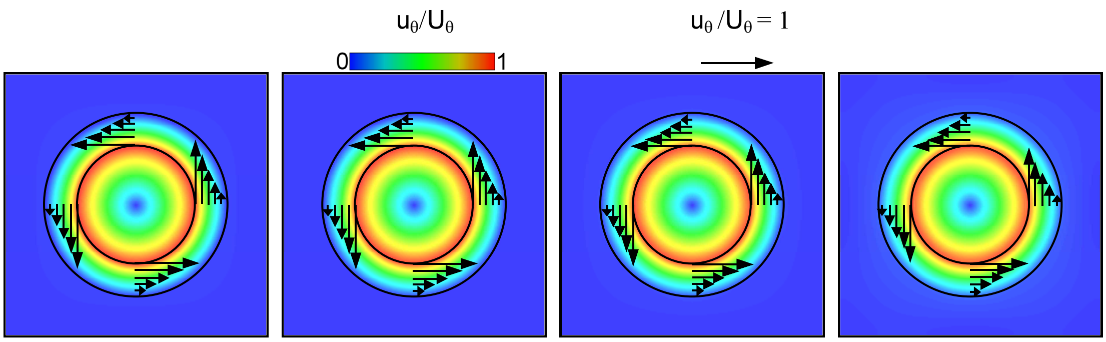

(a) (Re,τ_+,τ_-)=(1.5, 1, 1) (b) (0.17, 5, 0.56) (c) (0.079, 10, 0.53) (d) (0.038, 20, 0.51)

Fig. 5.1 Velocity distributions and velocity vector predicted by using IB-FDLBM with TRT.

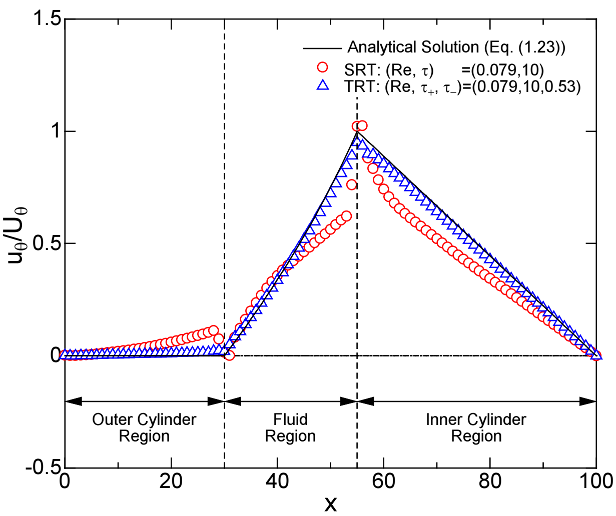

Fig. 5.2 Velocity profiles of circular Couette flows along a horizontal line at $Re = 0.079$ ($\tau = \tau_+ = 10$) obtained using IB-FDLBM

Figures 5.1 (a)-(d) show the azimuthal velocity distribution, u_θ/U_θ, obtained using IB-FDLBM with TRT. The non-symmetric velocity distortion is not formed even at low Reynolds numbers. A comparison of the velocity profiles along a horizontal cross-section obtained with SRT, TRT and the analytical solution (Eq. (1.23)) at *Re* = 0.079 ($\tau = \tau_+ = 10$) is shown in Fig. 5.2. The solution obtained with TRT agrees well with the analytical solution, whereas that obtained with SRT differs from the analytical solution, especially in the vicinity of the immersed boundary. The errors defined by Eq. (4.14) in velocity distribution are plotted against the Reynolds number in Fig. 5.3. The trend is similar to that obtained using IB-LBM. However slightly smaller errors are obtained using IB-FDLBM with TRT.

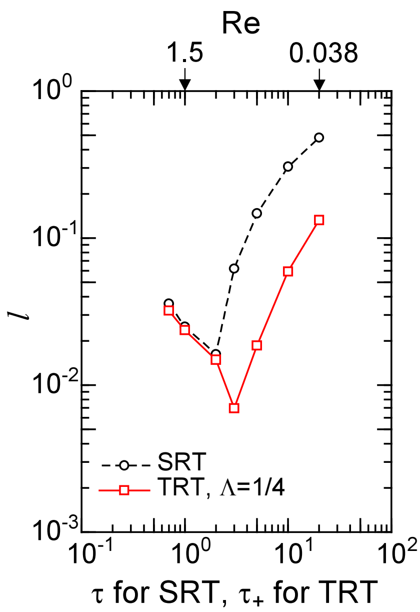

Fig. 5.3 Errors obtained by using IB-FDLBM with SRT and TRT at different Reynolds numbers

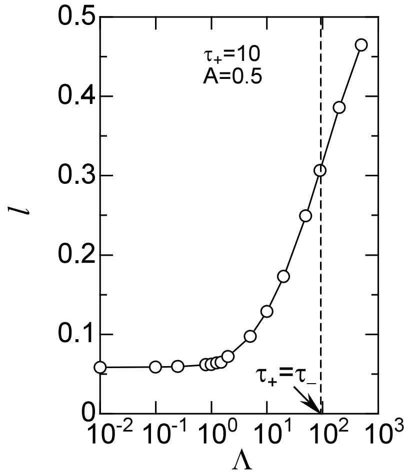

Fig. 5.4 Effects of Λ on numerical error, l, in circular Couette flow simulation at Re = 0.079 (τ_+=10)

The effects of Λ on the error in the velocity distribution of circular Couette flows at Re = 0.079 (τ_+ = 10) is shown in Fig. 5.4. TRT reduces to SRT ($\tau_+ = \tau_-$) at Λ = 90, at which l is about 0.3. The error decreases down to 0.06 as Λ decreases. The error in TRT is larger than that in SRT when Λ > 90, i.e. $\tau_- > \tau_+$. Therefore τ_- must be smaller than τ_+. Higher spatial resolutions, i.e. 401 and 801 lattice points for the domain width, were also tested to confirm that the error decreases with increasing the spatial resolution.

5.4.2 Flows past a circular cylinder at low Reynolds numbers

It was demonstrated in Chapter 3 that IB-FDLBM with SRT gives reasonable predictions of the drag coefficients of a two-dimensional circular cylinder at intermediate and high Reynolds numbers, i.e. $1 \leq Re \leq 10^5$. The applicability of the method to low Reynolds number flows (Re < 1), however, has not been examined. Therefore the applicability of IB-FDLBM with SRT to flows past the circular cylinder at low Re is first investigated.

The computational domain is shown in Fig. 1.2. A large computational domain, i.e. W = 100D and H = 80D in the x and y directions, is required to make the effects of the boundaries on the flow about the cylinder negligible because the viscous force is dominant when $Re < 1$. The cylinder is located at $(x, y) = (40D, 40D)$. The ratio of the cylinder diameter to the lattice spacing, $D/\Delta x$, is 40. The number of Lagrangian points, which are evenly distributed at the cylinder surface, is 126. The coefficient of the additional collision term A is set at 0.5. The free stream velocity, U_0, is 0.05.

Figure 5.5 shows the streamlines of the flows at $Re = 0.1$, at which $\tau = 60.5$. There are two problems: (1) the non-physical distortion in the velocity field and (2) the penetration of the streamlines into the cylinder. The former is caused by the numerical error of SRT as discussed in Section 4.1. The latter is caused not by the numerical error of SRT but by that of the direct forcing method to impose the no-slip boundary condition in IB-FDLBM. As pointed out by Wu & Shu [2009], the cause of penetration is that the direct forcing term, Eq. (2.10), for the Lth Lagrangian point does not include the effects of the forcing by the neighboring Lagrangian points. They also proposed an implicit direct forcing method for IB-LBM to prevent the non-physical penetration. The implicit direct forcing method is therefore implemented into IB-FDLBM in the next section.

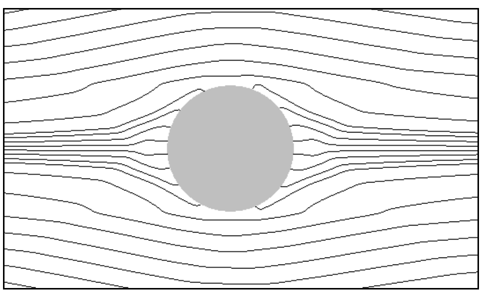

Fig. 5.5 Streamlines of flow past a cylinder at $Re = 0.1$ ($\tau = 60.5$) predicted using IB-FDLBM with SRT

5.5 Preventing penetration of the fluid flow into particles

5.5.1 Implicit direct forcing method

For the implementation of the implicit direct forcing method, the discrete Boltzmann equation, Eq. (5.1), without the forcing term, G_i, is used to obtain the predictor, f_i^*, of the distribution function. The predictor of $\boldsymbol{u}$ at the Eulerian grid points is obtained by $\boldsymbol{u}^* = \Sigma \boldsymbol{c}_i f_i^* / \rho$. The corrector, $\Delta\boldsymbol{u}(\boldsymbol{X}_L, t)$, of velocity to impose $\boldsymbol{u}_P(\boldsymbol{X}_L, t) = \boldsymbol{u}(\boldsymbol{X}_L, t)$ is obtained by solving the following simultaneous linear equations

$$\begin{aligned}\sum_{\boldsymbol{x}_{IJK}\in\Delta}\sum_{L=1}^{N_m}\Delta\boldsymbol{u}(\boldsymbol{X}_L,t)\delta(\boldsymbol{x}_{IJK}-\boldsymbol{X}_L)\Delta x\Delta S\delta(\boldsymbol{x}_{IJK}-\boldsymbol{X}_L)\Delta V \\ = \sum_{\boldsymbol{x}_{IJK}\in\Delta}\boldsymbol{u}^*(\boldsymbol{x}_{IJK},t)\delta(\boldsymbol{x}_{IJK}-\boldsymbol{X}_L)\Delta V-\boldsymbol{u}_P(\boldsymbol{X}_L,t)\end{aligned} \tag{5.27}$$

$\boldsymbol{u}^*$ is corrected as

$$\boldsymbol{u}(\boldsymbol{x}_{IJK},t)=\boldsymbol{u}^*(\boldsymbol{x}_{IJK},t)+\sum_{L=1}^{N_m}\Delta\boldsymbol{u}(\boldsymbol{X}_L,t)\delta(\boldsymbol{x}_{IJK}-\boldsymbol{X}_L)\Delta x\Delta S \tag{5.28}$$

The force, $\boldsymbol{G}$, is given by

$$\boldsymbol{G}(\boldsymbol{X}_L,t)=\rho\frac{\Delta\boldsymbol{u}(\boldsymbol{X}_L,t)}{\Delta t} \tag{5.29}$$

The forcing term, G_i, is calculated using Eq. (2.15), and then, the distribution function is updated as $f_i^{n+1} = f_i^* + G_i$.

The four-point piecewise delta function (Eq. (4.12)) [Yang et al., 2009] is used in the implicit method. The second-order Runge-Kutta method and the third-order upwind scheme

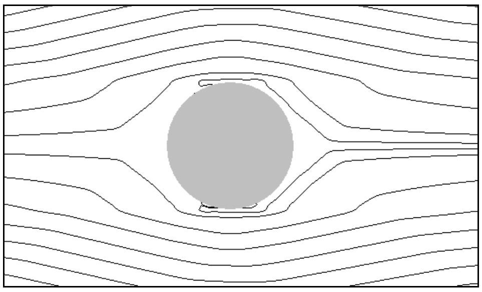

Fig. 5.6 Streamlines of flow past a cylinder at *Re* = 0.1 predicted using SRT and the implicit direct forcing method.

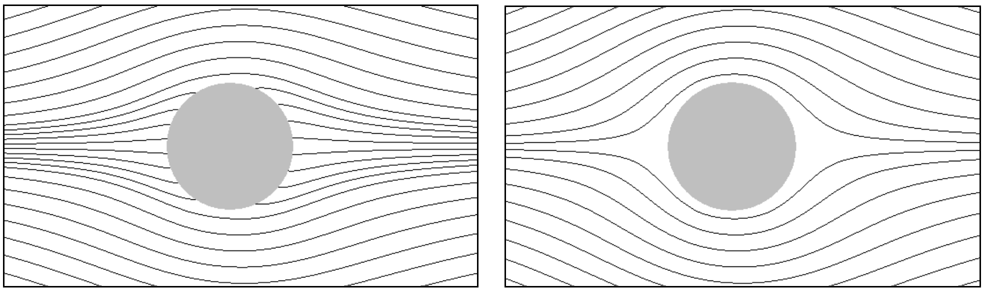

(a) Explicit direct forcing method (b) Implicit direct forcing method

Fig. 5.7 Streamlines of flow past a cylinder at *Re* = 0.1 predicted using TRT

are used to discretize Eq. (5.1). Hereafter the direct forcing method in Chapters 2 and 3 is referred to as the explicit direct forcing method.

5.5.2 Flows past a circular cylinder

The flow past the circular cylinder at *Re* = 0.1 is calculated using SRT and the implicit direct forcing method to validate the implicit direct forcing method. As shown in Fig. 5.6, the penetration is successfully prevented. The non-physical distortion in the velocity field however still remains.

Figures 5.7 (a) shows the streamlines of the flow at *Re* = 0.1 predicted using IB-FDLBM with TRT and the explicit direct forcing method. The parameter Λ is 1/4. Non-physical velocity distortion is not present. However the penetration takes place as in Fig. 5.5. The penetration can be prevented using the implicit direct forcing method as shown in Fig. 5.7

(b). Therefore IB-FDLBM with TRT and the implicit direct forcing method allows us to solve the aforementioned problems, i.e. the non-physical velocity distortion and the penetration of flow into the solid body.

Then the effects of Λ on the numerical stability are investigated. The same computational domain is used at $Re = 0.1$, whereas the domain sizes are $W = 50D$ and $H = 40D$ in the x and y directions and the cylinder is located at $(x, y) = (20D, 20D)$ when $Re \geq 1$. Figure 5.8 shows a diagram to distinguish acceptable and unacceptable parameter spaces, in which there is non-physical distortion of the velocity field or numerical instability arises in the calculation. The unacceptable region appears at high Λ and it becomes wider with increasing Re. Therefore for stable calculation Λ should be decreased as Re increases. The dashed line represents Λ for $\tau_+ = \tau_-$, at which TRT reduces to SRT. For $Re > 2$, both SRT and TRT can be used to stably simulate the flows. SRT however lies in the unacceptable region at lower Reynolds numbers.

The predicted drag coefficients are compared with measured data [Wieselsberger, 1922] and the following analytical solution [Lamb, 1911]:

$$C_D = \frac{8\pi}{Re\left(\frac{1}{2} - \gamma - \ln\frac{Re}{8}\right)} \tag{5.30}$$

where $\gamma = 0.57721$.

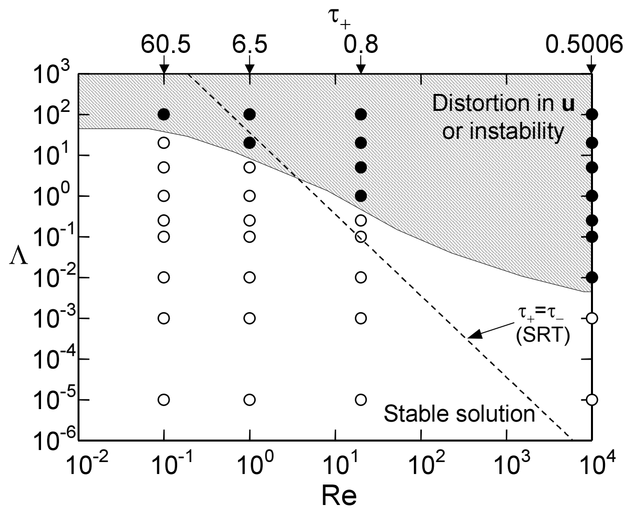

Closed symbol: distortion in **u** or instability is present. Open symbol: stable and accurate solution

Fig. 5.8 Effect of Λ on numerical stability in calculation of flow past a circular cylinder. The spatial resolution is fixed at $D/\Delta x = 40$. The explicit direct forcing method is used when $Re \geq 1$, whereas the implicit direct forcing method is used at $Re = 0.1$.

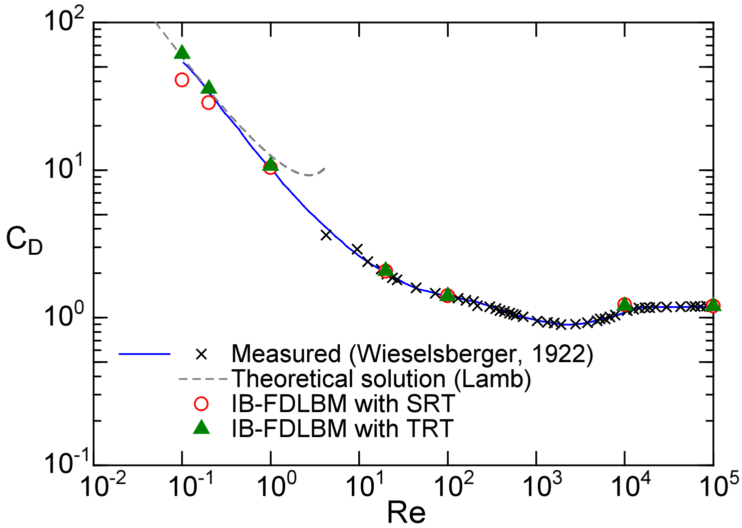

Fig. 5.9 Drag coefficient of flows past a circular cylinder at low *Re*.

Figure 5.9 shows the predicted drag coefficients. The parameter Λ in TRT is 1/4 for $Re \leq 1$, whereas it is 10^{-2}, 10^{-3}, 10^{-8} and 10^{-9} at Re = 20, 100, 10000 and 100000, respectively. Reasonable agreements between the predictions and the measured data are obtained using

SRT for $Re \geq 1$ as reported in Chapter 3. The error in C_D increases as Re decreases for $Re <$ 1.

Good predictions at high Reynolds numbers are obtained using TRT. Moreover, TRT gives more accurate predictions of C_D at low Re than SRT. The advantage of the implementation of TRT is also demonstrated in calculations of flows past a circular cylinder using the body-fitted FDLBM shown in appendix D.

5.5.3 Flows past a sphere

In Chapter 3, good predictions of flows past a sphere at intermediate and high Reynolds numbers were obtained by using explicit IB-FDLBM with SRT. In this section the range of Reynolds number is extended to calculate flows at low Reynolds numbers, i.e. $0.1 \leq Re \leq 10000$. The numerical setup is the same as that one utilized in Chapter 3: the domain size is ($50D$, $40D$, $40D$), the position of the sphere is ($20D$, $20D$, $20D$) and $D/\Delta x$ is 40. The number of Lagrangian points at the sphere surface is 4958 [Feng & Michaelides, 2005]. A is set at 0.5. The inflow velocity is 0.05.

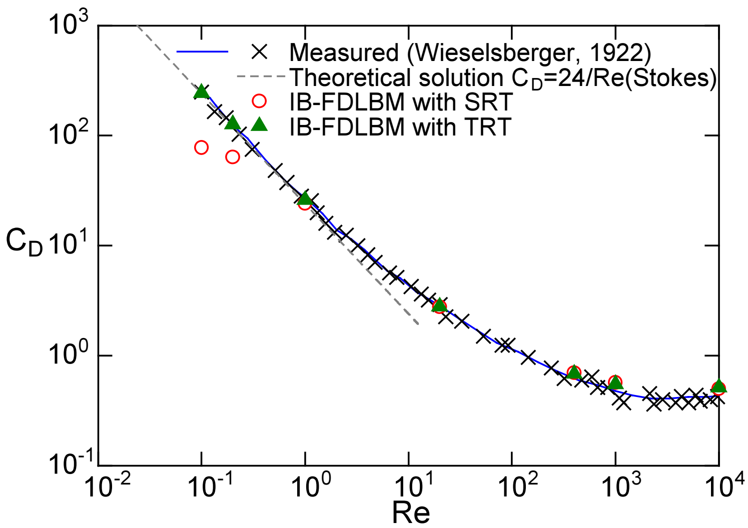

Fig. 5.10 Drag coefficients of flows past a sphere

Various Reynolds numbers, i.e. Re = 0.1, 0.2, 1, 20, 400, 1000, 10000, are tested. The parameter Λ is 1/4 for $Re \leq 1$, whereas it is 10^{-2}, 10^{-4}, 10^{-5} and 10^{-8} at Re = 20, 400, 1000 and 10000, respectively. The explicit direct forcing method is used for $Re \geq 1$, whereas the implicit method is used for $Re < 1$.

Predicted drag coefficients are plotted against the Reynolds number in Fig. 5.10. Despite good predictions of the drag coefficient are obtained at intermediate and high Reynolds number using SRT, the predicted drag coefficients at Re = 0.1 and 0.2 show large errors from the measured values [Wieselsberger, 1922] and theoretical solution. Non-physical velocity distortion similar to that in Fig. 5.5 is also present in these calculations. In contrast, TRT gives good predictions of C_D at low and high Reynolds numbers, and non-physical velocity distortion is not formed at low Reynolds numbers.

5.6 Simulation of particles at different Reynolds numbers

Most particulate flows in engineering practice consist of particles with various sizes and various physical properties. Since the particle Reynolds number, Re, is a function of the particle diameter, particle velocity and the fluid viscosity, Re of particulate flows varies widely. In this section, two-dimensional sedimentation of multiple particles with various diameters and densities is carried out to demonstrate that IB-FDLBM can predict particulate flows for a wide range of particle Reynolds numbers. Due to the limitation in the memory size and speed of the computer, two cases are simulated to show the benefits of the present method. First, the calculation of flows for a wide range of Reynolds number is carried out, and then, multiple particles at low and moderate Reynolds numbers are simulated.

Figure 5.11 (a) shows the computational domain for the former. All the domain boundaries are no-slip walls. The computational domain size is 8 cm and 80 cm in the x and y directions, respectively. The number of lattice points in the x and y directions are 401 and 4001. The lattice spacing, Δx, is 0.02 cm. The total number of particles is 45. The diameter of the largest particles, D, is 1 cm and their initial positions are (x, y) = (2 cm, 78 cm) and (6 cm, 78 cm). Their density is 8.0×10^3 kg/m^3, and their initial velocity is 30 cm/s. All the other particles are initially at rest. The diameter of these particles varies from 0.6 cm to 0.36 cm, and they are located in an array at the upper half of the domain starting from 42 cm in the y direction. The density is 1.3×10^3 kg/m^3. The fluid density and viscosity are 1.0×10^3 kg/m^3 and 2.0×10^{-2} Pa·s, respectively. The magnitude of acceleration of gravity, g, is 9.81 m/s^2. The parameters for collision terms are $\tau_+ = 0.65$, $A = 0.5$ and $\Lambda = 0.001$. The time step size is 5×10^{-5} s. The number of Lagrangian points at the surface of each particle is determined so as to make the spacing between two adjacent points on the surface comparable to the grid spacing. Thus, the numbers of Lagrangian points of the largest and smallest particles are 157 and 56, respectively.

Figures 5.11 (b)-(e) show the vorticity contour of the motion of multiple particles. At t = 0.45 s, the largest particles rapidly fall due to their initial velocity, and the vortex shedding can be observed behind the particles. At this time, the other particles fall slowly. The Reynolds number, Re, in the system varies from 9 for the smallest particles to 370 for the largest particles. As the largest particles approach the other particles, the motion of the particles becomes chaotic, and a complex wake structure is observed after the collision of particles at t = 0.7 s. The largest particles continue falling rapidly at t = 0.8 s. The small particles also continue falling, and their particle paths are strongly affected by the complex wake structure of the largest particle.

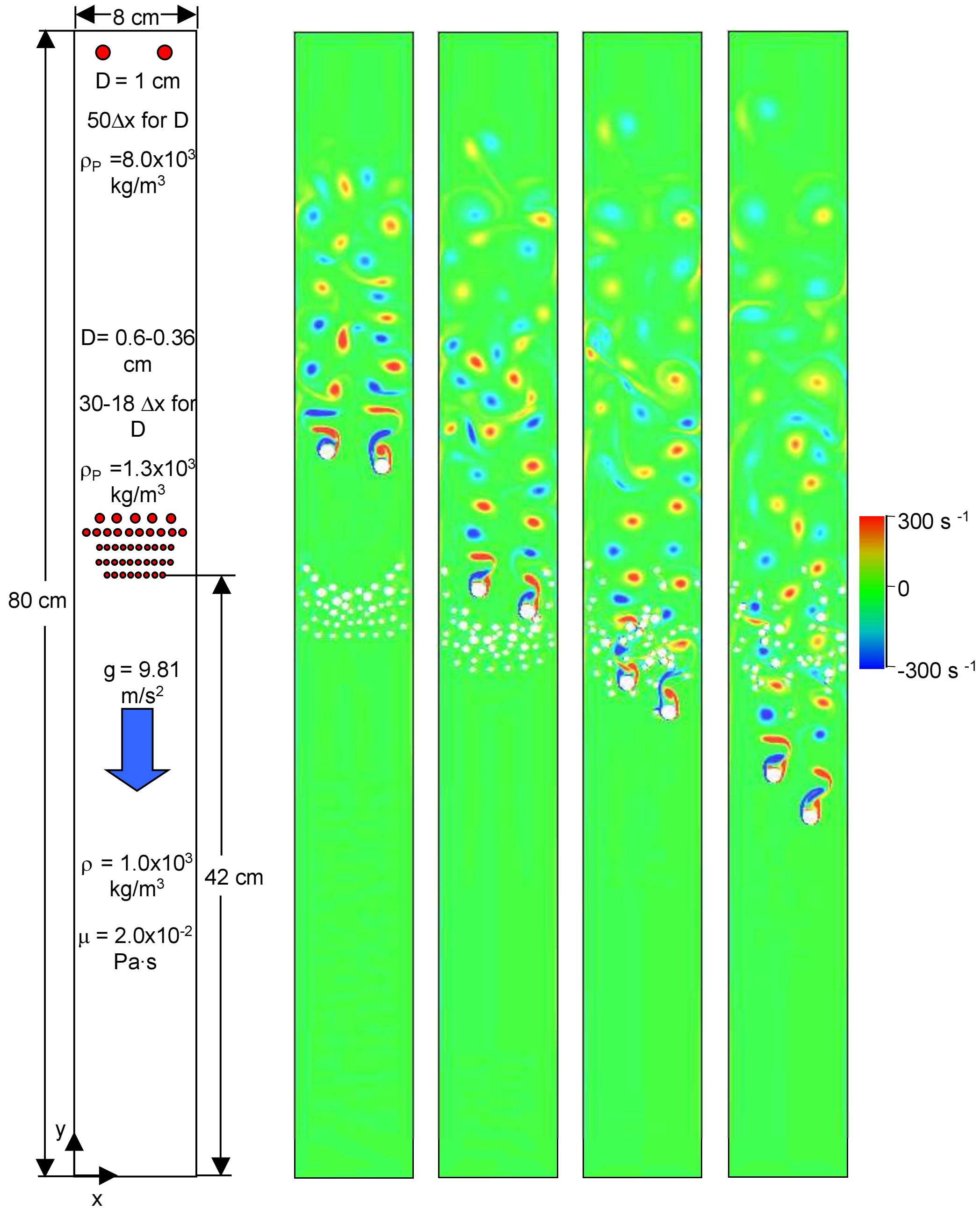

(a) (b) t =0.45 s (c) 0.60 s (d) 0.70 s (e) 0.80 s

Fig. 5.11 Computational domain (a) and vorticity contour of sedimentation of multiple particles

Then, multiple particles at low and moderate Reynolds numbers are simulated to make clear the advantage of the present method. Figure 5.12 (a) shows the computational domain. All the domain boundaries are no-slip walls. The computational domain size is 0.5 cm and 6 cm in the x and y directions, respectively. The numbers of lattice points in the x and y directions are 501 and 6001. Δx is 0.001 cm. The total number of particles is 10. The diameter of the largest particle, D, is 0.1 cm and their initial positions are (x, y) = (0.25 cm, 5.8 cm). Its density and initial velocity are 8.0×10^3 kg/m^3 and 6 cm/s, respectively. All the other particles are initially at rest. The diameter of these particles is 0.025 cm, and they are located in the x direction 1 cm above the bottom boundary. The particle density is 1.3×10^3 kg/m^3. The fluid density and viscosity are 1.0×10^3 kg/m^3 and 1.0×10^{-2} Pa·s, respectively. The CPU time for this problem is very long when a conventional relaxation time ($\tau \leq 1$) is used. Therefore, a high relaxation parameter is used to reduce the CPU time. The parameters for collision terms are $\tau_+ = 8$, $A = 0.5$ and $\Lambda = 0.03$ in TRT. The time step size is 2.5×10^{-5} s. The number of Lagrangian points at the surface of each particle is determined so as to make the spacing between two adjacent points on the surface comparable to the grid spacing. Thus, the numbers of Lagrangian points of the largest and smallest particles are 314 and 78, respectively.

First the simulation is carried out using SRT. However, it is failed due to large errors in the velocity field and numerical instability appears. Then, TRT is used. No instability appears and the vorticity contour of the motion is shown in Figs. 5.12 (b)-(f). At $t = 0.5$ s, the large particle rapidly falls due to its initial velocity and high density. A pair of vortices is formed behind it. In contrast, the motion of the small particles is almost

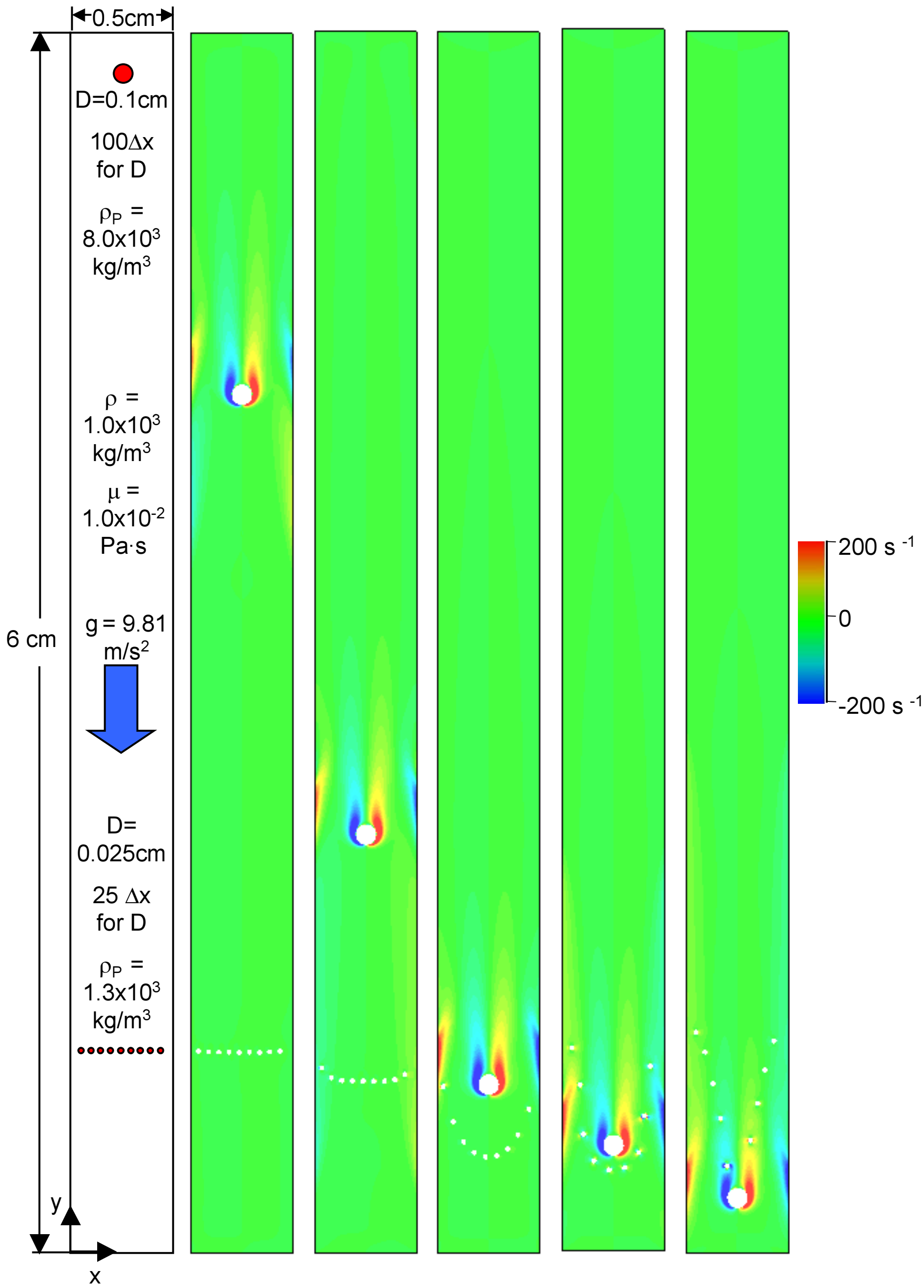

(a) (b) t =0.5 s (c) 1 s (d) 1.3 s (e) 1.4 s (f) 1.5 s

Fig. 5.12 Computational domain (a) and vorticity contour of sedimentation of multiple particles at low and moderate Reynolds numbers negligible in the early stage. The particle Reynolds number in the system varies from 0.027 for the small particles to 8 for the large particle. As the large particle approaches the small particles, the motion of the small particles becomes faster. At t = 1.4 s, the large particle collides the small particles. The paths of the small particles are strongly affected by the collision at t = 1.5 s.

5.7 Conclusions

A two-relaxation time (TRT) collision model was implemented into the immersed boundary-finite difference lattice Boltzmann method (IB-FDLBM) to reduce numerical errors appearing at low Reynolds numbers, i.e. at high relaxation times. An implicit direct forcing method was also implemented into IB-FDLBM to accurately deal with the no-slip boundary condition at the immersed boundaries. Simulations of circular Couette flows were carried out to validate the proposed method. In addition, flows past a circular cylinder and a sphere were simulated to examine the applicability of the method to both low and high Reynolds number flows. Finally, the sedimentation of multiple particles with various particle Reynolds numbers was carried out. As a result, the following conclusions were obtained:

(1) TRT reduces numerical errors causing non-physical distortion in the fluid velocity at low Reynolds numbers, and accurate predictions are obtained when the parameter Λ defined by Eq. (5.4) is low.

(2) For stable simulation the parameter Λ should be decreased as the Reynolds number increases.

(3) Implementation of TRT and the implicit direct forcing method into IB-FDLBM can solve two problems in simulation of low Reynolds number flows, i.e. non-physical velocity distortion and non-physical penetration of flow into a solid body.

(4) IB-FDLBM with TRT gives good predictions of the drag coefficients of a circular cylinder and a sphere in uniform flows for a wide range of the Reynolds number, *Re*, i.e., $0.1 \leq Re \leq 1\text{x}10^4$.

(5) Particulate flows with various particles are predicted with the proposed method.

References

Bhatnagar, P., L., Gross, E., P., Krook, M., A model for collision processes in gases. I. Small amplitude processes in charged and neutral one-component systems, Physical Review, 1954, 94, pp. 511-525.

Dupuis, A., Chatelain, P., Koumoutsakos, P., An immersed boundary–lattice-Boltzmann method for the simulation of the flow past an impulsively started cylinder, Journal of Computational Physics, 2008, 227, pp. 4486-4498.

Ginzburg, I., Verhaeghe, F., d'Humieres, D., "Two-relaxation-time lattice Boltzmann scheme: about parametrization, velocity, pressure and mixed boundary conditions", Communication in Computational Physics, 2008, 3(2), pp. 427-478.

Lamb, H., On the uniform motion of a sphere through a viscous fluid, Phil. Mag., 6(xxi), 112 (1911).

Le, G., Zhang, J., Boundary slip from the immersed boundary lattice Boltzmann models, Physical Review E, 2009, 79, 026701.

Tsutahara, M., Kurita, M., Iwagami, T., A study of new finite difference lattice

Boltzmann model, Transaction of Japanese Society of Mechanical Engineers, Series B, 68(665) (2002) pp. 15-21. (in Japanese)

Wieselsberger, C., Further information on the laws of fluid resistance, National Advisory Committee for Aeronautics, 121 (1922).

Wu, J., Shu, C., Implicit velocity correction-based immersed boundary-lattice Boltzmann method and its applications, Journal of Computational Physics, 228 (2009) pp. 1963-1979.

Yang, X., Zhang, X., Li, Z., He, G.W., A smoothing technique for discrete delta functions with application to immersed boundary method in moving boundary simulations, Journal of Computational Physics, 2009, 228, pp. 7821-7836.

6

Conclusions

6.1 Conclusions

In this dissertation, a new numerical method was proposed to predict liquid-solid two-phase flows for a wide range of the particulate Reynolds number. The method is a combination of an immersed boundary method (IBM) and a finite difference lattice Boltzmann method (FDLBM). The use of the finite difference method allows us to set the lattice spacing and the time step size independently. Furthermore, an additional collision term, which works as a negative viscosity at the macroscopic level, is added to the discrete Boltzmann equation for numerical stability. IBM is based on a direct-forcing method, in which an external forcing term to impose the no-slip boundary condition at immersed boundaries is added to the discrete Boltzmann equation. The performance of the proposed method was demonstrated through several two- and three-dimensional calculations.

First, calculations of cavity flows at different Reynolds numbers were carried out using FDLBM with the additional term in Chapter 2 to prove that FDLBM can deal with high Reynolds number flows. Then, IBM was combined with FDLBM to deal with moving particles. The Chapman-Enskog expansion was applied to the discrete Boltzmann equation with the additional collision term and the external forcing term of IBM to prove that the present Boltzmann equation recovers the macroscopic equations for incompressible Newtonian fluids. Two- and three-dimensional simulations of single particles falling in liquids and interaction between two particles were carried out to validate the proposed method. As a result, the following conclusions were obtained:

(1) The velocity distribution of cavity flows at moderate and high Reynolds numbers is stably and accurately predicted using FDLBM.

(2) The continuity and Navier-Stokes equations are recovered by applying the Chapman-Enskog expansion to the discrete Boltzmann equation with the external forcing term.

(3) The motions of particles falling through liquids at intermediate particle Reynolds numbers predicted using IB-FDLBM quantitatively agree with those obtained using IB-LBMs.

(4) The proposed method well predicts the interaction between two intermediate Reynolds number particles, e.g., the drafting-kissing-tumbling (DKT) motion.

In Chapter 3, the applicability of IB-FDLBM to flows at high Reynolds numbers was examined. It is known that when the relaxation time is decreased while keeping the relevant dimensionless numbers constant, the spatial resolution of IB-LBM needs to be increased to stably calculate flows at high Reynolds numbers. On the other hand, in the proposed IB-FDLBM, the additional collision term allows us to alter the fluid viscosity without changing the relaxation time and the spatial resolution, so that the proposed method is expected to be able to deal with flows at high particle Reynolds numbers without increasing the spatial resolution. Simulations of flows past two-dimensional stationary circular and square cylinders and flows past a sphere were carried out for a wide range of particle Reynolds numbers for validation. Free-falling cylinders at intermediate and high Reynolds numbers were also simulated. As a result, the followings were confirmed:

(5) The drag coefficient, the Strouhal number and the flow structure of flows past a stationary cylinder are well predicted for a wide range of *Re*, i.e. $1 \le Re \le 1\times10^5$.

(6) IB-FDLBM can stably simulate flows at high particle Reynolds numbers without increasing the spatial resolution.

(7) IB-FDLBM gives reasonable predictions of the drag coefficients of a sphere in uniform flows for a wide range of Reynolds number, i.e. $1 \le Re \le 1\times10^4$ provided that the ratio of the cylinder diameter to the lattice spacing is high enough.

(8) IB-FDLBM accurately predicts the reduction in the Strouhal number of vortex shedding behind a moving cylinder due to the falling-motion of the cylinder at intermediate Reynolds numbers.

(9) IB-FDLBM also reasonably predicts the motion of the moving cylinder at high

Reynolds numbers.

IB-LBM has problems not only at high Reynolds numbers but also at low Reynolds numbers (high relaxation times), that is, errors in velocity near the immersed boundary remarkably increase with decreasing the Reynolds number, i.e. increasing the relaxation time. It is known that the numerical stability and accuracy of LBM mainly depend on the number of discrete velocities and the numerical treatment of the collision term. Therefore a remedy for the above-mentioned problem in IB-LBM at low Reynolds number might be to improve the discrete velocity model and/or the collision model. The increase in the number of discrete velocities however makes the computational cost high. It was therefore decided to use D2Q9 and D3Q19 models, which are the most common models for the discrete velocity. For the collision model, the single relaxation time collision model (SRT) has been often used due to its simplicity and efficiency. It is however well known that numerical errors increase with the relaxation time and Le and Zhang (2009) pointed out that non-physical velocity distortion appears at high relaxation times. Therefore the improvement of the collision model was attempted in this study. The multiple-relaxation time (MRT) collision model has been often used instead of SRT to improve the numerical stability and accuracy of LBM. However MRT is much more complicated than SRT: for instance, the number of relaxation times for D3Q19 model is 19 and several relaxation times are arbitrary (no definite principle are present for these arbitrary relaxation times). The simplest multi-relaxation-time model, i.e. the two-relaxation time (TRT) collision model, was therefore utilized. The formulation of TRT is as simple as that of SRT. TRT uses one relaxation time for determining the viscosity and the other for improving the numerical stability and accuracy. In Chapter 4, TRT was implemented into IB-LBM. It is expected that the implementation of TRT helps to remove or reduce the errors appearing at low Reynolds numbers (at high relaxation times). To validate the method, numerical simulations of circular Couette flows, sedimentation of single particles and DTK motion were carried out. The effect of TRT on numerical errors in velocity of symmetric shear flows was analytically and numerically studied. The conclusions obtained are as follows:

(10) IB-LBM with TRT does not cause a non-physical anti-symmetric velocity distribution in a circular Couette flow even at low Reynolds numbers, i.e. at high relaxation times.

(11) Two- and three-dimensional particulate flows with moving boundaries are reasonably predicted using IB-LBM with TRT.

(12) The analytical solutions obtained for the velocity gradient, the boundary velocity and the boundary slip agree well with the numerical predictions in the same conditions.

(13) The two-relaxation time collision model can remove the boundary slip velocity or accurately impose the boundary velocity at low Reynolds numbers. However it cannot solve both problems at the same time.

In Chapter 5, the two-relaxation time collision model was also implemented into

IB-FDLBM to extend the range of applicability of the proposed method to simulations of low Reynolds number flows. First, the Chapman-Enskog expansion was applied to the discrete Boltzmann equation with the two-relaxation time collision term to show the recovery of the macroscopic conservation equations for incompressible Newtonian flows. Simulations of circular Couette flows were carried out to validate the present method. Flows past a circular cylinder and a sphere were calculated to examine the applicability of the method to both low and high particle Reynolds numbers. To accurately deal with the no-slip boundary condition at the immersed boundaries and avoid additional problems appearing in flows at low Reynolds numbers, an implicit direct forcing method was implemented into IB-FDLBM. Finally, sedimentation of multiple particles with various Reynolds numbers was carried out. As a result, the following conclusions were obtained:

(14) The continuity and the Navier-Stokes equations are reasonably recovered, and the kinematic viscosity is determined by one relaxation time.

(15) TRT implemented into IB-FDLBM reduces numerical errors causing non-physical distortion in the fluid velocity at low Reynolds numbers.

(16) Implementation of TRT and the implicit direct forcing method into IB-FDLBM can solve two problems in simulation of low Reynolds number flows, i.e. non-physical velocity distortion and non-physical penetration of flow into a solid body.

(17) IB-FDLBM with TRT gives good predictions of the drag coefficients of a circular cylinder and a sphere in uniform flows for a wide range of the particle Reynolds number.

(18) Particulate flows with various particles are predictable with the proposed method.

In summary, IB-FDLBM is proved to be an effective method for solving flows including various particles ranging from low to high particle Reynolds numbers. A guideline for using the present numerical method is given in Appendix C.

Appendix

A. Stability analysis of the finite difference lattice Boltzmann method

The Von Neumann stability analysis is applied to the governing equation of the finite difference lattice Boltzmann method, Eq. (2.3):

$$\frac{\partial f_k}{\partial t} + c_{k\alpha}\frac{\partial f_k}{\partial x_\alpha} - \frac{Ac_{k\alpha}}{\tau}\frac{\partial}{\partial x_\alpha}\left[f_k - f_k^{eq}\right] = -\frac{1}{\tau}\left[f_k - f_k^{eq}\right] \tag{A.1}$$

where k represents the direction of the discrete velocity. For the purpose of simplifying the stability analysis, a general distribution function, f, is considered and the advection and the negative terms are omitted from Eq. (A.1). Thus, the analysis is done for an idealization of the collision term given by

$$\frac{\partial f}{\partial t} = -\frac{1}{\tau} f \tag{A.2}$$

The discretization of Eq. (A.2) is given by

$$f_j^{n+1} = \left(1 - \frac{\Delta t}{\tau}\right) f_j^n \tag{A.3}$$

where n is the discrete time, Δt is the time increment and the subscript j represents the spatial position. Equation (A.3) can also be expressed in terms of the round-off error ε_j^n:

$$\varepsilon_j^{n+1} = \left(1 - \frac{\Delta t}{\tau}\right) \varepsilon_j^n \tag{A.4}$$

Equations (A.3) and (A.4) show that both equations have the same growth or decay behavior with respect to time. For linear differential equations, the error may be expressed as the growth of a typical term

$$\varepsilon(x,t) = e^{at} e^{ik_m x} \tag{A.5}$$

where a is a constant and k_m is the wavenumber. Expressing each term in Eq. (A.4) in terms of the typical error term Eq. (A.5) yields

$$\varepsilon_j^{n+1} = e^{a(t+\Delta t)} e^{ik_m x} \tag{A.6}$$

$$\varepsilon_j^{n} = e^{at} e^{ik_m x} \tag{A.7}$$

Substitution of Eqs. (A.6) and (A.7) into Eq. (A.4) gives

$$e^{a(t+\Delta t)} e^{ik_m x} = \left(1 - \frac{\Delta t}{\tau}\right) e^{at} e^{ik_m x} \tag{A.8}$$

$$e^{\Delta t} = \left(1 - \frac{\Delta t}{\tau}\right) \tag{A.9}$$

Now, the amplification factor, H, is defined as

$$H = \frac{\varepsilon_j^{n+1}}{\varepsilon_j^{n}} \tag{A.10}$$

The necessary and sufficient condition for the error to be bounded is that, $|H| \leq 1$. Thus, the condition for stability is given by

$$\left|1-\frac{\Delta t}{\tau}\right| \le 1 \tag{A.11}$$

Finally, the solution of Eq. (A.11) gives the condition for stable calculation using the finite difference lattice Boltzmann method:

$$\frac{\Delta t}{\tau} \le 2 \tag{A.12}$$

B. Flow past a circular cylinder with body-fitted grid finite difference lattice Boltzmann method

Flows past a stationary circular cylinder are also calculated using the body-fitted grid finite difference lattice Boltzmann method. The computational domain and O-grid in the vicinity of the cylinder are shown in Figs. B.1 (a) and (b). The spacing lattice in the radial direction grid gradually increases outwards. The diameter of the cylinder, D, is 1, and the computational domain size is 200D represented by 151 and 126, in the radial and angular direction, respectively. The cylinder is located at the center of the computational domain. The free stream velocity, U_0, is 0.005 and 0.05 at $Re < 1$ and $Re \geq 1$, respectively. All the other boundaries are continuous outflow. The Reynolds number varies from 0.1 to 1×10^5. The parameter Λ is 7.5×10^{-4} for flows at $Re < 1$.

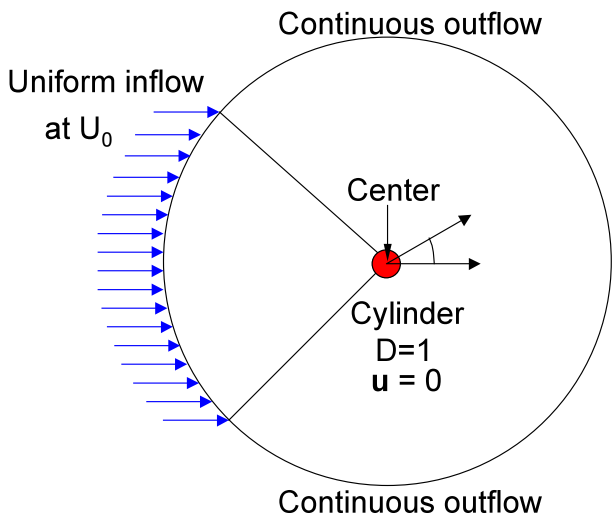

(a)

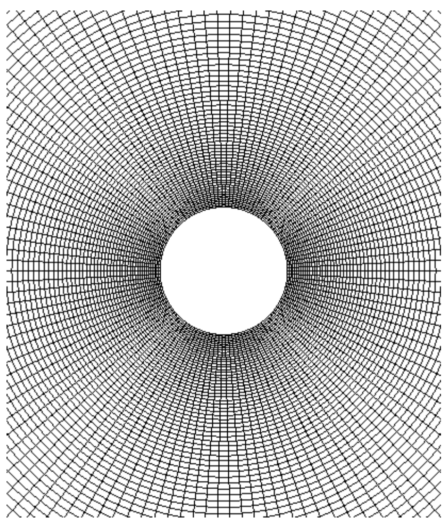

(b)

Fig. B.1 Computational domain for flows past a circular cylinder using body-fitted grid FDLBM

Calculations using SRT and TRT are carried out and it is confirmed that SRT and TRT give the same predictions for flows at Re $\geq$ 1. At lower Reynolds numbers non-physical distortion of the streamlines appear when using SRT (Fig. B.2 (a)), whereas TRT prevents the distortion of streamlines (Fig. B.2 (b)). The flows past a circular cylinder in different regimes are shown in Figs B.2 - B.5. Figure D.2 (b) shows creeping flow at *Re* = 0.1. Two steady symmetric vortices are formed behind the cylinder at *Re* = 20 and 40. The streamlines of unsteady flows at *Re* = 100 and 100000 at two instants are shown in Figs. B.4 and B.5. These patterns are in good agreement with experimental observations

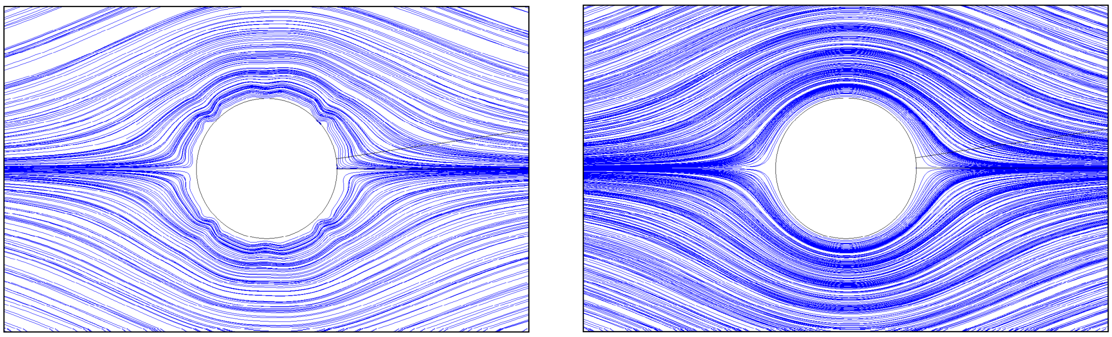

(a) SRT (b) TRT

Fig. B.2 Streamlines of flows at *Re* = 0.1 obtained using body-fitted grid FDLBM

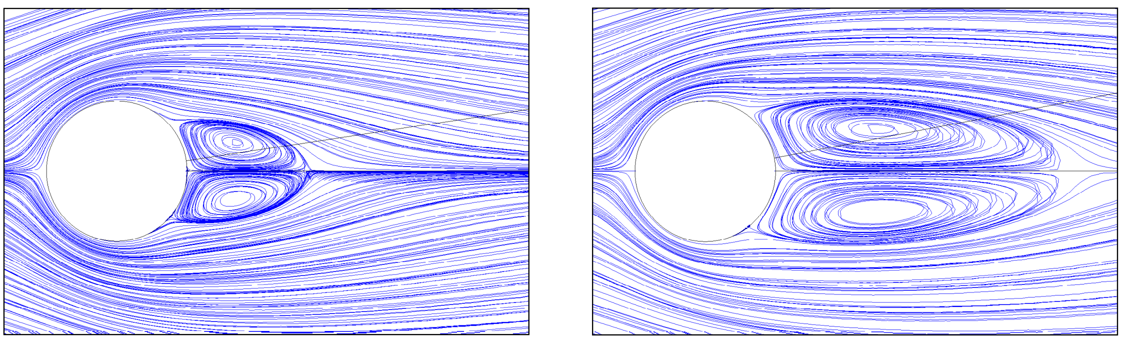

(a) *Re* = 20 (b) *Re* = 40

Fig. B.3 Streamlines of flows steady flows obtained using body-fitted grid FDLBM

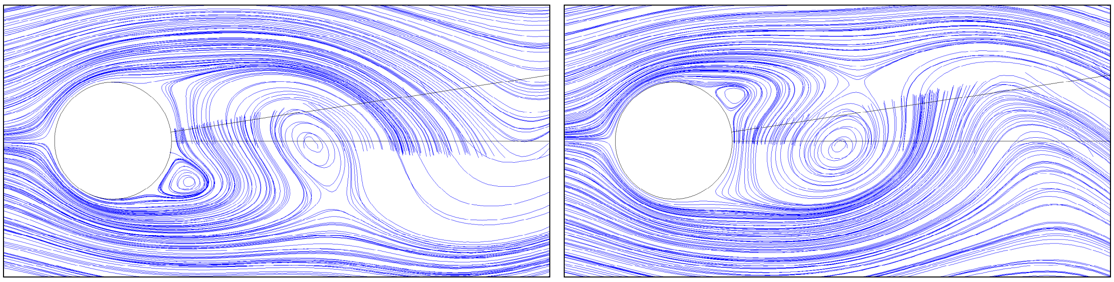

(a) Dimensional Time $U_0 t/D$ = 220.0 (b) $U_0 t/D$ = 222.4

Fig. B.4 Streamlines of flows at Re = 100 obtained using body-fitted grid FDLBM

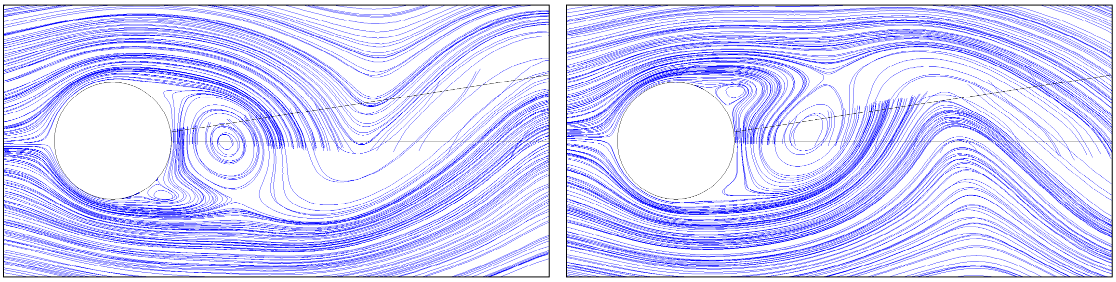

(a)$U_0 t/D$ = 220.0 (b) $U_0 t/D$ = 222.4

Fig. B.5 Streamlines of flows at Re = 100000 obtained using body-fitted grid FDLBM

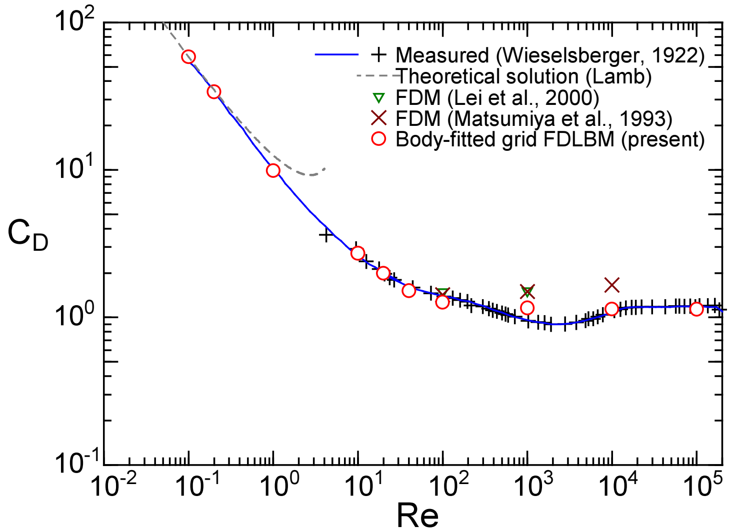

Fig. B.6 Drag coefficient of a stationary cylinder predicted by using body-fitted grid FDLBM

The drag coefficients and Strouhal numbers predicted using body-fitted grid FDLBM are plotted against the Reynolds number in Figs. B.6 and B.7. The predictions reasonably agree with measured data [Wieselsberger, 1920; Roshko, 1954; Schewe, 1983] and other numerical predictions [Lei et al, 2000; Matsumiya, 1993] are obtained for a wide range of Reynolds numbers.

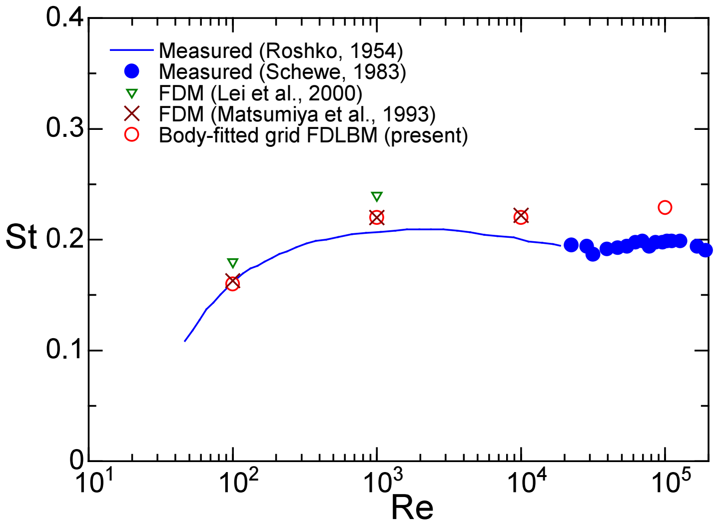

Fig. B.7 Strouhal number of a stationary cylinder predicted by using body-fitted grid FDLBM

C. Guideline for using IB-FDLBM for predicting particulate flows

In this study, several numerical methods for predicting particulate flows have been proposed. First, IB-FDLBM with the explicit direct-forcing method and SRT was proposed. Then, the two-relaxation time collision model was implemented into IB-FDLBM. Finally, the calculation of the direct-forcing term was modified from the explicit to implicit scheme. In addition, OpenMP for parallel computation was adopted to enhance the efficiency of calculations. In this section, a guideline for using IB-FDLBM is stated.

The appropriate use of the proposed method, of course, depends on the problem, and the available computational resources. An important matter of the numerical methods is the calculation time. Therefore, it is preferable to implement OpenMP or MPI for all the three available schemes, i.e. explicit direct-forcing SRT, explicit direct-forcing TRT and implicit direct-forcing TRT.

The explicit direct-forcing method with SRT is applicable to problems with stationary or moving boundaries at intermediate and high Reynolds numbers. To be more specific, the relaxation time used in the calculation should be of the order of unity. In this way, errors in the velocity field are kept small. Additionally, the penetration of streamlines into immersed boundaries is negligibly small.

The explicit direct-forcing method with TRT is appropriate to solve problems with complex geometry at low particle Reynolds numbers, i.e. $Re < 1$. The relaxation time at low Reynolds numbers for a given characteristic velocity and a characteristic length is usually high. Accurate predictions are obtained when the parameter Λ, which is a function of the two relaxation times, is low, usually less than unity.

The implicit direct-forcing method with TRT is effective to solve problems including obstacles at low Reynolds number particles ($Re < 1$). When a relaxation time is fixed, the controllable parameter to obtain reasonable predictions is Λ. In the same way as the afore-mentioned method, Λ should be less than unity. This method is applicable not only to low Reynolds number particles but also high Reynolds number particles. Hence IB-FDLBM with TRT should be chosen when low and high Reynolds number particles are simultaneously present.

Acknowledgments

First of all, I would like to express my appreciation to the Ministry of Education, Science, Sports and Culture (Monbukagakusho) of the Government of Japan for their financial support during my stay in Japan.

I would also like to express my deep gratitude to my supervisors Prof. Akio Tomiyama, Prof. Takeshi Seta, and Prof. Kosuke Hayashi whose continuous support, patient guidance and valuable suggestions have enabled me to complete my studies.

I am particularly grateful for the constructive criticism and significant contributions given by Prof. Shigeo Hosokawa and Dr. Katsuji Akamatsu.

I would like to offer my special thanks to all the members of the laboratory of Energy and Environmental Engineering, Kobe University -in particular Shimpei Ojima, Shogo Hosoda, Mohd Hatta, Kazuya Ishii, Kyosuke Kitahata and Yuki Fujii- for all their cooperation and kindness both inside and outside the laboratory.

Finally, I would like to take this opportunity to thank my family and friends, both who are in Ecuador and Japan, who have always been there with their words of support and encouragement.

みなさん、ありがとうございました。

Muchas gracias a todos.

Roberto Rojas

Doctor Thesis, Kobe University
"Immersed Boundary-Finite Difference Lattice Boltzmann Method for Predicting Particulate Flows", 138 pages

Submitted on July, 12, 2013
The date of publication is printed in cover of repository version published in Kobe University Repository Kernel.